SOLID STATE ELECTRONICS LABORATORY

Stanford Solid State Electronics Laboratory

HIGH PRECISION X-RAY LITHOGRAPHIC MASKS

Final Report on Contract # N0014-90-K-2000
NRL Project # 68-1717-90

Under Sponsorship from U. S. Naval Research Laboratory

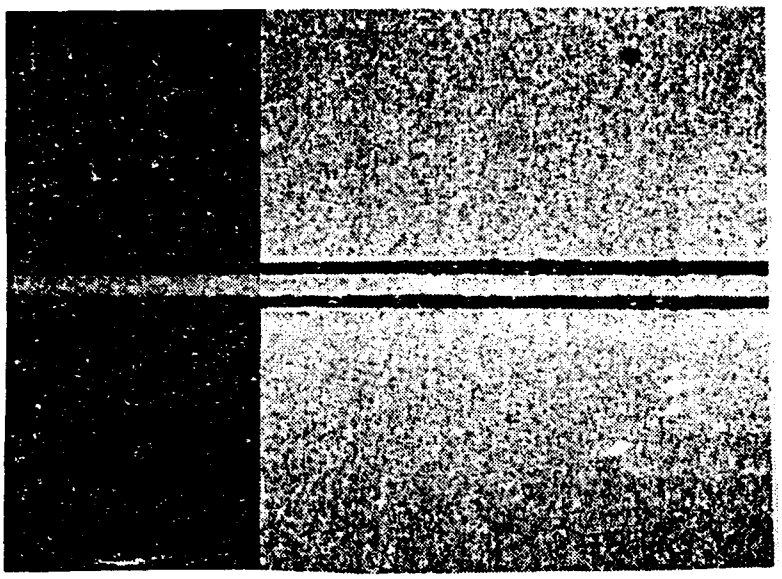

I 86nm

Principal Investigator: R. F. W. Pease, Professor of Electrical Engineering
Co-Principal Investigator: R. Browning, Senior Research Associate

93 11

STANFORD ELECTRONICS LABORATORIES • DEPARTMENT OF ELECTRICAL ENGINEERING
STANFORD UNIVERSITY • STANFORD, CA 94305-4055

DISCLAIMER NOTICE

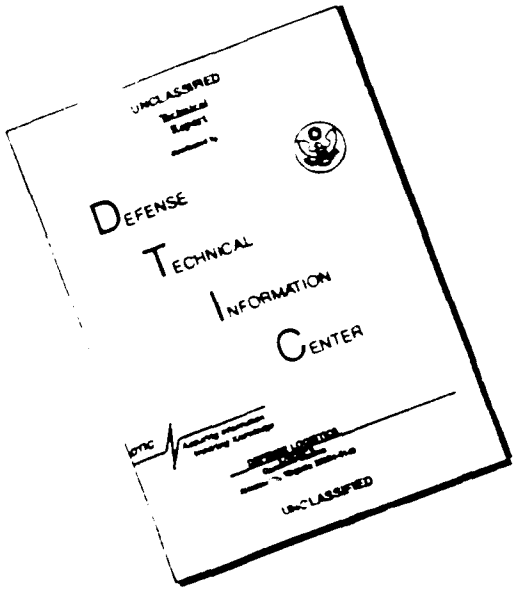

THIS DOCUMENT IS BEST QUALITY AVAILABLE. THE COPY FURNISHED TO DTIC CONTAINED A SIGNIFICANT NUMBER OF PAGES WHICH DO NOT REPRODUCE LEGIBLY.

CONTENTS

1. EXECUTIVE ABSTRACT

This contract period, March 1990 to July 1992, was first concerned with winding up the projects on the embedded X-ray Mask structure and on the 'quantum lithography' idea. Both were published as journal articles and in the PhD. Dissertation of N. Maluf (Dept. of ELectrical Engineering, Stanford University, 1990). As a result of that earlier work and of developments elsewhere it became clear that the among the most critical issues in achieving high precision X-ray masks were those associated with achieving high precision in both feature size and feature placement in electron beam lithography. Most of the effort in this reporting period was aimed at achieving precision in feature size; notably an attack on the problem of proximity effects. There were two approaches:

1. A short term approach aimed at correcting proximity effects in existing electron beam pattern generators (notably the ETEC MEBES 3 and 4) for feature sizes down to 500 nm.

2. A long term approach aimed at avoiding proximity effects by employing low energy electron exposure for feature sizes below 500 nm.

The first approach was successfully executed during the first year of the contract period under a sub-contract to Perkin Elmer EBT (now ETEC Systems Inc). Successful correction for proximity efffects was demonstrated for features down to 400 nm for both sparse and dense patterns using a modification of the GHOST approach. This technique is now available for use on MEBES equipment. The report on this sub-contract is attached as an appendix.

The second approach, the use of low voltage (<=2KV) electron beam exposure, has also been successful. We have computer modeled and experimentally demonstrated good feature size control for features smaller than 100 nm in both sparse and dense regions. For a 10% change in dose (far larger than is normally allowed), the linewidth variation of was less than 10nm. These experiments were carried out with a modified Hitachi S-800 scanning electron microscope operating at 2 KV. The electron optics of this SEM, while excelient for an SEM and just usable for experiments in lithography, is far from optimum as a reliable source of well focused, low energy electrons. Accordingly we initiated an investigation into low voltage electron optics; this work is continuing under a grant from DARPA/ONR.

During the research period we also developed the idea of using orientation-dependent etched single crystal silicon as a useful calibration plate for electron beam pattern generators and so begin an attack on the feature placement problem in electron beam mask making. The crystallographic axes make for a naturally square and straight features that act to complement the laser interferometers, which give accurate distance calibration, to ensure improved pattern fidelity. This project is being continued under the current grant from DARPA/ONR.

2. INTRODUCTION

Although there have been many ingenious ideas for exposing wafers with sub-optical resolution nearly all suffer from the Achilles heel of inadequate mask technology. Proximity X-ray lithography is no exception. When X-ray lithography (XRL) was first invented minimum feature sizes in integrated circuits were about 7 μm and it was envisaged that X-ray lithography would be introduced for feature sizes above 1μm. For such features satisfactory 1X electron beam pattern generation technology existed for making the masks. However by 1989 it appeared that XRL would be used primarily for manufacturing circuits with feature sizes below 500 nm. As a result the there needed to be significant improvements in the electron beam technology used for patterning the masks. The research program supported by this contract extended from December 1989 to April 1992 and was concentrated on the issue of minimizing feature-size errors introduced by electron scattering in the workpiece ('proximity effects'). There were two main aspects:

1. Developing a short term correction procedure that could be implemented on existing pattern generators and was acceptable for feature sizes down to 500nm and perhaps below.

2. Investigating longer term strategies that would suffice for feature sizes down to 100nm.

A third aspect was related to the second and was an investigation of advanced electron optical concepts for new-generation electron beam mask makers. This third aspect is the main thrust of the new contract initiated September 1992.

3. SHORT TERM CORRECTION FOR ELECTRON BEAM PROXIMITY EFFECTS

Although many schemes for correcting proximity effects had been described since the original work of Parikh in 1977 (Int. Symp. on Electron, Ion and Photon Beam Tehcnology, Proceedings published in J. Vac. Sci. Tech.). None had been implemented on the most widespread mask making tools, the MEBES series of electron beam pattern generators from ETEC. Accordingly ETEC undertook, as a 1-year sub-contract, to review the options and choose and implement the most suitable. After the initial review a modified version of the GHOST (G. Owen and P. A. Rissmann, J. Appl. Phys. June 1983) strategy was chosen. Computer simulation indicated that by using GHOST for correcting for the effects of electrons backscattered from the substrate and feature-size biassing to correct for forward scattering in the resist it should be possible to achieve adequate correction for feature sizes down to below 400 nm without changing the basic mask making materials and processes . This prediction was borne out by experiment; as more experience was gained, it was even found unnecessary to bias the feature edges (fig. 3.1). This procedure has now been implemented as an option for commercial mask vendors. The ETEC report describing this work is attached as an appendix.

ETEC

FIG 3-1

0.3 μm Minimum Feature Size Resist on X-Ray Substrate

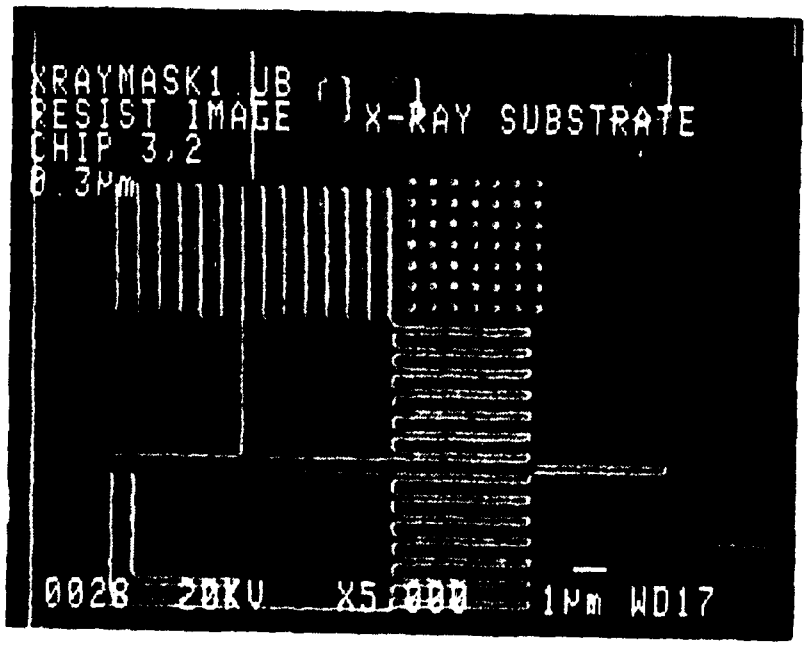

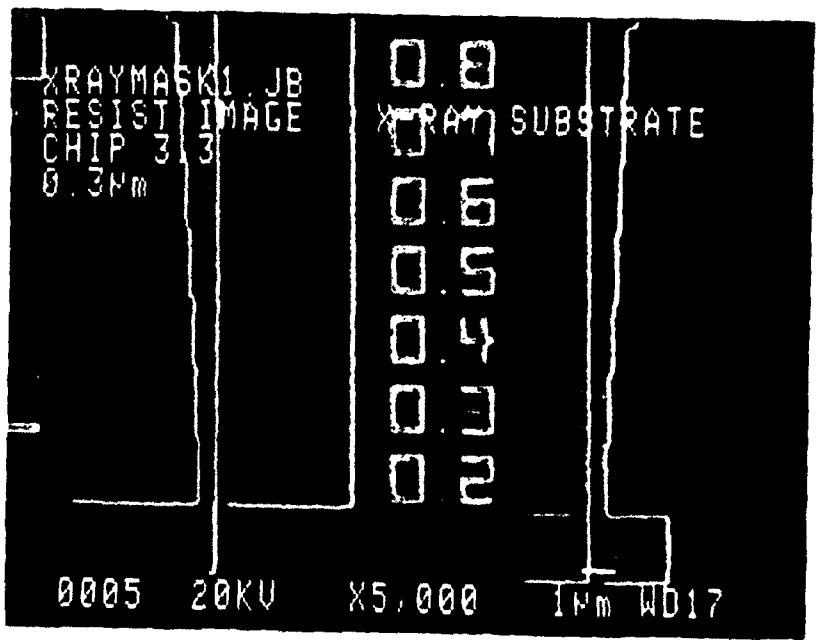

4. ELIMINATION OF PROXIMITY EFFECTS-SIMULATION

The major goal for this work was to establish the ability to predict the proximity effects for electron beam lithography over a wide range of energies and materials. The processes in electron scattering are non-linear and at medium and high energies (5-100keV) are dependent on the three dimensional structure of the target. For this reason the simulation of the deposited energy distribution by solution of a diffusion equation is only possible with considerable simplifying assumptions and Monte-Carlo simulations of electron trajectories is the major technique for determining the properties of the electron beam target interaction.

For simulation of electron trajectories we initially used software packages obtained from U.C.Berkley (SAMPLE) and the University of Tennesse. We found that although these packages were excellent for the conventional range of electron energies expected in electron beam lithography (10-30kkeV) they did not give us the energy range or the flexibilty in materials we required. In the absence of software packages available to fit our needs we have developed a complete software package to simulate exposure and development.

The simulator software we have developed is flexible and accurately covers a very wide range of target structures and energies. Multiple target layers are possible and thus electron scattering from structures such as multi-layer X-ray masks can be simulated. The radial distribution of deposited electron energy is treated in a novel way to give high accuracy but minimum computation time over a wide range of energies. In a conventional Monte-Carlo program the distribution of electrons scattered into a resist is treated by considering the energy deposited into a set of parralell stripes (bins) linearly increasing away from the center of the initial irradiation. Ten thousand stripes are needed to cover the range of the electrons (10 microns) with 1nm acuracy. This large number of stripes increases the computation time both in the Monte-Carlo simulation, because relatively few electrons reach the outer stripes, and also during the fitting of Gaussians to the final energy distributions. As an alternative to linear stripes we have used a radial bin with an exponentially increasing bin size. An initial circular bin of 1nm diameter is surrounded by annular bins increasing by 10% per bin. Thus the first annular bin is between 1nm and 1.1nm diameter, and the bins increase to 10.4 microns in only 97 steps. This scheme thus gives high spatial accuracy where it is neeeded at the impact point and to simulate low energy scattering, yet gives a wide range for high energy electrons with large bins where the electron energy deposition per unit area is low. We have found this scheme to be very successfull.

The resist layer which is normally chosen as the top layer is divided into five equal slices and up to six Gaussians can be fitted to the energy distributions in each slice. We normally find that at least three Gausssians are needed to fit the resist energy distributions to better than 10% accuracy and that the forward scattering is not well represented by a single Gaussian. This latter fact is obvious from the form of the Mott and Rutherford scattering crossections.

We have made a significant advance in the use of Monte-Carlo programs for low electron energy scattering simulations by introducing a new formula for the scattering cross sections. The Monte-Carlo simulation of electron beam scattering from high atomic number targets requires an accurate but simple model of the electron/atom scattering crossections. We have modified the form of the screened Rutherford elastic scattering cross-section to approximate the Mott scattering cross-section for low energy electrons interacting with high atomic number targets both for the total and the differential elastic cross-section. This work is fully described in appendix 2.

Low Energy Electron Ineleastic Mean Free Paths In Resists.

The inelastic mean free path (IMFP) of low energy (1.4keV) electrons traveling in the Langmuir-Blodgett (L-B) PMMA films was measured using x-ray photoelectron spectroscopy (XPS). In an XPS experiment, the probability of a primary photoelectron escaping from a depth z below the surface of a clean solid A is proportional to $\exp(-z/\lambda_A)$ where λ_A is the inelastic mean free path for the electrons in the solid[1,2]. Therefore, the intensity ratio of the substrate XPS signal (I_d) with an overlayer A of thickness d to that (I_0) in the absence of the overlayer is:

$$I_d = I_0 \exp(-d/\lambda_A \sin\theta)$$

With the knowledge of the precise thickness of overlayer and the take-off-angle the IMFP can be obtained using the relationship between measured I_d and I_0. An empirical equation based on a compilation of results is often used for the IMFP of electron energies in the range between 10 to 2000eV. For organic overlayers the IMFP is:

$$\lambda = \frac{538}{E^2} + 0.41(aE)^2 \quad \text{monolayer}$$

where a is the monolayer thickness in nm and E is the electron energy in eV[3].

From this equation it can be seen that XPS with electron energies in the range of 0.1 to 2keV is a surface sensitive technique with the majority of the XPS signal coming from the first few surface monolayers. For IMFP measurements using XPS, it is clearly important to know the precise overlayer thickness. For organic molecules, spin casting is the common technique to have uniform films on substrates. However, as the thickness goes thinner than 10nm, the pinhole density gets much higher. The Langmuir-Blodgett technique is a method of preparing ultra-thin L-B PMMA films of a precise thickness with very few pinholes[4].

Atactic-PMMA obtained from Pressure Chemical, with weight average molecular weight (Mw) of 188,100 amu and Mw/Mn < 1.08, where Mn is the average molecular weight, was used to prepare the monolayers on the thermally evaporated Au/Si substrate by the standard Langmuir-Blodgett technique. A Joyce-Loebl Langmuir Trough IV equipped with a microbalance for measurement of the surface pressure by the Wilhelmy plate method was used to prepare the Langmuir-Blodgett films. Filtered deionized water with a pH of 7 was used for the subphase. PMMA was spread on the water surface from a dilute chlorobenzene solution (10 mg PMMA in 20 ml benzene). Transfer pressure of 15 dyn/cm was used to deposit L-B films during downstroke and upstroke at the speed of 2 mm/min. The first monolayer is transferred to Au/Si substrate by dipping the substrate to the subphase due to the hydrophobic nature of the Au surface. The subsequent monolayers were deposited during upstrokes and downstrokes. The thicknesses of the L-B films can be accurately measured by ellipsometry technique. For each L-B PMMA monolayer, the thickness is 0.85nm[4] so that in using overlayer structures from two to eight monolayers overlayer thicknesses are from 1.7 to 6.8 nm.

A Surface Science ESCA system was used for the XPS measurements. Monochromatic X-rays from Al target was used to minimise damage to the polymer structures. C1s, O1s, and Au4f were collected from the L-B PMMA films of 2, 4, 6, and 8 monolayers at two take-off-angles; 38 and 60 degrees from the surface plane. For these experiments, the PMMA L-B films were prepared separately.

The photoelectron (1.4keV) intensities of Au4f7/2 peaks at different take-off-angles are plotted as functions of number of the L-B PMMA monolayer, as shown in figure The IMFP can be obtained by using the relationship between I_d and I_0, as described in equation (2). The IMFP's derived from figure 1 are listed in table 1, and the average IMFP for 1.4keV electrons traveling in the L-B PMMA films is found to be 8.3nm.

1. W. J. Carter,et al, J. Electr. Spectr. 5, 827(1974).
2. T. A. Carlson and G. E. McDuire, ibid, 1, 161(1972).
3. M. P. Seah and W. A. D. Dench, Surf. Interface Anal. 1, 2(1979).
4. S. W. J. Kuan, C. W. Frank, C. C. Fu, D. R. Allee, P. Maccagno, and R. F. W. Pease, J. Vac. Sci. Technol. B6, 2274(1988).

take-off-angle	measured IMFP
38°	8.69nm
60°	7.90nm

Table 1 Measured IMFP's at different take-off-angles.

FIG. 4.1

The photoelectron intensity of Au4f7/2 peaks at different take off angles as a function of number PMMA L-B monolayers. (a) at 38^0 (b) at 60^0 take off angle.

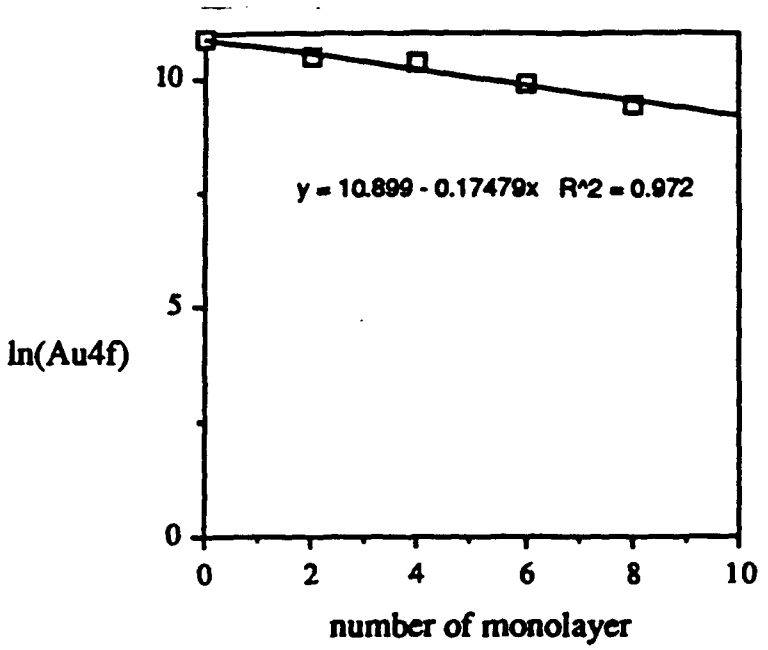

(a) IMFP measurement at take-off-angle 38°.

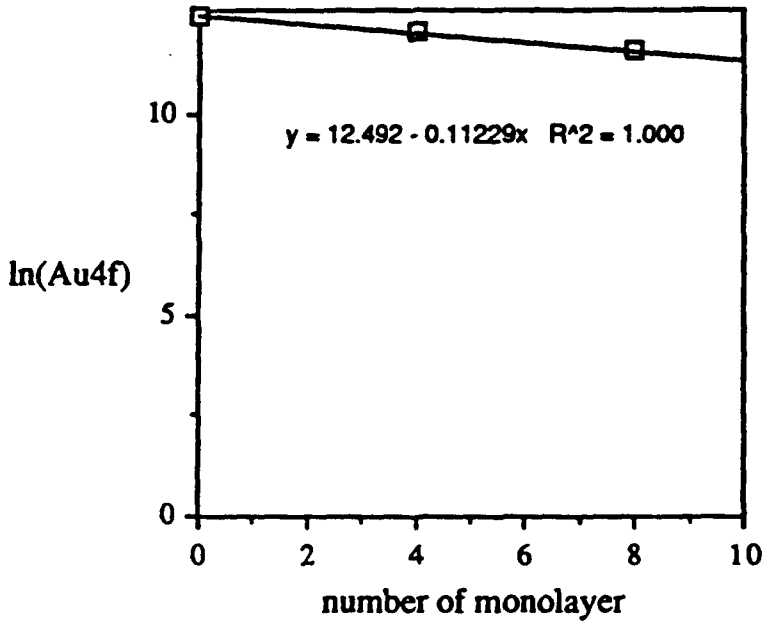

(b) IMFP measurement at take-off-angle 60°.

5. ELIMINATION OF PROXIMITY EFFECTS-EXPERIMENT

Initial experiments to verify the predictions of the previous section were carried out on a Nanometrics Cwikscan IIIE scanning electron microscope (SEM). However the availability of a Hitachi S800 SEM offered the possibility of superior gun performance at low voltages and so, despite the lack of a blanking capability, was used for the experiments described here. Most experiments were carried out at 2 KV because the simulations predicted that an energy of 2KeV was a suitable choice as the maximum energy to keep the proximity effects negligible and the minimum value to penetrate a thick enough resist layer to allow useful pattern-transfer. The resist thickness was nominally 100 nm but a more accurate measurement indicated that the corect value was 66nm. This is quite thick enough to allow patterning of 50nm chromium which could be used directly as an absorber for deep ultraviolet light or as an etch mask for silicon or silicon dioxide (S. W. J. Kuan, PhD. dissertation, Stanford University, 1988). The resist material was Poly(methyl - methacrylate) (PMMA) of Mw=188,100=1.08Mn. The substrates used were oxidized silicon (to simulate an X-ray mask when using an additive pattern transfer process) and oxididized silicon with 300nm gold (to simulate an X-ray mask proces using subtractive pattern transfer).

The test pattern used contained an isolated exposed line, equal lines and spaces, and an isolated unexposed line (fig. 5.1). The exposure levels were varied from 15$\mu C/cm^2$ to 35$\mu C/cm^2$. As predicted and previously reported the required dose is inversely proportional to the primary electron energy thus compensating exactly to the loss of beam brightness at lower energies for a given convergence angle.

The results showed that the proximity effect is indeed virtually eliminated under the above conditions for linewidths down to less than 100 nm (fig. 5.2). By measuring the linewidths as the fullwidth at half maximum of the SEM video signal we also plotted widths of exposed isolated lines and of unexposed isolated lines as a function of exposure for two different substrates (figs. 5.3). From these results we determined that the linewidth variation as a result of a 10% exposure variation (more than twice that normally allowed) is only 6nm and 9nm for the two representative substrates (table 5.1). The higher figure is for the gold substrate as expected due to the increased backscattering from the higher atomic-number substrate. These figures are within the limit of any rational specifications for feature sizes down to 100nm.

Since the use of the SEM video signal as a measure of linewidth is open to some ambiguity we also investigated the use of the atomic force microscope (AFM) as a metrology tool. This is described in the following section.

6 METROLOGY WITH THE ATOMIC FORCE MICROSCOPE.

An atomic force microscope (AFM) has been used to study the latent image in an electron beam resist, polymethylmethacrylate (PMMA). PMMA shrinks under electron bombardment and the dose dependence of this process can be characterized using optical ellipsometry. Knowledge of the dose dependence of the shrinkage gives the electron energy deposition distribution from the AFM profile. The half width of the writing electron beam can also be estimated from the AFM profile giving an unique measurement method for this difficult-to-measure quantity.

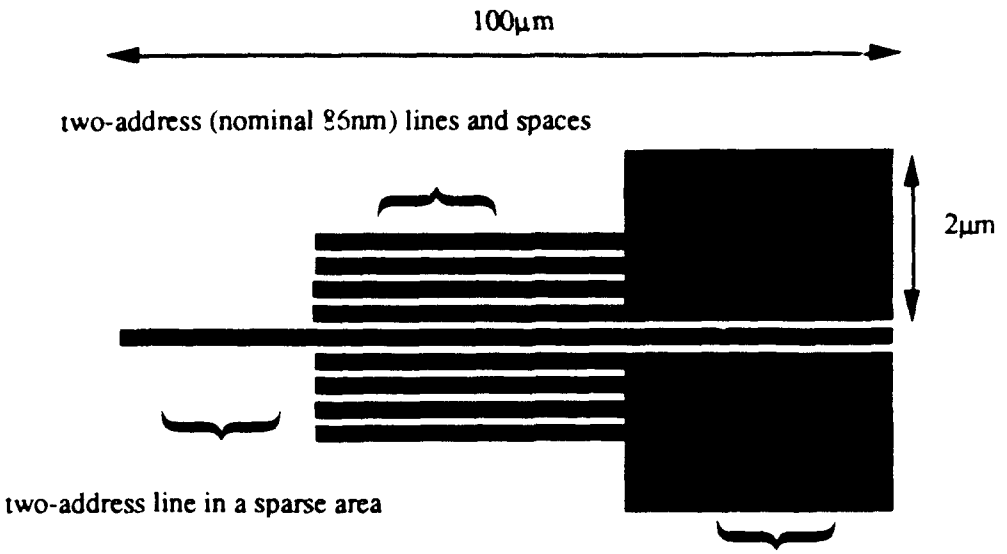

5.1

Fig. 5.1 Proximity effect pattern consists of two-address lines in dense and sparse areas. The dark areas are the exposed areas. The white areas are the unexposed areas.

	lines in sparse areas		lines in dense areas	
	$\Delta L_{10\%}$ measured	$\Delta L_{10\%}$ calculated	$\Delta L_{10\%}$ measured	$\Delta L_{10\%}$ calculated
Si	6nm	8nm	6nm	8nm
Au	9nm	10nm	9nm	10nm

$\Delta L_{10\%}$: linewidth difference for a 10% exposure variation

Table 5.1 Comparison of measured and modeled linewidth difference at 10% dose variation for two-address lines in dense and sparse area on both Si and 300nm thick gold coated Si substrates.

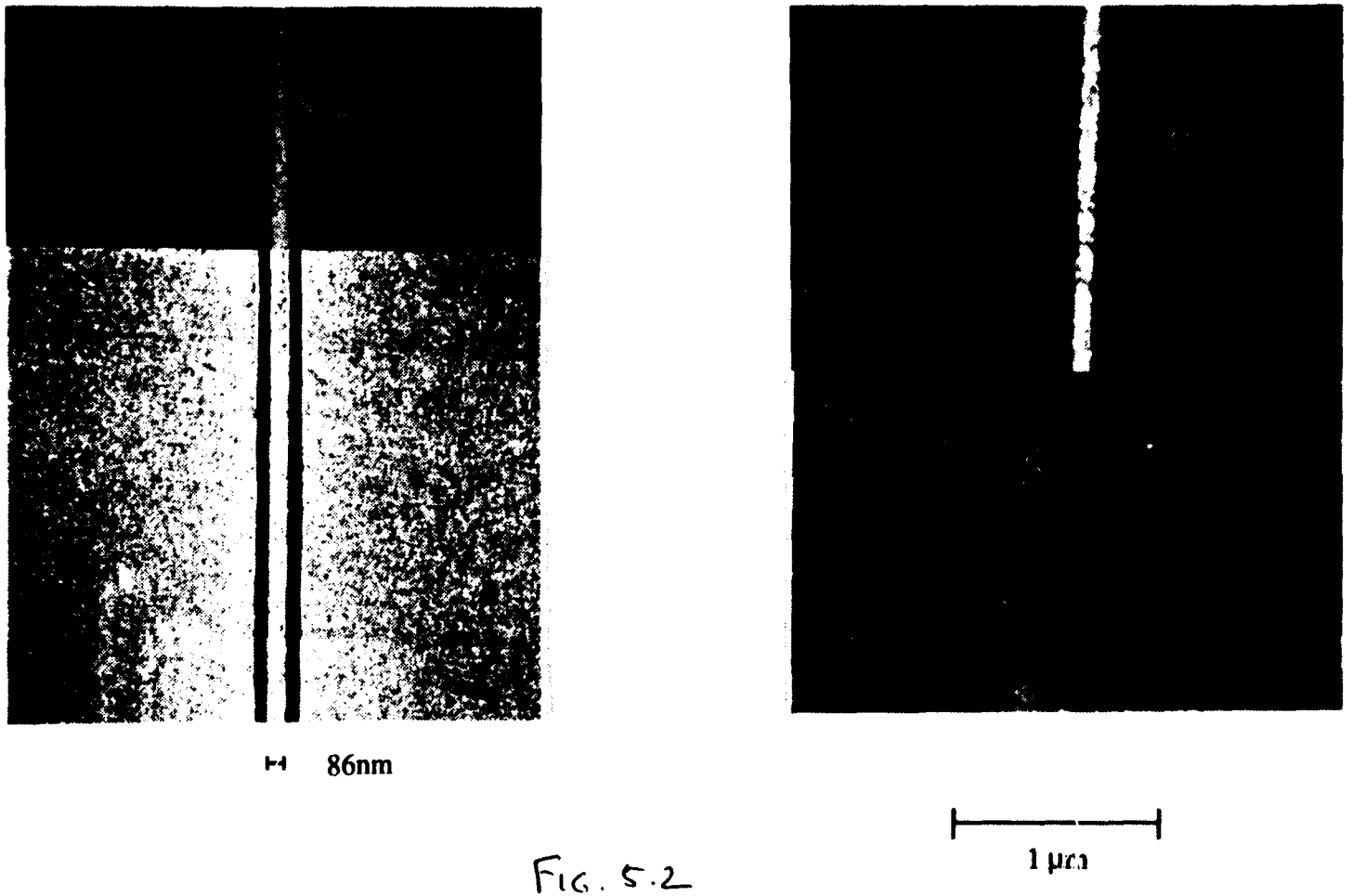

FIG. 5.2

100nm features were resolved in 60nm PMMA resist on both Si (left) and 300nm Au/Si (right) substrates.

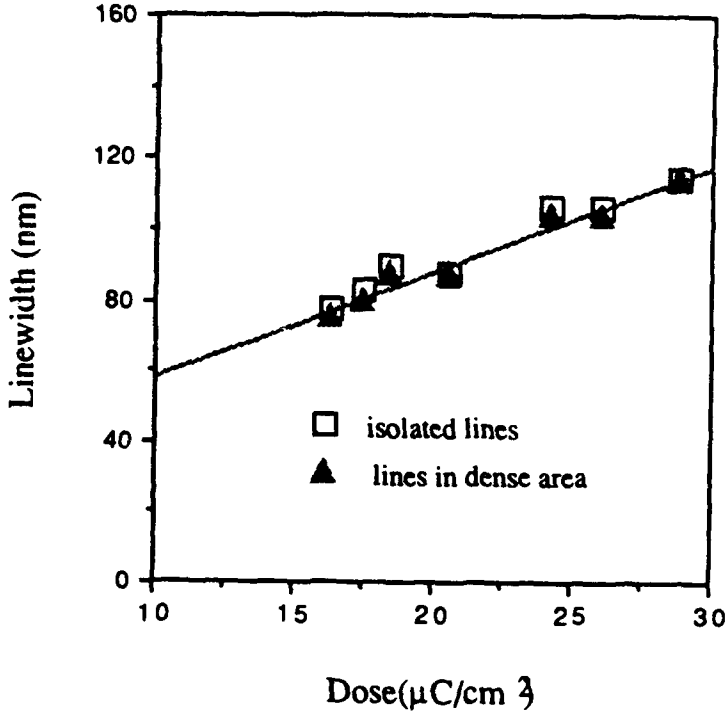

5-3(a)

Fig. Linewidths patterned on bare silicon as a function of exposure dose for 86nm features. Note (a) the absence of any effect of the density of the pattern and (b) the low sensitivity of linewidth to dose (ΔL=40nm for a 2-fold increase in dose). (c) the difference of the linewidths in dense and sparse areas is less than 8nm.

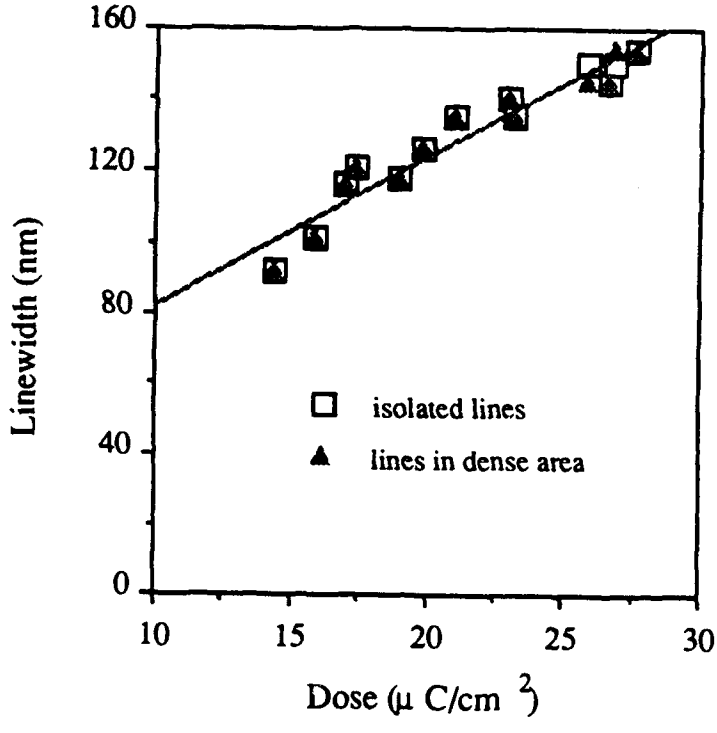

5-3(b)

Fig. Linewidths patterned on gold coated silicon substrates as a function of exposure dose for nominal 86nm features. Note (a) negligible proximity effect on these patterns, (b) the difference of the linewidths in dense and sparse areas is less than 8nm, and (c) these patterns can be resolved over a two-fold exposure range.

Several recent studies have suggested the possibility of using the atomic force microscope (AFM) as a metrology tool for electron beam resists. In the study reported here we have used the AFM to study the latent image in a resist, that is, after electron beam exposure but before the normal development of the resist. The aim of this experiment being to measure the exposed dose profile in the resist.

The resist used was 82nm of polymethylmethacrylate (PMMA) spun onto a Si wafer with a pre-exposure bake of 1hr at 120°C. All exposures used a MEBES-II electron beam lithography tool which has been modified to give both 5keV and the standard 10keV operation. The 5keV exposures are limited to 0.25 micron minimum beam size, while the minimum 10keV beam size is 0.125 micron.

A matrix of line exposures was run using three different doses 60, 180 and 600uC/cm^2. The nominal PMMA exposure dose is 60uC/cm^2. Both 0.125 and 0.25 micron single address width lines were exposed at 10keV, and 0.25 micron lines at 5keV. An AFM micrograph over an 8x10 micron area of the 0.125 micron lines exposed at 10keV and 600uC/cm^2 is shown in figure 1. The scale is exagerated in the vertical direction. The exposed lines are approximately 10nm deep which represents a 12% shrinkage of the film. As can been seen there is a great deal of detail in this image, both in cross-section and in-plane. Most of the features seen are 'real', not noise in the recording system, and give a wealth of information about the exposure process and the film topography. Some small dust particles can be seen, and some damage due to bounce of the SiO_2 cantilever over one of these is apparent as a line on the trailing edge of the particle. In other AFM scans the recording force of approximately 100nN has been reduced to 10nN to avoid such effects.

Profiles across the 0.25 micron lines exposed at 5 and 10keV and 600uC/cm^2 are shown in figure 2. The profiles have been plotted inversely, as a positive shrinkage, to emphasize that we intend to derive exposure dose distributions from these profiles. From both these figures the effects of scattering in the resist and backscattering from the Si substrate can be clearly seen. For the 5keV exposure the greater width of the forward scattering and the confined nature of the backscattering has produced an overlap of the dose distributions that has effectively broadened the linewidth. For the 10keV exposure the forward and backscattered distributions are well separated and the classic 'double Gaussian' distribution can be observed.

The results can be quantified within limits largely set by the AFM accuracy and the resist surface roughness. The AFM (Park Scientific Instruments) used a piezoelectric scanner with a 10 micron maximum scan. Thus these results are at the limit of the scan size and do show some non-linear behavior. The resist shrinkage shown in the figures here are nominal nm units, but were not calibrated for either magnitude or linearity for the distance range used in these experiments. A further limit on the accuracy of all the measurements using the line profiles is the roughness of the PMMA surface (2nm RMS) and the number of AFM image line scans that can summed without either introducing

broadening of the features or adding noise from defects. The profiles shown in figure 2 are summed over 10 linescans which is equivalent to approximately 0.4 micron in the direction of the line exposures.

A further complication in quantification is the non-linearity and scan distortion in the vertical direction due to the limited scan of the particular AFM used here. A linear and quadratic term have been removed from the linescans to give an approximately flat base line, but there is necessarily some informality about this procedure, and for the wider 10keV backscattered distributions this may introduce a significant error.

To recover the dose distribution from the AFM profiles we have used a model of resist shrinkage based on ellipsometry measurements. For these measurements 2x2mm areas were exposed with doses up to 1600uC/cm^2 at 10keV (25 times the nominal exposure dose for PMMA) and up to 500uC/cm^2 for 5keV exposures. The dependence of the resist thickness with dose and the change in the refractive index were both measured. The results of the resist thickness measurements are presented in figure 3 as the normalized resist shrinkage, $(t_0-t)/t_0$, where t_0 is the initial film thicknes and t is the exposed thickness. The maximum shinkage was 24% for a dose of 1600uC/cm^2 at 10keV, while the refractive index changed from 1.486 to 1.509 over this range. The change in the refractive index can only account for 20-25% of the resist shrinkage and the remainder is probably volatized. This is also evidenced by the pressure rise observed in the MEBES lithography tool. The combined effect of the removal of material and the densification of the resist is to produce a complex dependence of the shrinkage on dose. There are several distinct processes that may contribute to the shrinkage[4], scissioning of the polymer chains followed by relaxation, liberation of the various volatile components, each with it's own rate, and possibly recombination at broken bonds. We might therefore expect that the shinkage can be characterised by a summation of the different reaction rates removing that part of the resist that is available for the interaction with the electron beam. The ellipsometer data of the present study shown in figure 3 can be fitted to within $\pm$0.2nm using two linear rates and limits for the 5 and 10keV exposures:

$$1-t/t_0 = 0.021(1 - e^{-0.012d}) + 0.42(1 - e^{-0.00065d}) \qquad (1)$$

where t is the exposed resist thickness, t_0 the original resist thickness, and d is the dose in uC/cm^2. The pre-exponential factors represent the proportion of the resist shrinkable by one mechanism, and the exponent the rate of the process.

The profilometer results of Erasmus[5] using 0.5 micron PMMA show that the shrinkage tends to limit at 0.48 the original thickness with doses above 1000C/m^2 and the results for 10keV from Erasmus[5], which are also plotted on figure 3, require additional slower rate processes for agreement out to these large doses but are otherwise consistent with this work.

As the ellipsometer shrinkage measurements from 82nm thick resists presented here are consistent up to 600uC/cm^2 with the profilometer results of Erasmus[5] using a 0.5

micron resist, it would be expected that there would be no non-linearities associated with diffusion of volatiles through the film. Thus given the apparently high diffusivity of these volatiles there seems less likelihood of a build-up of material just out of the electron beam.

In the range of doses reported here the shrinkage given by equation 1 is also seen at other energies and for microscopic structures. Figure 4 shows linescans for 5keV exposures at three different doses. The peak heights, which are plotted in figure 3 follow the same dose dependence as the results for the 10keV area exposures. This can be understood if the backscattering factor is near unity as then the peak height of the 5keV line exposure will be at approximately the same deposited energy as the 10keV area exposure. The results of Erasmus[5] show that the shrinkage scales approximately linearly with deposited energy and are consistent with our Monte Carlo simulation which gives a ratio of 1:1.85:2 for 5, 10, and 20keV exposures in 0.5 micron resists.

The half width of the forward scattering distribution for the 0.25 micron lines at 10keV from figure 2b is 0.26 micron, which equates to 0.23 micron using the dose dependence of equation 1. The backscattering distribution is found to be 0.7 of the dose of the forward distribution (assuming no overlap between lines). The narrower than expected forward distribution is in fact consistent with the MEBES method of estimating the beam profile width by measuring across an edge. Apart from the error associated with the non-linear scan of this particular AFM, this method represents a more realistic estimate for this notoriously difficult-to-measure quantity.

The half width of the 5keV 0.25 micron profile is 0.49 micron on the linear plot of figure 2a which equates to a 0.42 micron dose distribution. The line broadening observed experimentally is consistent with the overlap of the forward and backscattered distributions from Monte-Carlo calculations.

The results reported here demonstrate that direct measurements of the electron beam dose profiles in a resist can be made using an AFM. Besides giving a measure of the electron beam half width, the technique can be used to quantify proximity effects, and any dose distribution on a free surface that can be coated with PMMA.

References

1. J.C. Shaw, S.A.Rishton, R.R.Jackson, and M.P.O'Boyle, Appl. Phys. Lett. 58, 21 (1991)

2.Y.Martin, C.C.Williams, and H.K.Wickramasinghe, J. Appl. Phys. 61, 4723 (1987)

3. C.R.K.Marrian, E.A.Dobisz and R.J.Colton, JVST **B5**,1367 (1991)

4. J.O.Choi, J.A.Moore, J.C.Corelli, J.P.Silverman, H.Bakhru, JVST **B6**, 2286 (1988)

5. S.J.Erasmus, J. Vac. Sci. Technol. **B5**, 409 (1987)

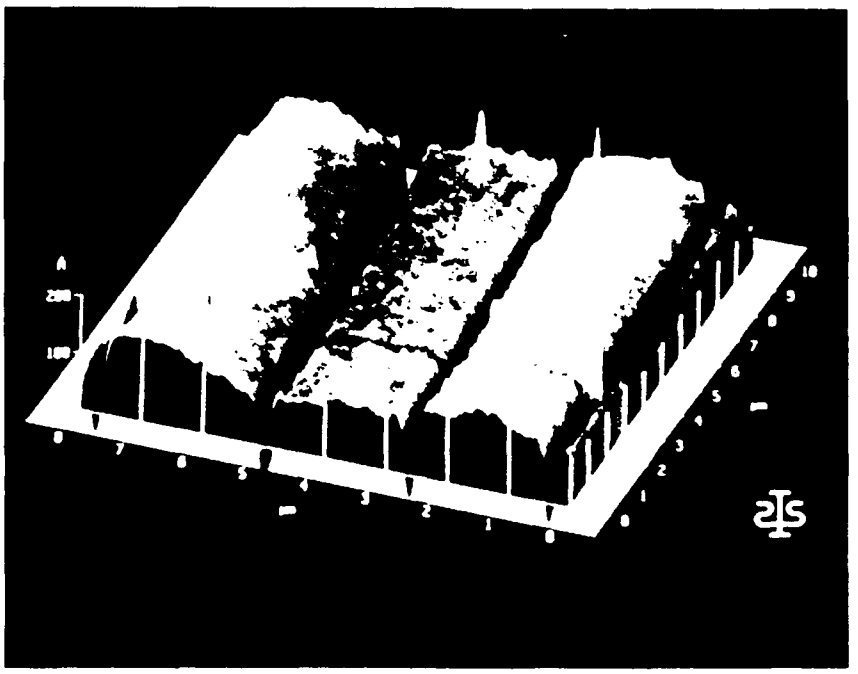

AFM micrograph of the latent image of e-beam exposed lines.

Figure 1.

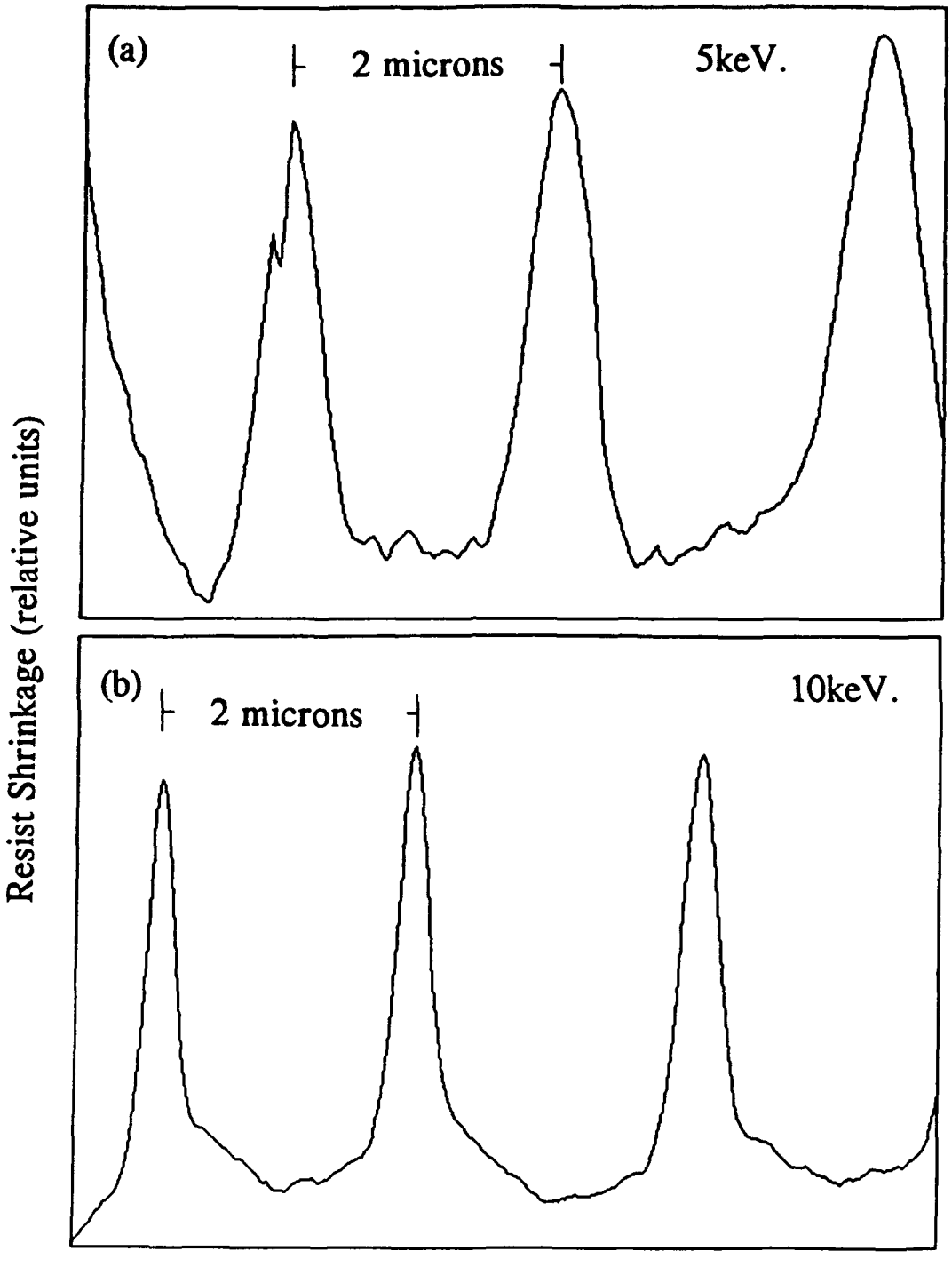
(a)
2 microns
5keV.
(b)
2 microns
10keV.
Resist Shrinkage (relative units)
Scan Distance

Figure 2.

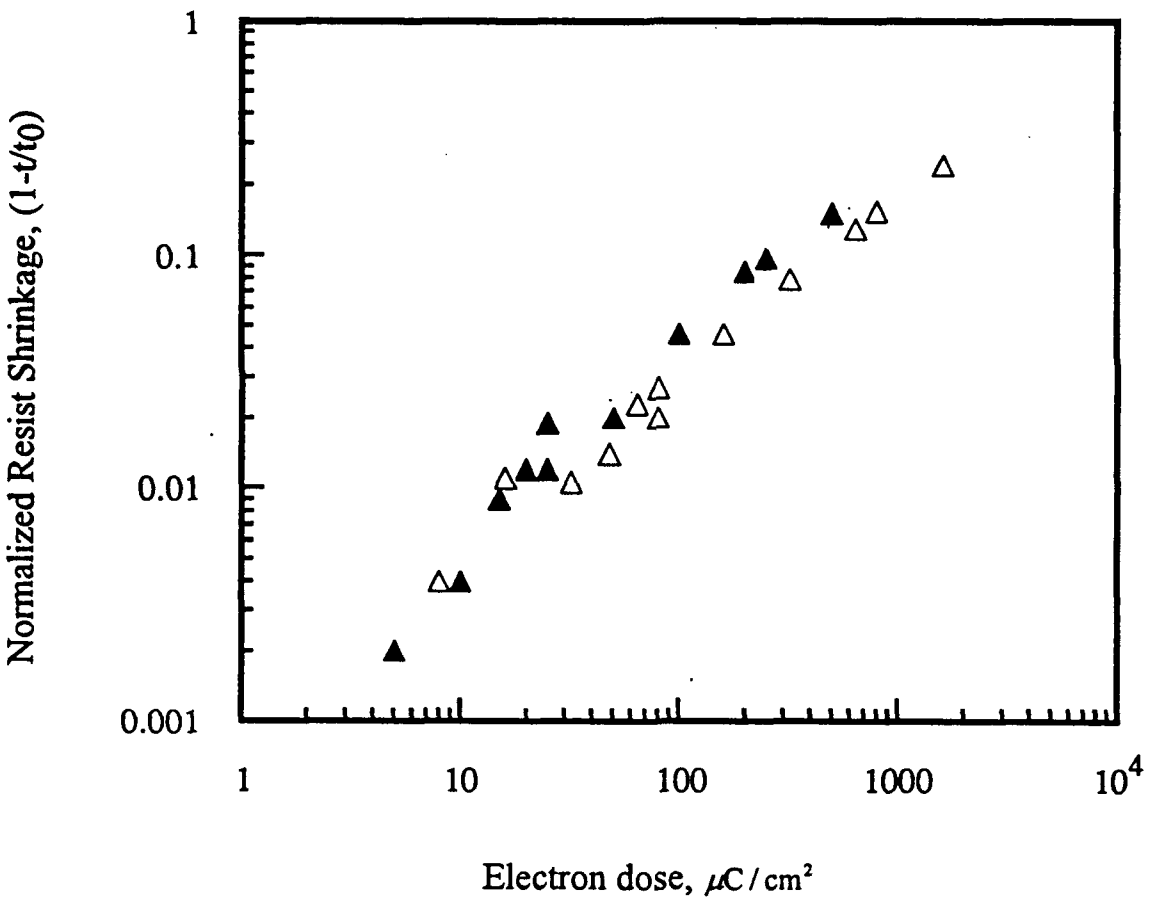
Normalized Resist Shrinkage, (1-t/t0)
1
0.1
0.01
0.001
1
10
100
1000
10^4
Electron dose, μC / cm²

Figure 3

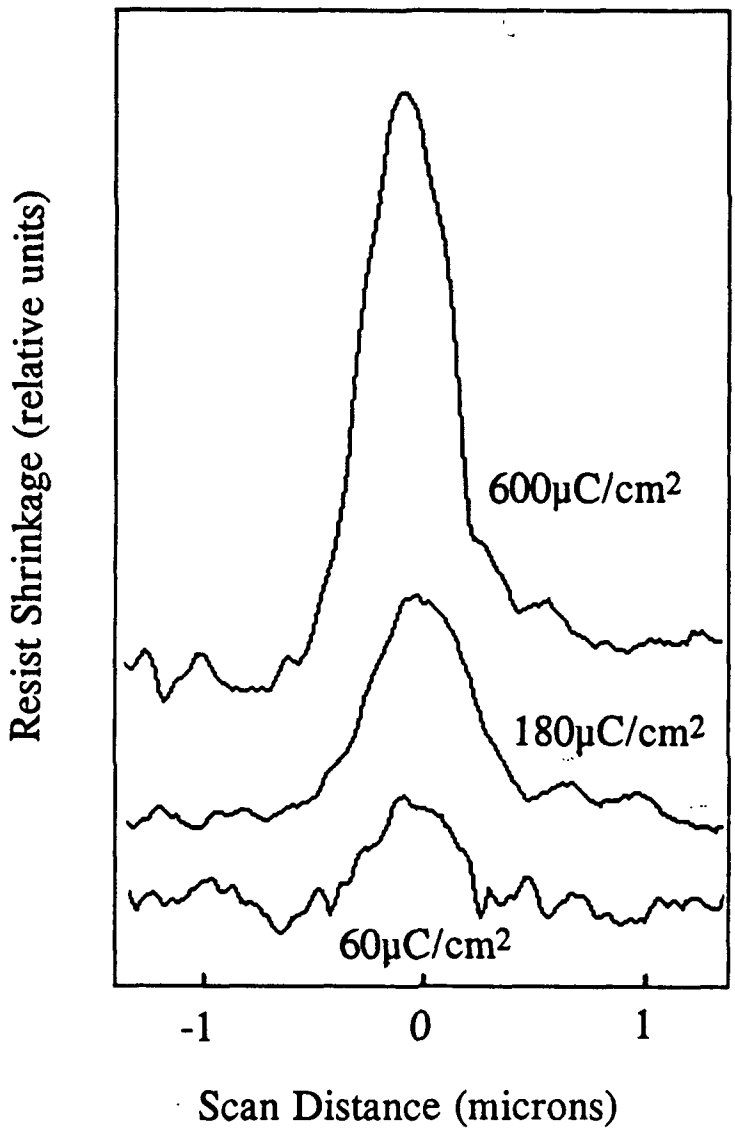
Resist Shrinkage (relative units)
600μC/cm2
180μC/cm2
60μC/cm2
-1
0
1
Scan Distance (microns)

Figure 4.

7. BRIEF REVIEW OF PERFORMANCE OF LOW VOLTAGE ELECTRON OPTICS

There is now a substantial body of work pointing out the that the penalty of moving to low energy electrons (increased minimum beam diameter and reduced available current density) is much less than indicated in traditional electron optical analysis.

There have been several developments leading to this change of mind:
1. The possibility of using a projection lens in which the workpiece is immersed in the focusing field.

2. In particular the use of a retarding field as the focusing field.

3. The use of a retarding field followed by a field-free region for hte workpiece (Meisburger et al. EIPBT symposium, Orlando, Fla., June 1992)

4. The introduction of low-energy -spread electron emitters such as thermal-field emitters.

Although we have not yet determined the optimum configuration for a low voltage electron beam column for lithography it is clear that we can, using some of the above developments obtain some very attractive results.

For example if we assume that we employ a thermal field emitter with an energy spread ∂V of 1 eV and virtually unlimited brightness then, neglecting space charge we can estimste the minimum beam diameter obtainable using purely magnetic focusing. A very simple lens, and probably the optimum for this example, is that of a uniform axial field B (that extends to the image plane) for which the chromatic aberration coefficient, Cc, is minimized by choosing the largest practical value of B, about 1T for a conventional magnet.

It is easily shown that, for large demagnification, the focal length is given by

$$f = -1/k = \frac{1}{B}\sqrt{\frac{8mV}{e}}$$

and the chromatic aberration coefficient is given by

$$C_c = \frac{\pi}{4} f = \frac{\pi}{4}\frac{1}{B}\sqrt{\frac{8mV}{e}}$$

For a low voltage column the dominant aberration is chromatic giving rise to a disk of confusion of diameter:

$$d_c = C_c \frac{\partial V}{V}\alpha = \frac{\pi}{4}\frac{1}{B}\sqrt{\frac{8m}{eV}}\partial V\ \alpha$$

The diameter of the Airy disk (diffraction) is given by:

$$d_f = \frac{12}{\sqrt{V}}\alpha^{-1}\ \text{Å}$$

The combined diameter can be expressed as:

$$d=\sqrt{d_f^2+d_c^2}$$

which has a minimum value when $\alpha = \sqrt{\frac{24B}{\pi\partial V}\sqrt{\frac{e}{2m}}}\ 10^{-5}$ rad

$$\text{for } \partial V=1eV \text{ and } B=1T,\ \alpha_{opt}=15mrad.$$

$$\text{so that } d_{min} = 1.4d_{cmin} = 1.4\ d_{fmin} = \frac{1200}{\sqrt{V}}\ \text{Å}$$

Thus, for purely magnetic focusing with conventional magnets our lower limit of beam diameter for V=2000V is about 3 nm. This is quite small enough for our envisaged mask making. How close we can approach this limit when space charge effects and finite brightness have to be taken into account is the subject of current work.

Another configuration that has been described for low voltage electron optics is the retarding field operation. In its simplest form a uniform retarding field is set up between the (flat) target and the flat surface of the final electrode of the beam forming system. If the target potential, V << electrode potential, V_e, (relative to the source) then the field is V_e/d where d is the electrode-to-target distance and most of the focusing takes place in tfeh retarding field. Assuming parabolic trajectories the chromatic aberration of this retarding field lens is given by

$$Cc= d\frac{V}{V_e}.$$

The minmum value of d is set by the maximum practical field, about 10^7V/m. Thus at best:

$$Cc= V10^{-7}m$$

$$\text{and } d_c = \partial V10^{-7}\alpha\ m.$$

Proceeding as before: $\alpha_{opt} = \sqrt{\frac{10\text{-}2}{\partial V\sqrt{V}}}$

and so the minimum value of d is given by;

$$d_{min} = 14\sqrt{\frac{\partial V}{\sqrt{V}}}\ nm$$

Thus for V=2000V and ∂V=1eV, d_{min} = 2.2 nm which is marginally better than the result with magnetic only.

The best result might be expected to be when both focusing fields overlap. Again that case is being studied under the current contract.

However it is abundantly clear that the possibility now exists for obtaining very fine probes for low voltage lithography.

8.SILICON CALIBRATION STANDARD FOR HIGH PRECISION PATTERN GENERATORS

Achieving accurate overlay in microlithographic processing is one of the key requirements in pushing to higher density integrated circuits. For X-ray and 1x lithography, minimizing the errors is hampered by the lack of a suitable reference against which to check mask and electron beam tool distortion. Initial studies show the feasibility of making a high accuracy distortion standard based on the crystal lattice of unstressed Si wafers. The aim of the standard is to facilitate the measurement of distortion by providing a working reference of high accuracy.

A Si crystal has the property that when cut and polished along the (100) face, the crystal can be anisotropically etched along orthogonal [110] directions leaving four (111) faces. Under the right conditions lithographically exposed lines will self align to the crystal axis and on unstrained Si can give the straightness and orthogonality required for a distortion standard. Initial experiments were performed using a Canon stepper for optical exposures. Standard 3 inch wafers were exposed with a series of lines and squares. The pattern was steeped nine times, and at each step the pattern was rotated through~0.2^{o} to cover the wafer flat alignment error. A nitride mask is first etched with the lithographically defined line. Then a KOH solution is used to anisotropically etch the wafer. The Si etches the (100) planes preferentially and is stopped by the (111) planes. This leaves a V shaped feature in the wafer which extends along the (100) direction, and in a perfect etch the feature has no steps along the (111) planes.

Figure 1 and 2 show SEM micrographs from exposures with different alignments. In figure 1 the SEM is looking down into V shaped grooves comprising two (111) faces oriented in the [110] direction. The dark narrow lines are the centers of the grooves shown schematically in figure 1c. In figure 1a the wafer was well aligned and no steps are visible. In figure 1b the series of steps shows that the lithography is not well aligned to the crystal direction, and there are many steps on the (111) faces. Figure 2 shows the effects of alignment of an etched square. Here the four (111) faces can been seen.

One of the critical steps in the production of distortion standard is the demonstration that long defect free lines can be etched into Si and one unknown is how accurately the initial exposed lines need to be aligned to the Si crystal axis. For this demonstration we have made a Cr on glass photo mask in the MBES for the contact printing of lines on a (100) Si wafer. The lithographic pattern consists of multiple lines 100mm in length arranged as a fan at 0.4mradian intervals over a 2^{o} range. There are three groups of these lines and also a set of square features. The initial exposures are very encouraging. In these first exposures it was not realized that the Cannon printer skewed the alignment but there was sufficient range in the fan for the outer lines to be etched with a very small number of steps being detected in the SEM per cm. The detection limit for the size of these steps being approximately 100nm. Figure 3 shows a micrograph of a nearly aligned line. The micrograph is of of the V shaped line in plane view. The dark line running along the center of the micrograph being the bottom of the V, the self stopping point. The lighter features at the edges of the V is the nitride mask, which has been undercut. There are very few steps in the line which shows the concept of using

the fan of lines to find the crystal axis does indeed work. The jagged edge of the nitride mask in figure 3 is from the ETEC-MEBES photomask, and is due to the aliasing error made in writing a sloped line. It can be seen that the anisotropic etch ingnores these aliasing errors. The vertex here was imaged by inverting the SEM contrast and shows this is a very sharp feature and a good high contrast target for electron beam metrology.

Figure 1. Aligned and misaligned etched lines in Si.

a) Aligned

b) misaligned

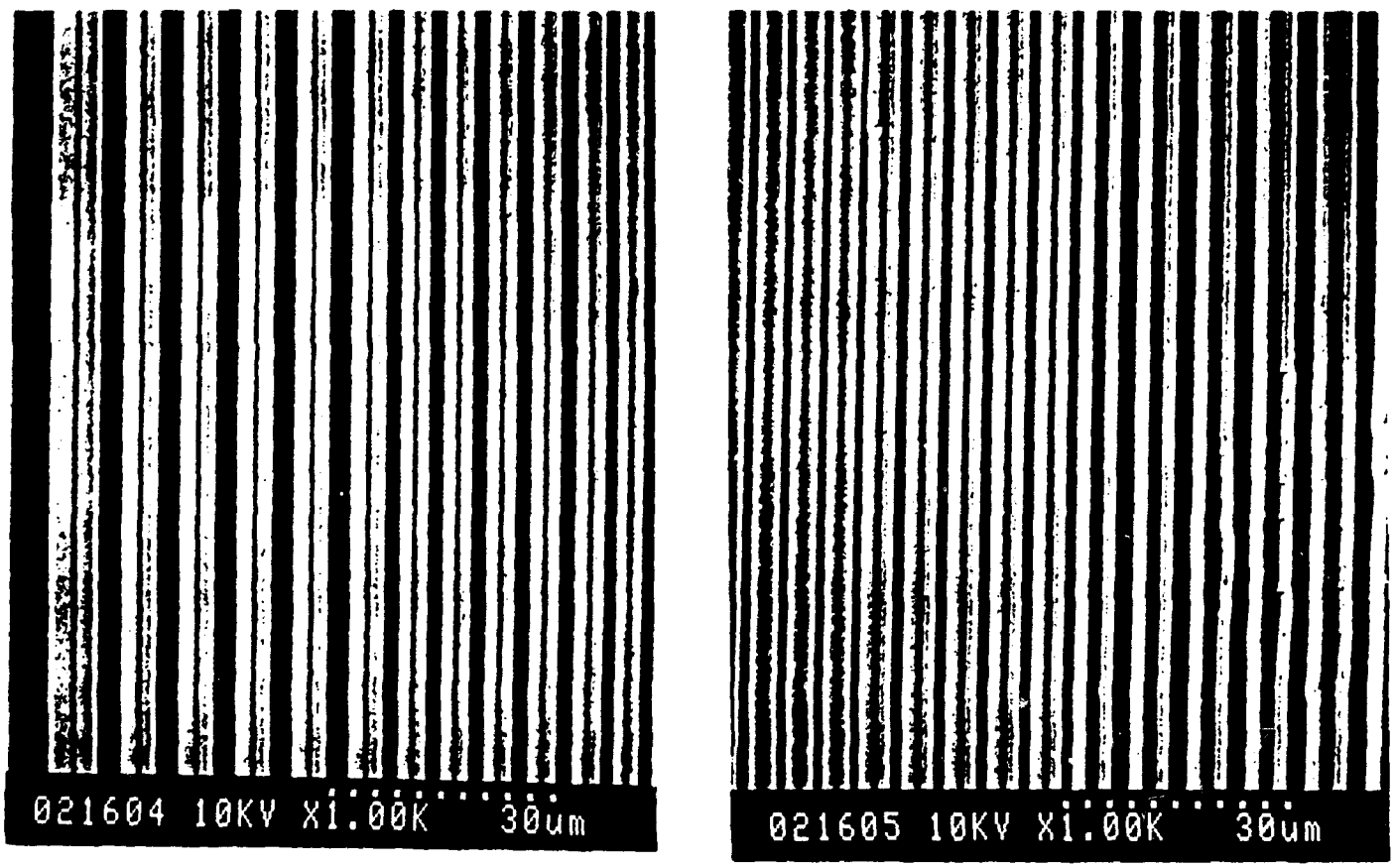

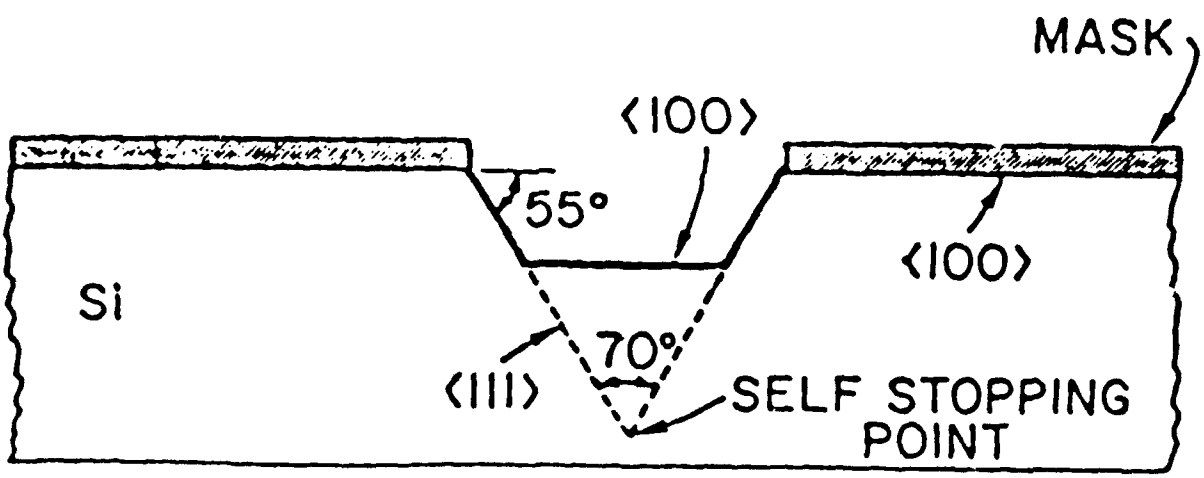

c) Schematic section of lines anisotropically etched into (100) Si.

Figure 2 Square features anisotropically etched into Si (100)

a) Feature aligned

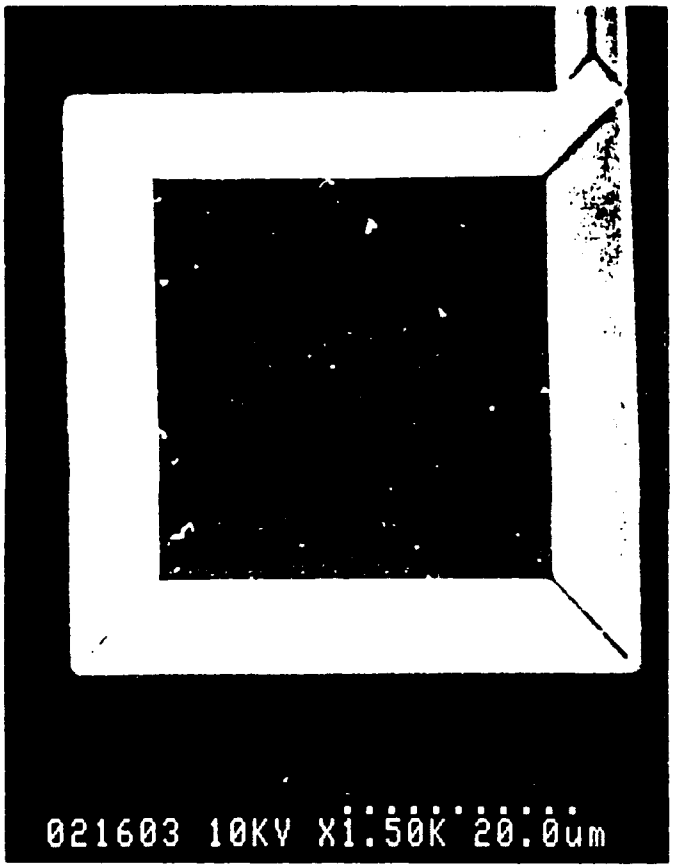

b) Feature misaligned

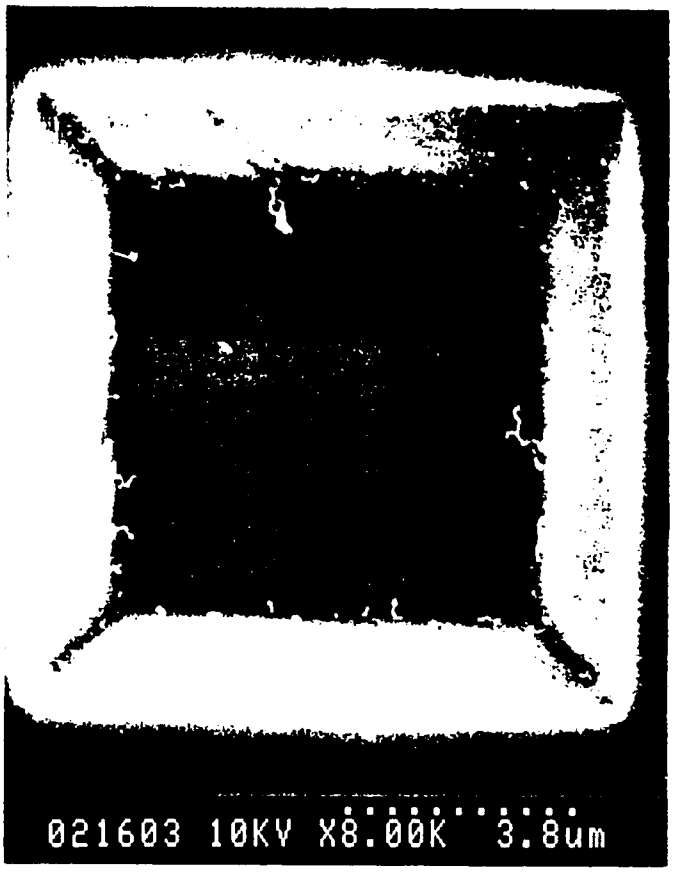

Figure 3. Correction of MEBES aliasing errors.

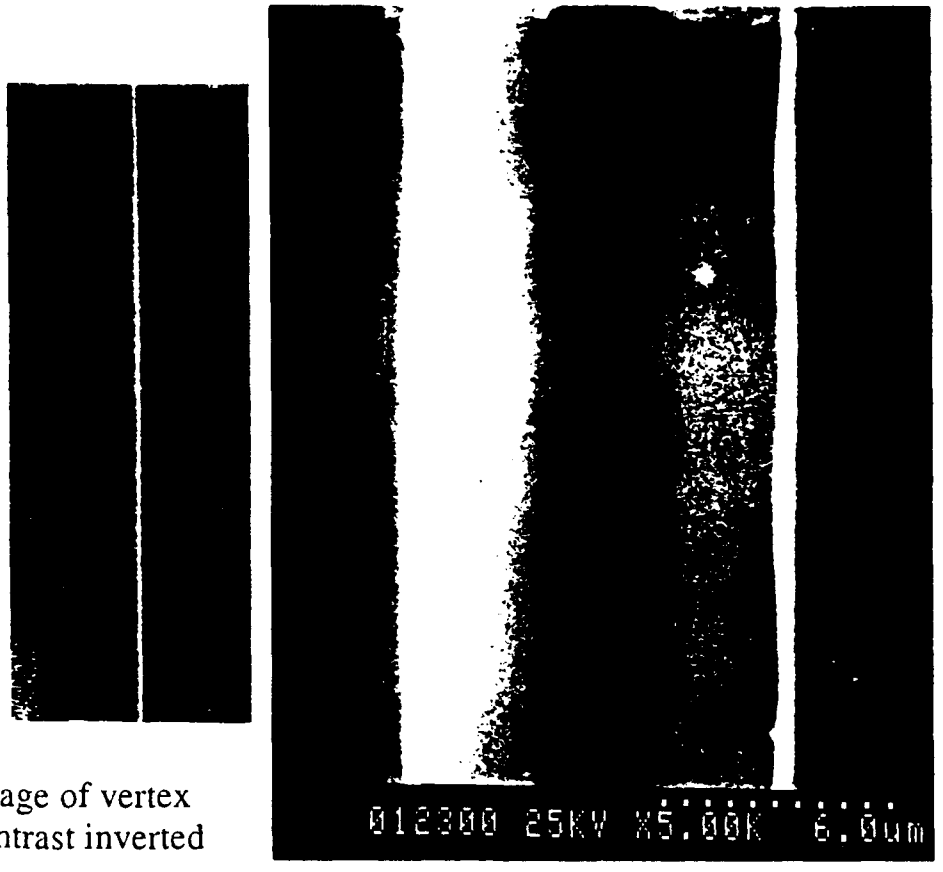

Image of vertex
contrast inverted

The edge roughness of the nitride mask tech mask (light feature) caused by MEBES aliasing error is not present at the vertex of an anisotropically etched line in the Si [100] direction.

9. Appendix 1
Submicron Maskmaking for Optical and X-ray Mask Making Using GHOST Proximity Effect Correction.
Robert Dean, ETEC COrporation

Interim Proximity Effect Correction

A Subcontract in Support of High-Precision X-Ray Lithography Masks

Contract Number PR 6975
Stanford University

FINAL REPORT

Submicron Maskmaking for Optical and X-Ray Masks Using GHOST Proximity Effect Compensation

March 1991

Prepared by
Etec Systems, Inc
26460 Corporate Avenue
Hayward, California 94545

COPYRIGHT

TRADEMARKS

INTRODUCTION

One of the major difficulties of manufacturing either optical or x-ray masks with submicron features is the proximity effect. Electron scattering causes the proximity effect by overexposing dense features and underexposing isolated features. Most scattered electrons fall within a range of one micron from the edge of an electron beam during exposure of the substrate. Therefore, the proximity effect is less important for the large feature masks that are currently manufactured. However, attempts to manufacture both optical and x-ray mask_ th half- to quarter-micron design rules has required correction for the proximity effect.

At Etec we have chosen the GHOST™ method to compensate for the proximity effect. GHOST works by exposing the reverse image of a primary pattern at about one-half the dose of the primary pattern, using a large spot beam but at the same address. The result smooths the energy density profile deposited in the resist along the edges of the pattern and equalizes the dose between features. Figure 1 illustrates typical energy density profiles of an uncorrected primary exposure, the correction exposure, and the resultant corrected exposure where the two exposures are superimposed.

The goals of this project were the following:

- Verify theoretical GHOST parameters for both inter- and intraproximity effect.
- Compare the differences between patterns written with GHOST and patterns written without GHOST on optical masks.
- Quantify changes in the proximity effect to features as small as 0.3 micron on both optical and x-ray substrates with isolated opaque and clear lines from chip to chip in an array written at optimum parameters.
- Determine the minimum resolution obtainable.
- Determine linewidth uniformity and line edge roughness.
- Transfer patterns developed on a resist film on x-ray trilayer substrates to plated gold features. Characterize, showing that 0.5-μm lithography can be achieved with linewidth uniformity of less than or equal to ±5% of the nominal linewidth.

RESULTS

Verification of SAMPLE Parameters for GHOST on Optical and X-Ray Substrates

GHOST parameters for optical and x-ray trilayer substrates were determined with SAMPLE. The parameters were for 3000Å of AZ™ 5206 resist on 800Å of midreflective chrome on a quartz substrate for optical masks. For x-ray masks, the substrate was a trilayer of 3000Å of AZ 5206 resist on 300Å of bright chrome on 0.7 to 1.0 μm of hard-baked resist or polyimide, on a gold/tantalum plating base. The trilayer is illustrated in Figure 2.

A 6x6 array dose/correction ratio series was written on both substrates with the optimum theoretical values in the center of the array. For optical substrates, the array ranged from a dose of 7.5 to 9.5 μC and a correction ratio of 0.35 to 0.54 Q_c/Q_p for the optical masks with a 0.1 μm primary spot size and a 0.58 μm correction spot size. For the x-ray

substrates, the array ranged from 7.5 to 9.0 Q_c/Q_p and 0.33 to 0.55 Q_c/Q_p with a 0.1 μm spot size for the primary beam and a 0.8 μm spot size for the correction beam. The arrays were generated by the GHOST Process Evaluation Tool (GPET) program.

A process was worked out for each substrate. Development was done with undiluted PPD 450, which allows iterative developments. End points were chosen by measuring linewidths of 4.000 μm lines at several development times on different plates to characterize all doses. With optical masks the initial development time was 32 seconds followed by one or more 5-second iterations. The optical arrays were then etched, coated with 100Å of gold, and examined in an SEM for proximity effect. The process for the x-ray substrates varied little from that of the optical substrates; it was 34 seconds, again followed by various numbers of iterations. The x-ray substrates needed fewer iterations to characterize all of the chips in the array, and there was a much smaller proximity effect on the chrome/resist substrate than was observed on the chrome/quartz substrate. The development time required varied over time for both substrates. A turnkey process is being developed with internal funding for GHOSTed substrates.

The optimum parameters were determined by examination of CDs of 2.000, 1.000, 0.500, 0.400, and 0.300 μm isolated opaque and clear lines, and a grating structure to determine intraproximity effect and dagger structures to determine interproximity effects. Figures 3 through 5 illustrate these features. The approach was to find where CD-nominal of clear and opaque lines in each of these features begin to increase beyond normal noise differences. (In cases where features were over- or underdeveloped, the absolute value of CD-nominal for clear and opaque features was compared and proximity effect was determined when these values were not equal beyond normal noise.)

The results showed that proximity effect was fully corrected to 0.35 μm at 9.00 μC dose at a 0.1 μm primary spot size and Q_c/Q_p of 0.42 at a 0.58 μm correction spot size on optical masks. There was some distortion of opaque dagger lines when the clear feature on either side was 0.2 μm. This distortion was also observed in some, but not all cases with 0.3 μm clear features on either side. The distortion was not observed on other features as small as 0.3 μm. The difference is probably explained by slight differences in the MEBES column setups in the size of the primary and correction spot sizes, and slight differences in the dose. Based on these results, we maintain that the proximity effect is fully corrected to 0.35 μm for etched chrome on optical masks. The distortion discussed is observed in Figure 6, a micrograph of an opaque dagger pattern.

The results for x-ray substrates were determined by SEM evaluation as before, except that we evaluated the gold-coated resist rather than etched chrome. The results showed that a much smaller proximity effect is observed with this substrate. This is probably due to fewer backscattered electrons from the mostly carbon substrate. Almost any of the chips in the array could have been chosen for the parameters by our method of evaluation. We chose 8.8 μC at a 0.1 μm spot with Q_c/Q_p set at 0.50. At this value, no distortions were observed on any of the features to 0.3 μm. Based on these results, the lithography on trilayer x-ray substrates is fully corrected to 0.3 μm and may be good to smaller features. Figure 7 is a micrograph of the dagger pattern in developed resist on a trilayer.

Qualitative Comparison of Corrected and Uncorrected Patterns

Patterns of isolated lines and spaces, grating patterns, and dagger patterns in chrome are compared in Figures 8 through 11. Figure 8 compares corrected and uncorrected clear and

opaque dagger patterns for 0.4 μm lines. The proximity effect becomes apparent in the uncorrected pattern beginning at about 0.6 μm and degrades as the feature becomes smaller. The corrected feature shows only a small proximity effect for the opaque line at the 0.2 μm space.

Figure 9 compares two gratings of 0.3 μm features. The proximity effect is apparent without GHOST. The isolated clear lines are not developed out, the isolated opaque lines are narrower than the lines and spaces, the isolated opaque pad is almost etched away, and the clear pads are not etched. The corrected version shows all features, each of them having approximately the correct dimensions.

Figure 10 shows a reverse tone of Figure 9 at a higher magnification. Similar effects are observed.

Figure 11 shows isolated clear crosses. Many of these, at different sizes, were measured both with an SEM and with the EDGE measurement system in MEBES® to quantitatively determine uniformity and the proximity effect in a 3x3-cm 6x6 array of chips written at the optimum dose. The isolated 0.3 μm uncorrected line does not develop out except at the cross where there is a larger dose due to backscttered electrons.

Quantitative Measurement of the Proximity Effect Measuring Isolated Clear and Opaque Lines with SEM and EDGE

A 3x3-cm array of 36 chips containing clear and opaque crosses 2.000, 1.000, 0.500, 0.400, and 0.300 μm in diameter were written at the optimum GHOST parameters on chrome on quartz substrates, developed and etched, and measured with SEM and EDGE. The results were determined by taking micrographs of the crosses as shown in Figure 11. Four measurements were taken on each of the 36 crosses, one from each chip. Measurements were taken on both clear and opaque features. EDGE measured 72 lines, 71 times each. Table 1 presents the SEM data for both GHOSTed and unGHOSTed plates. Mean CDs, mean deviation from nominal, and 3 sigma values are presented. Table 2 presents the EDGE data for a GHOSTed plate. Uncorrected plates were not read with EDGE.

Figures 12 and 13 plot the data produced by EDGE. Figure 12 is a plot of the mean linewidth obtained from EDGE data versus feature size for clear lines in x. All the values vary by less than 0.012 μm from nominal. The proximity effect that would be seen with simple change in size is only slightly apparent at the 0.3 μm line, on the order of 0.01 to 0.02 μm correcting for the overdevelopment of the plate. The error bars are the 3 sigma variation of the lines. Figure 13 plots the data for opaque lines in x. All but the 0.3 μm lines are within 0.013 μm of nominal. The 0.3 μm line is within 0.032 μm of nominal. Correcting for overdevelopment, the line is within 0.02 μm. The difference between the two lines shown in Figures 12 and 13 can be explained in terms of the degree of development or etch. The lines were overdeveloped or overetched by approximately 0.01 μm. The dropoff of the 0.3 μm lines may be the beginning of a proximity effect. Figure 14 compares this data with lines measured by SEM on an uncorrected mask. The solid lines represent the uncorrected features and the dashed lines the corrected features. The amount of proximity effect observed between the two is evident in the slope of the solid uncorrected lines as the features get smaller. The results show little proximity effect for the corrected patterns to 0.3 μm relative to the uncorrected values. For uncorrected opaque lines, the proximity effect is –0.04, –0.065, and –0.01 μm for 0.5, 0.4 and 0.3 μm

lines, respectively. For clear lines correcting for overdevelopment, the values are –0.06, –0.1 and –0.3 for the respective lines. Corrected lines show a dropoff of about 0.01 to 0.02 μm that could be a result of the proximity effect. For this reason, we set full correction at 0.35 rather than 0.3 μm.

Similar plots are shown in Figures 15 through 20 for resist features on the trilayer. The values are very close to nominal for all features. The 0.3 μm lines do not begin to drop off in these plots as they do with the chrome on glass substrates. Therefore, the proximity effect is fully corrected on the trilayer to 0.3 μm. The difference when the two are compared is probably due to fewer backscattered electrons in the trilayer due to the carbon based substrate. This is also born out in the large choice noted before when determining parameters in the dose/correction series on the trilayer. The error bars are maximum minus minimum values.

Determination of Minimum Resolution

Features as small as 0.3 μm in proximity patterns are relatively easy to produce with the current process for chrome on quartz. One can process to 4.000 μm lines and produce 0.3 μm features repeatable where linewidth varies by less than ±5% of the nominal linewidth. In about 20% of the cases, 0.2 μm features can also be produced. Figures 21 and 22 show 0.2 μm features in resist. Figures 22 and 23 show features etched in chrome. When linewidths are mixed as in Figures 22 and 23, 0.2 μm CDs are much easier to process. We believe that further work may improve the resolution we can consistently obtain to 0.2 lines. Additionally, proximity effect compensation may be improved by using smaller spot sizes for the primary beam that will be possible with MEBES IV. Lines of 0.2 μm were easy to produce repeatably in the resist on a trilayer but were not evaluated. A micrograph is shown in Figure 24.

Determination of Uniformity and Line Edge Roughness

The 3 sigma values listed in Tables 1 and 2 represent line edge uniformities. It can be seen from the data that the uniformities improve with the GHOST process. The 3 sigma value is on the order of 0.04 μm for GHOSTed features, while it is around 0.07 for the uncorrected features. This is explained by the general smoothing of the exposure along the edges of the lines by GHOST. Improvement of uniformity is also observed with other techniques that smooth the exposure at the edges, such as sizing the data and MPP™, which introduces gray levels of exposure at the edges.

Line edge roughness (LER) values determined by EDGE are listed in Table 3. The values for all lines vary from 0.037 to 0.055 μm. The average is 0.041 μm. These values are typical of the type of line edge roughness seen in the cross depicted in Figure 11. This value is within spec for a MEBES III, but is relatively high for features in the 0.3 μm range. There are several ways to improve these values:

- The first is to achieve a primary spot size of as close to 0.1 μm as possible. Normally, spots sizes are larger than this by 10 to 20%. Comparison of machine data on spot size has implied that larger spot sizes result in greater line edge roughness. We have not confirmed this by experiment.
- Second, improve the current process. A slower process with no iterative developments will also improve LER.

- Third, sizing the data also improves the LER.
- Finally, other resists such as PBS show much better LER. Very smooth edges are observed in the micrographs shown in Figure 25, which were done with GHOSTed PBS.

Evaluation of Simulated X-Ray Masks Written on Trilayers

Five masks simulating x-ray substrates were written and sent to Du Pont, Danbury, for gold plating. They were returned and evaluated. Micrographs are shown in Figures 26 through 28.

The evaluation showed that a process bias was introduced during the processing of the x-ray substrates at Du Pont. The bias varied from 0.15 to 0.2 μm. In addition, the bias was different for clear and opaque features. For example, Table 4 lists the mean linewidths at various feature sizes along with the bias and 3 sigma deviations from the mean for 32 measurements.

Table 4 illustrates the bias and the shift in the bias with the size of the clear features. Comparison of these values with the values of lines etched in chrome and resist lines on the x-ray substrates indicated that the bias and shift is introduced in the process during the gold plating process or RIE. It should be noted that the substrates that were plated were not sized to account for process-induced bias. However, a plate was included that had a dose series written on it. Patterns that were underdeveloped showed much less bias and shift from nominal. It is believed that 0.5 μm resolution can be accomplished through gold plate with the trilayer process as it is now. Lithographic quality in terms of uniformity, including 3 sigma values and values of less than ±5% of the nominal linewidth, may not be accomplished with the process as it is now.

APPENDIX

Table 1. SEM Data of GHOSTed and unGHOSTed Patterns

a. Mean Linewidths, GHOSTed

Nominal linewidth (microns)	Tone (all values in microns)		
	Clear	Opaque	All lines
1.0	1.001	0.992	0.997
0.5	0.505	0.499	0.502
0.4	0.405	0.398	0.401
0.3	0.300	0.293	0.296

b. Mean Linewidths, unGHOSTed

Nominal linewidth (microns)	Tone (all values in microns)		
	Clear	Opaque	All lines
1.0	1.073	0.993	1.033
0.5	0.504	0.457	0.481
0.4	0.360	0.335	0.347
0.3*	0	0.203	—

* 0.3 clear lines did not develop out.

c. Mean Deviation from Nominal Linewidth, GHOSTed lines

Nominal linewidth (microns)	Tone (all values in microns)		
	Clear	Opaque	All lines
1.0	0.001	–0.008	–0.004
0.5	0.005	–0.001	0.002
0.4	0.001	–0.002	0.001
0.3	0	–0.007	–0.004

d. Mean Deviation from Nominal Linewidth, unGHOSTed lines

Nominal linewidth (microns)	Tone (all values in microns)		
	Clear	Opaque	All lines
1.0	0.073	–0.007	0.033
0.5	0.004	–0.043	–0.019
0.4	–0.040	–0.065	–0.053
0.3	–0.300	–0.097	—

Table 1. SEM Data GHOSTed and unGHOSTed Patterns (continued)

e. Plus or Minus Percent of Deviation from Nominal, GHOSTed

Nominal linewidth (microns)	Tone		
	Clear	Opaque	All lines
1.0	0.10	0.8	0.4
0.5	1.0	0.2	0.4
0.4	0.3	0.5	0.3
0.3	0	2.3	1.3

f. Plus or Minus Percent of Deviation from Nominal, unGHOSTed

Nominal linewidth (microns)	Tone		
	Clear	Opaque	All lines
1.0	7.3	0.7	3.3
0.5	0.8	8.6	3.8
0.4	10.0	16.3	13.3
0.3	100	32.3	—

g. Three Sigma Deviations, GHOSTed

Nominal linewidth (microns)	Tone (all values in microns)		
	Clear	Opaque	All lines
1.0	0.034	0.051	0.043
0.5	0.055	0.033	0.046
0.4	0.039	0.029	0.036
0.3	0.029	0.042	0.037

h. Three Sigma Deviations, unGHOSTed

Nominal linewidth (microns)	Tone (all values in microns)		
	Clear	Opaque	All lines
1.0	0.055	0.057	0.132
0.5	0.053	0.070	0.082
0.4	0.076	0.057	0.077
0.3	—	0.060	—

Table 2. EDGE Data, GHOSTed

a. Mean Linewidths, GHOSTed

Nominal linewidth (microns)	Tone (all values in microns)		
	Clear	Opaque	All lines
2.0	2.002	2.004	2.003
1.0	1.001	0.992	0.997
0.5	0.512	0.489	0.501
0.4	0.406	0.395	0.401
0.3	0.295	0.269	0.282

b. Average Deviations

Nominal linewidth (microns)	Tone (all values in microns)		
	Clear	Opaque	All lines
2.0	0.002	0.004	0.003
1.0	0.001	–0.008	–0.003
0.5	0.012	–0.011	0.001
0.4	0.006	–0.005	0.001
0.3	–0.005	–0.031	–0.018

c. Percent of Deviation from Nominal

Nominal linewidth (microns)	Tone		
	Clear	Opaque	All lines
2.0	0.44	0.53	0.48
0.5	3.57	2.66	3.10
0.4	1.52	1.77	1.65
0.3	1.75	6.17	4.25

d. Three Sigma Deviations

Nominal linewidth (microns)	Tone (all values in microns)		
	Clear	Opaque	All lines
2.0	0.030	0.038	0.034
0.5	0.033	0.043	0.056
0.4	0.021	0.027	0.025
0.3	0.012	0.032	0.043

Table 3. Line Edge Roughness Determined by EDGE

Mean 3 sigma values for all measurements on each line

Nominal linewidth (microns)	Tone (all values in microns)	
	Clear	Opaque
2.0	0.046	0.42
1.0	0.042	0.041
0.75	0.041	0.039
0.5	0.046	0.038
0.4	0.039	0.042
0.3	0.042	0.037

Table 4. Gold Plated Linewidths (in microns)

Nominal linewidth	Mean linewidth (3 sigma)		Mean linewidth (3 sigma)		Bias	
	Clear	Feature	Opaque	Feature	Clear	Opaque
0.3	0.256	0.078	0.507	0.072	0.05	0.20
0.5	0.419	0.083	0.713	0.074	0.081	0.213
1.0	0.853	0.069	1.226	0.076	0.147	0.226

ETEC

GHOST Proximity Correction (Owen and Rissman)

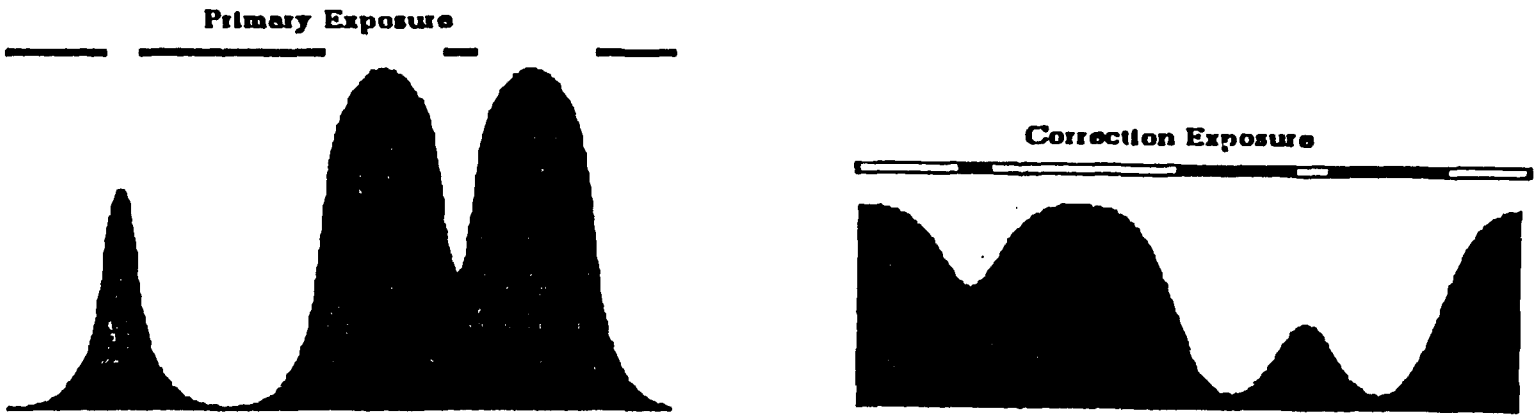

ETEC

X-Ray Masks — Materials

Simulated Masks

- Used 5x5-inch 90 mil quartz rather than BN film on an etched wafer to avoid breakage and pumpdown problems. The trilayer was identical to Du Pont's trilayer.

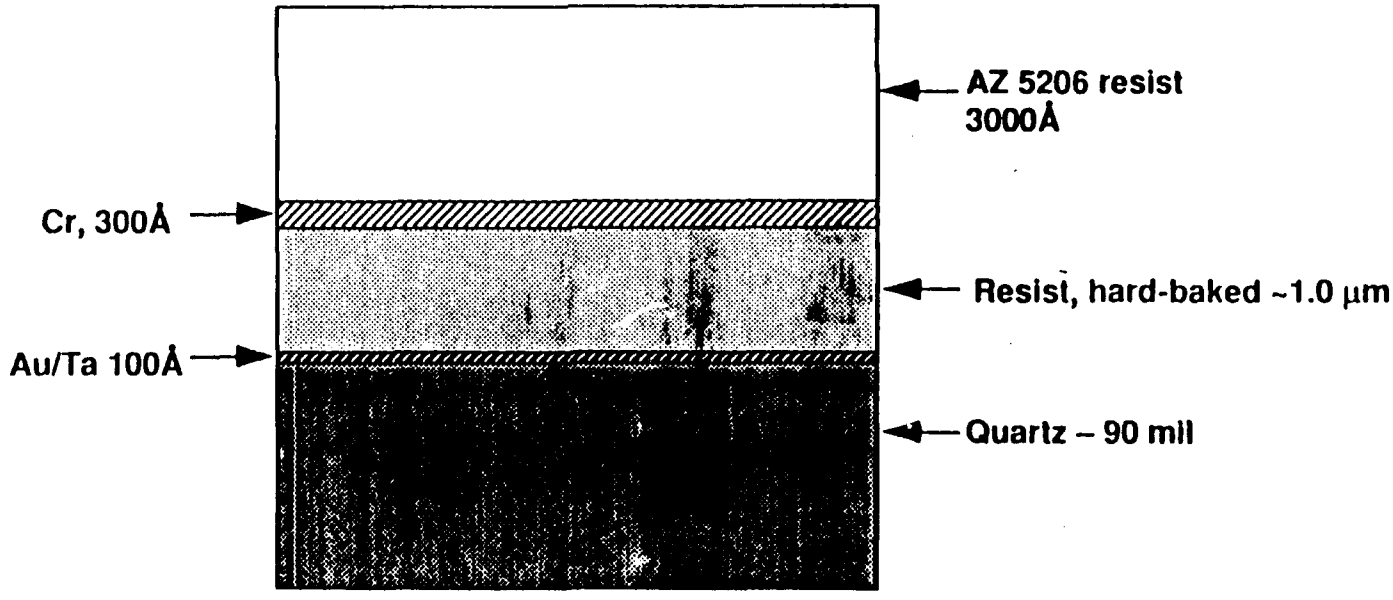

Figure 3
Proximity Grating

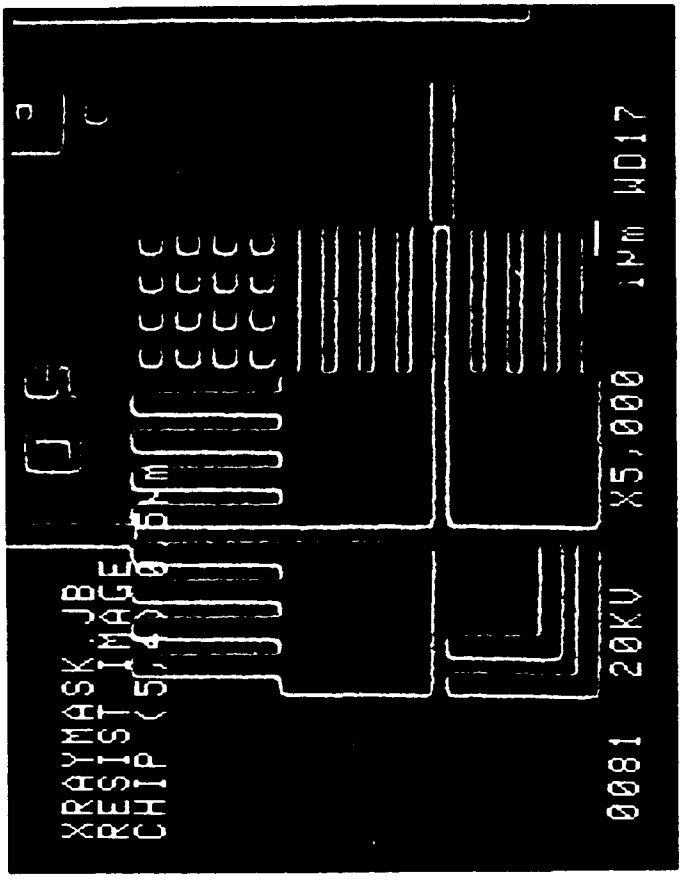

Figure 4
Proximity Dagger

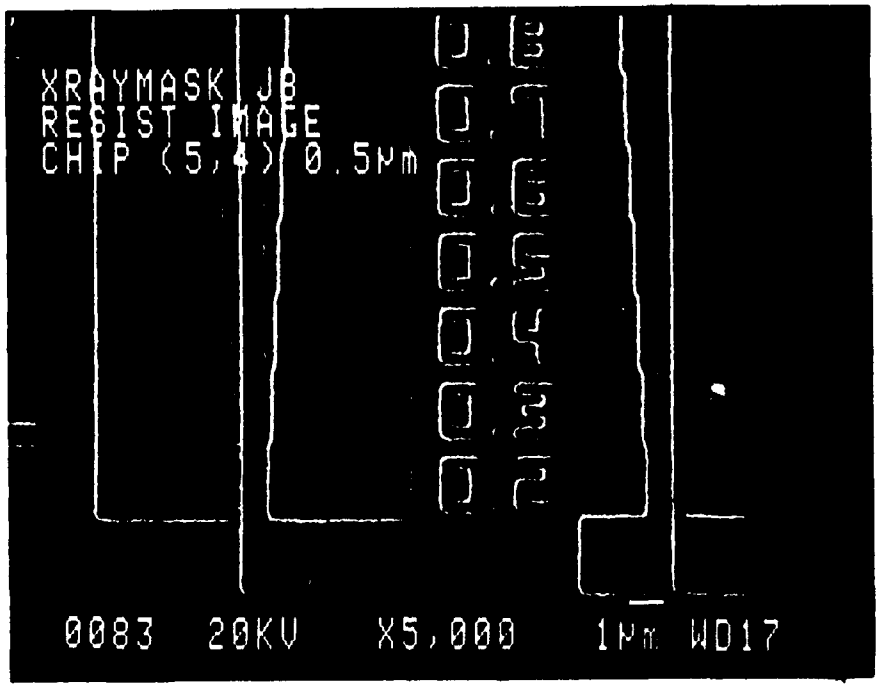

Figure 5
Crosses

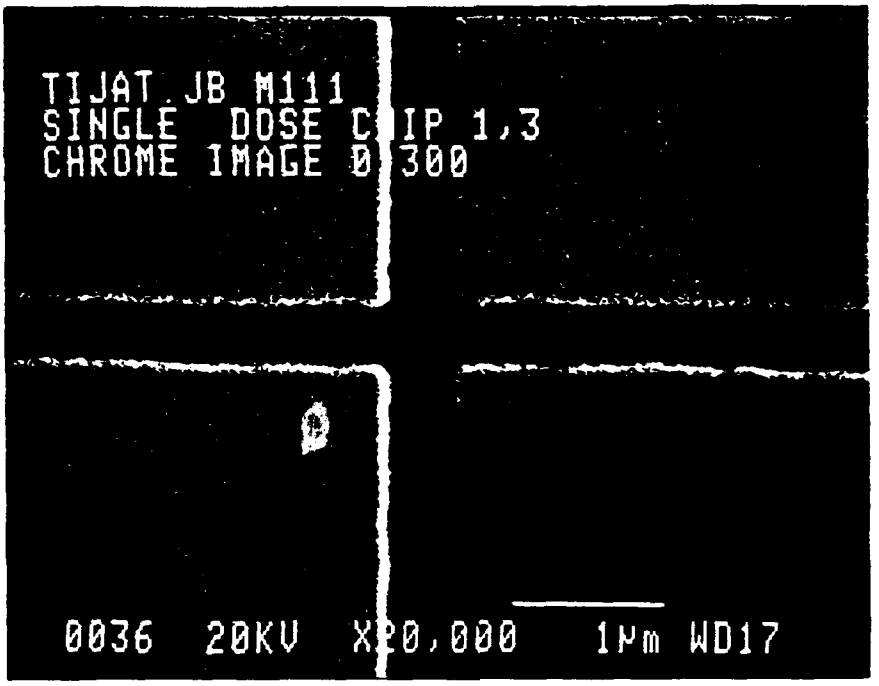

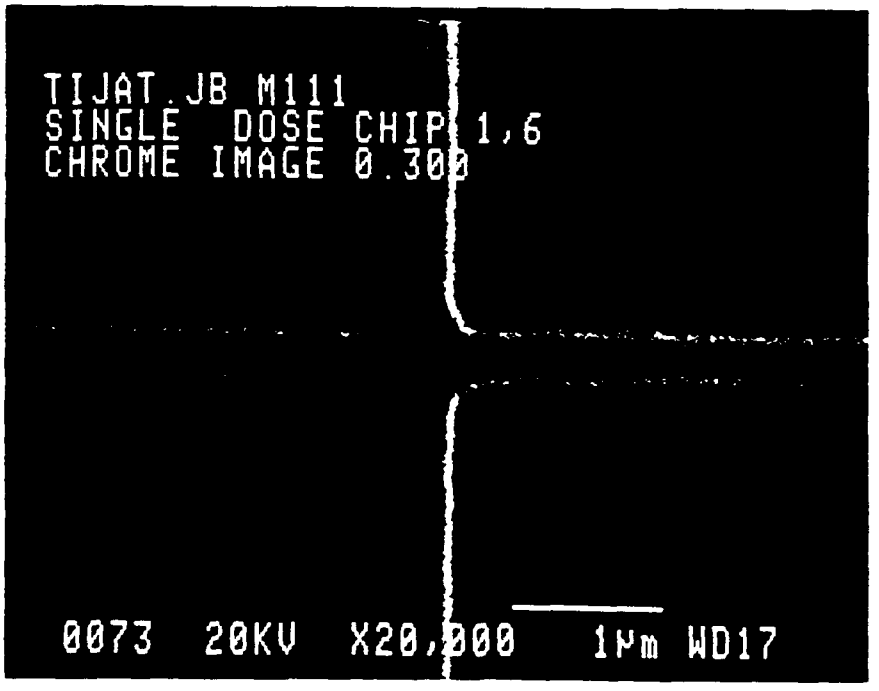

Figure 6

Diagram showing Proximity Effect Distortion for 0.3 micron Opaque line at the 0.2 micron Gap.

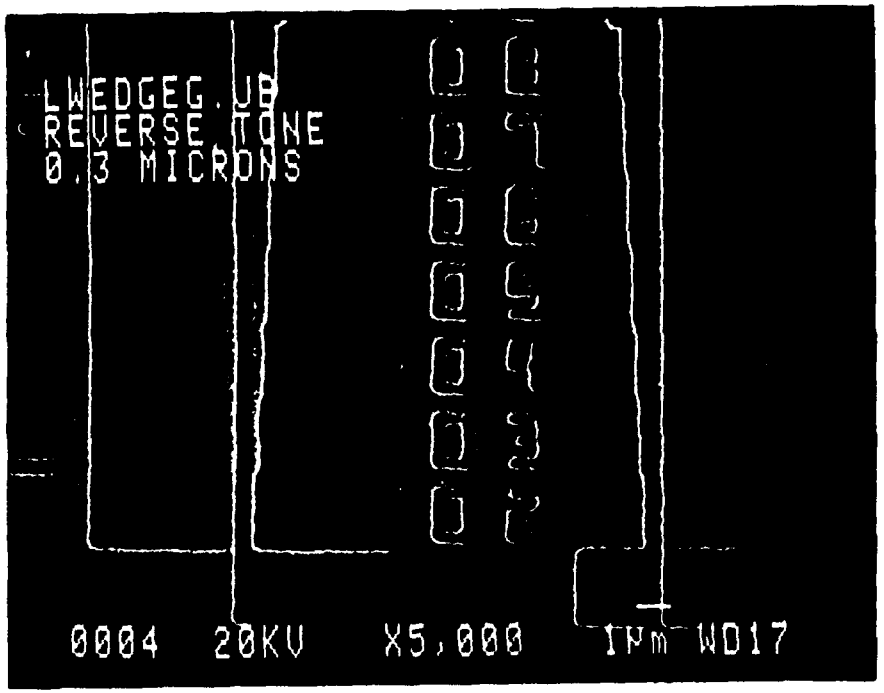

Figure 7

Resist image of Dagger on Trilayer. No Proximity Effect Distortion

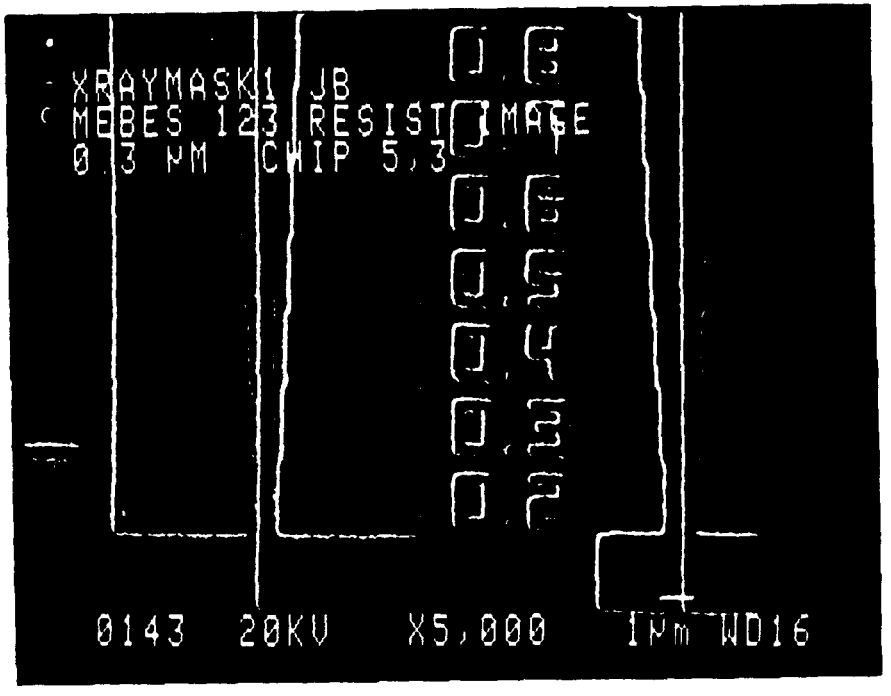

ETEC

Figure 8

Chrome on Glass
0.4 μm Pattern

No GHOST

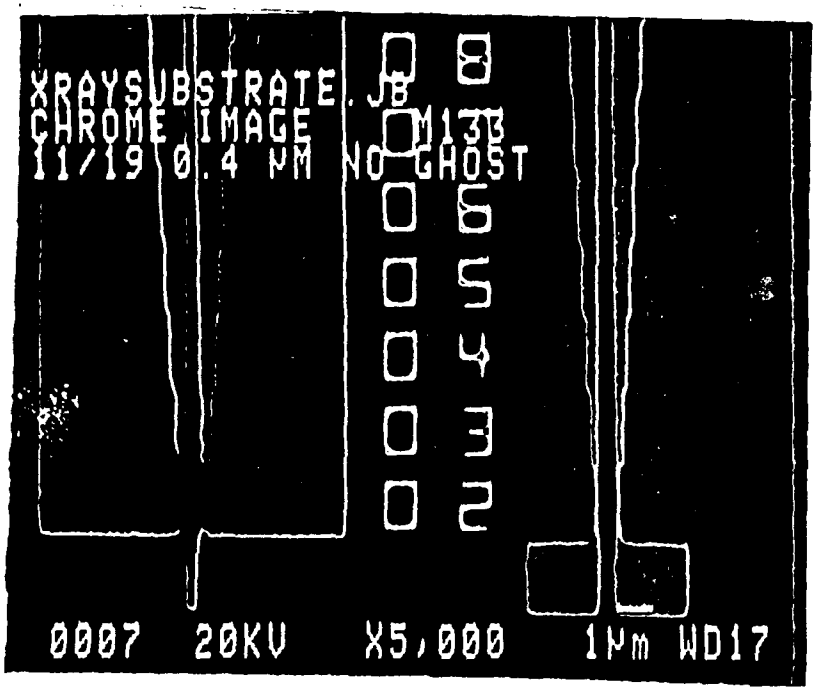

GHOST

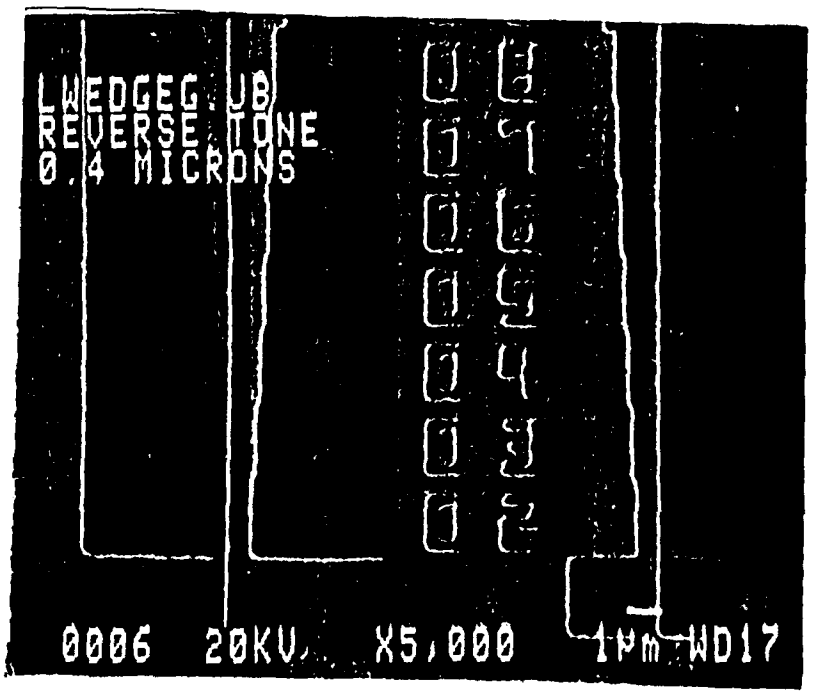

ETEC

Figure 9

Chrome on Glass
0.3 μm Pattern

No GHOST

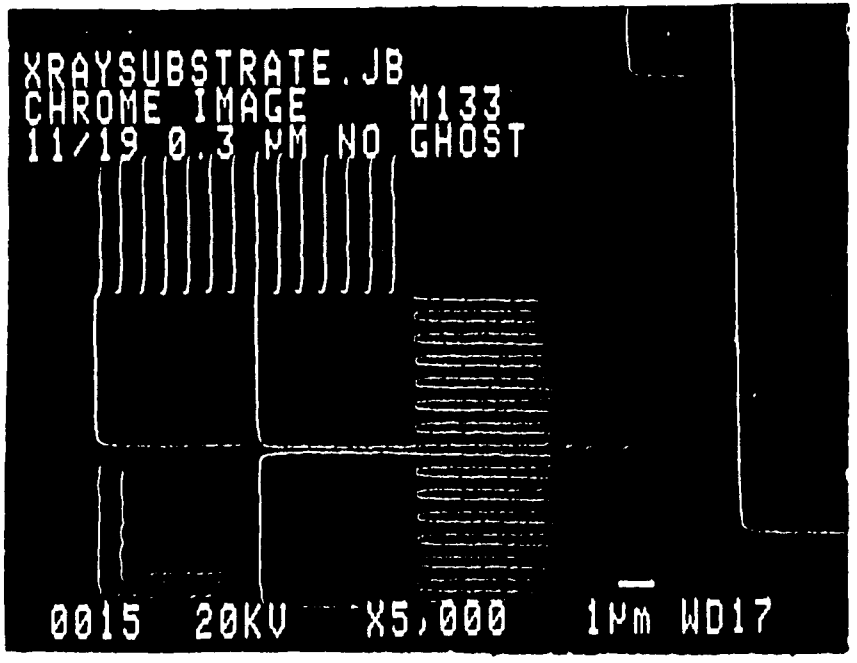

GHOST

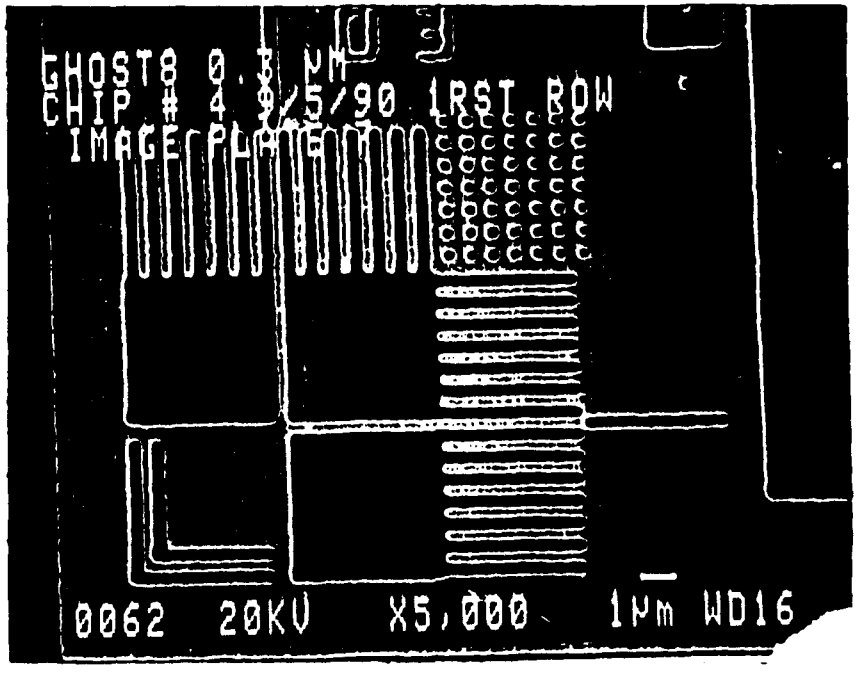

ETEC

Figure 10

Chrome on Glass
0.3 μm Pattern

No GHOST

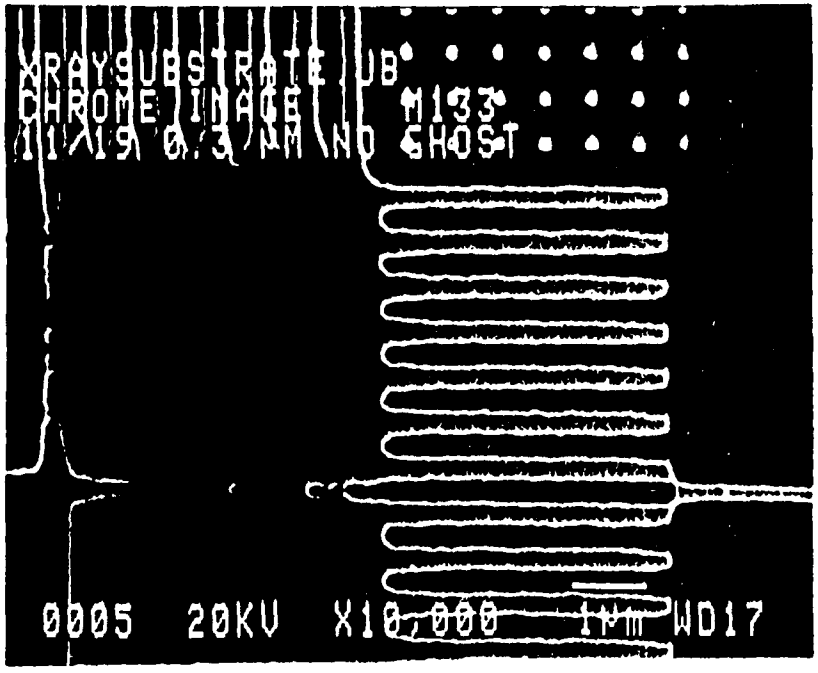

GHOST

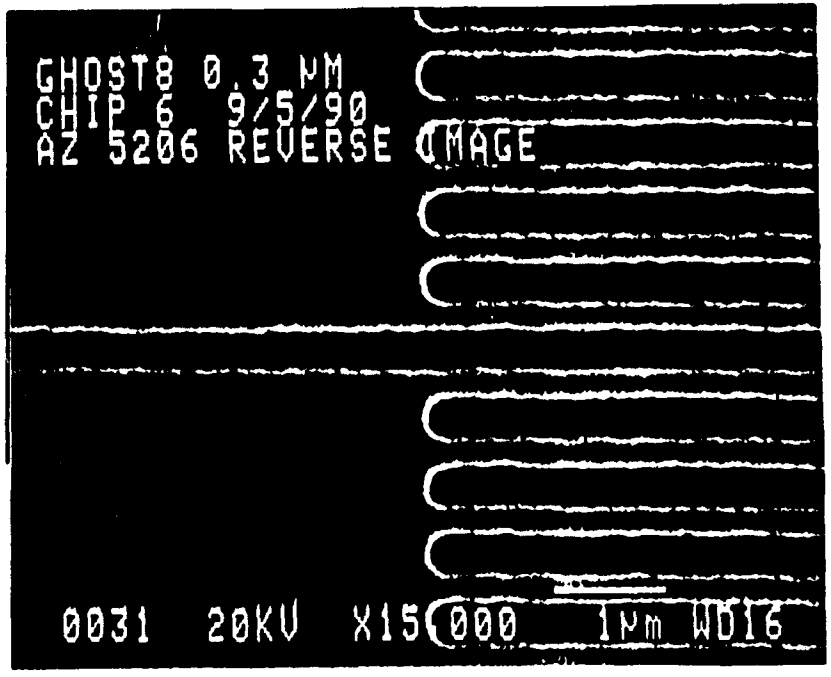

ETEC

Figure 11

Highest Magnification
0.3 μm Pattern

No GHOST

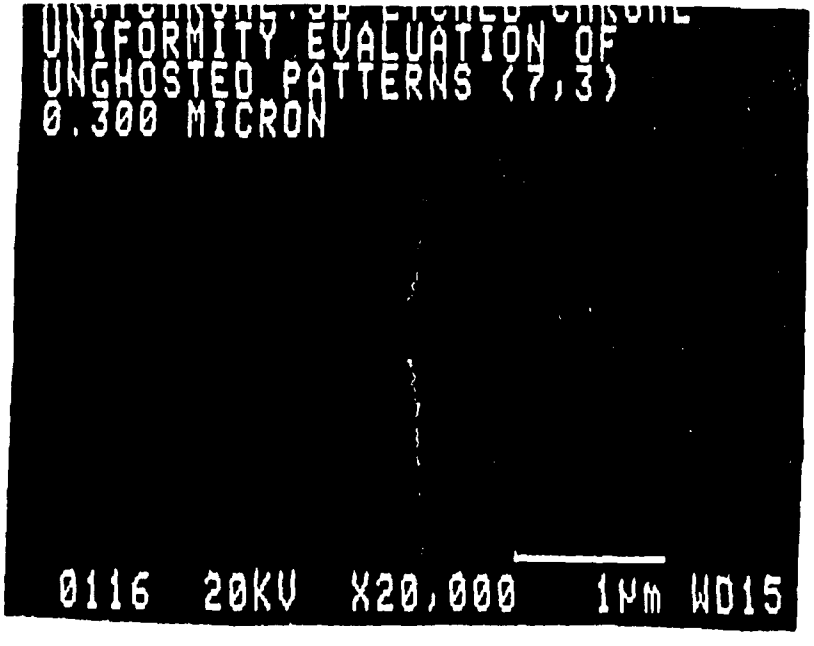

GHOST

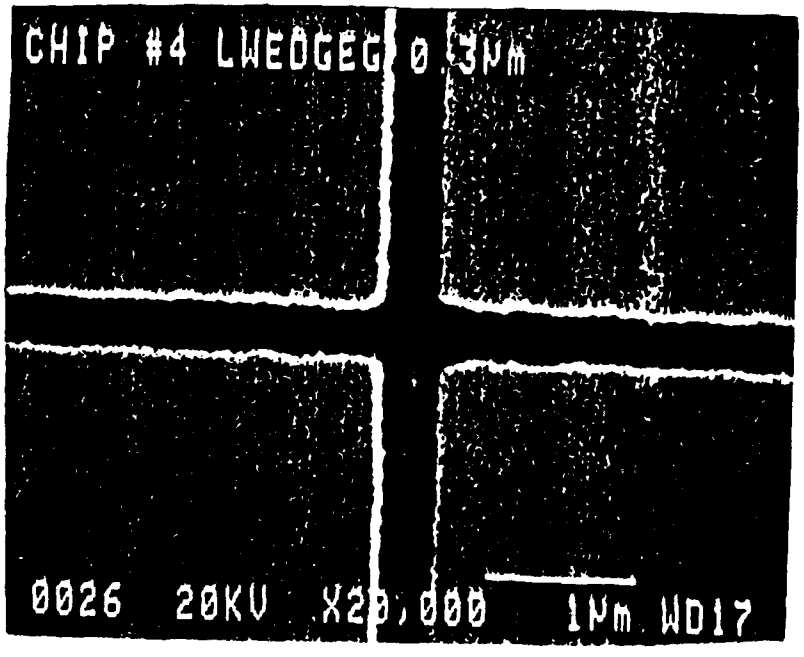

ETEC

Figure 12

Average Deviation from Nominal with 3 Sigma Error Bars for Clear Lines in X

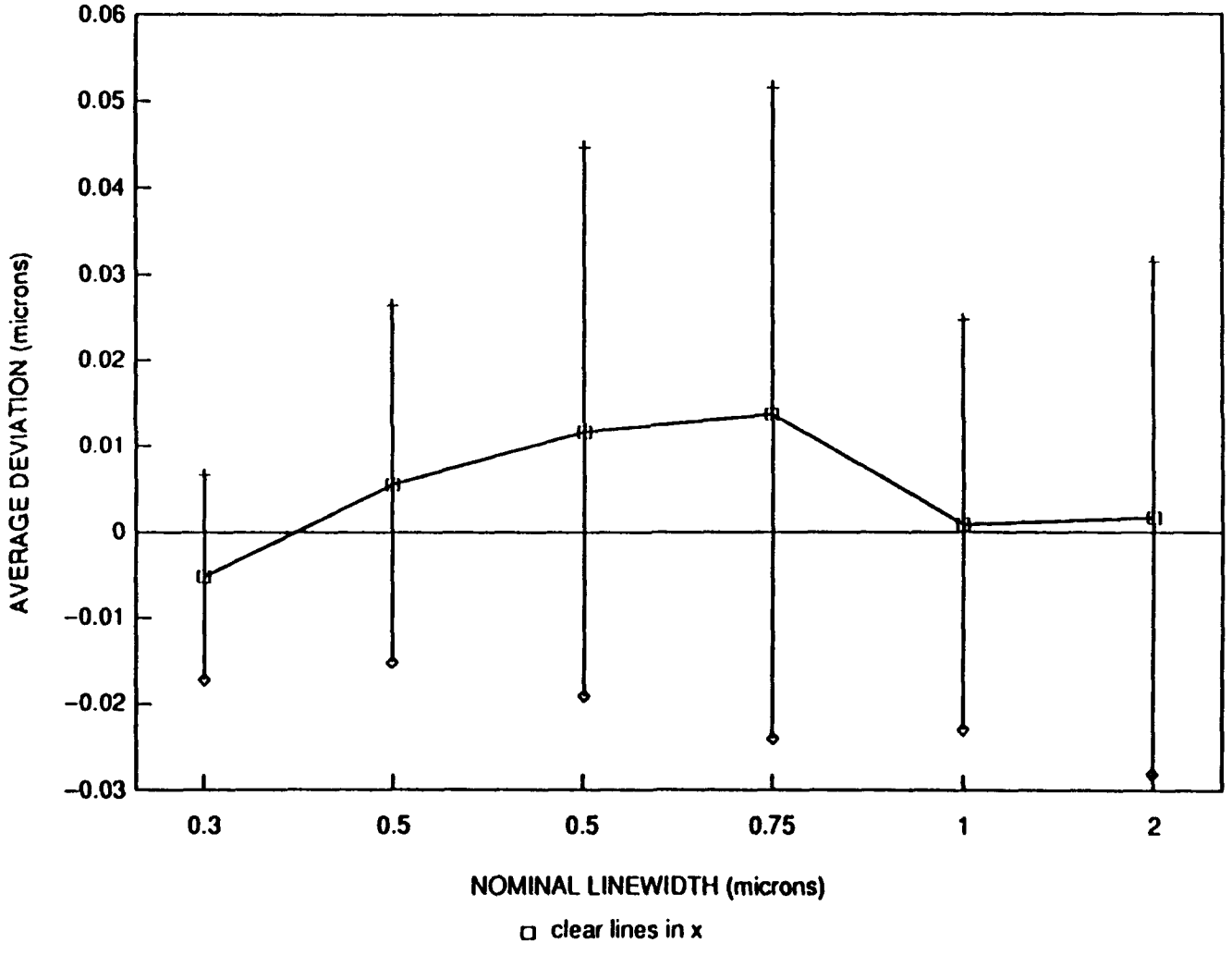

ETEC

Figure 13

Average Deviation from Nominal with 3 Sigma Error Bars for Opaque X Lines

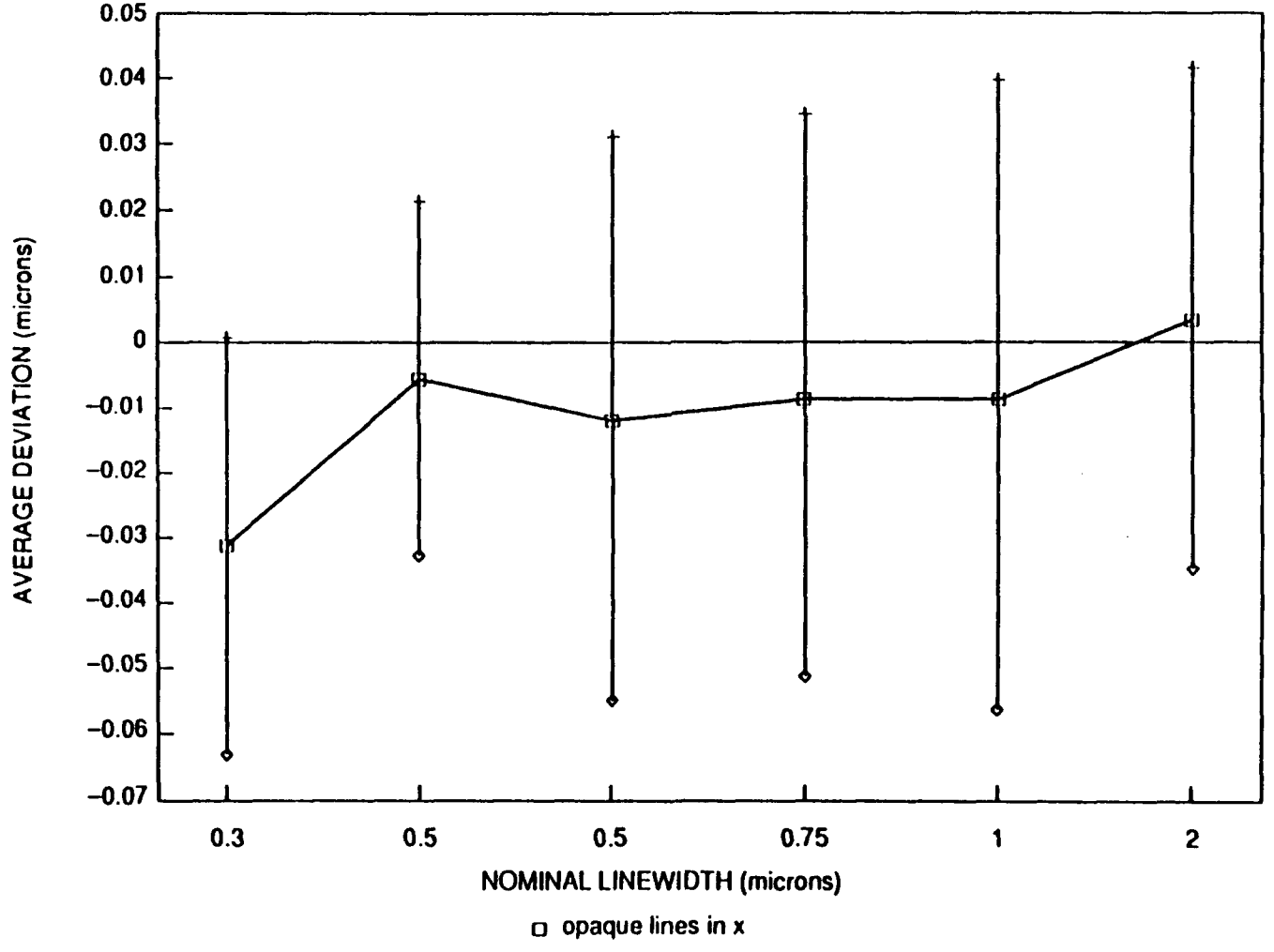

ETEC

Figure 14

Average Deviation from Nominal of GHOSTed (dashed) and unGHOSTed Patterns

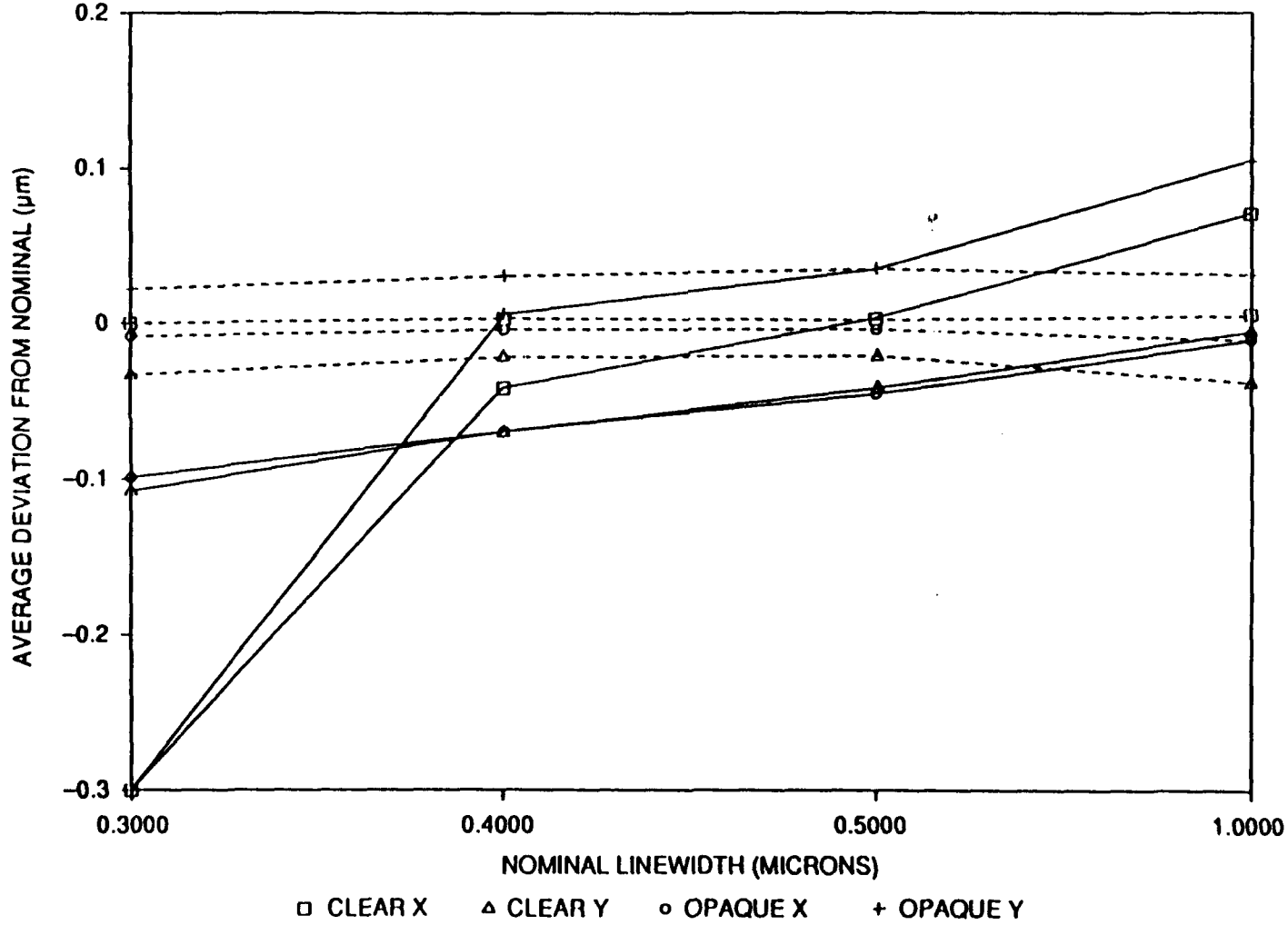

ETEC

Resist on X-Ray Stack 15

Opaque Y

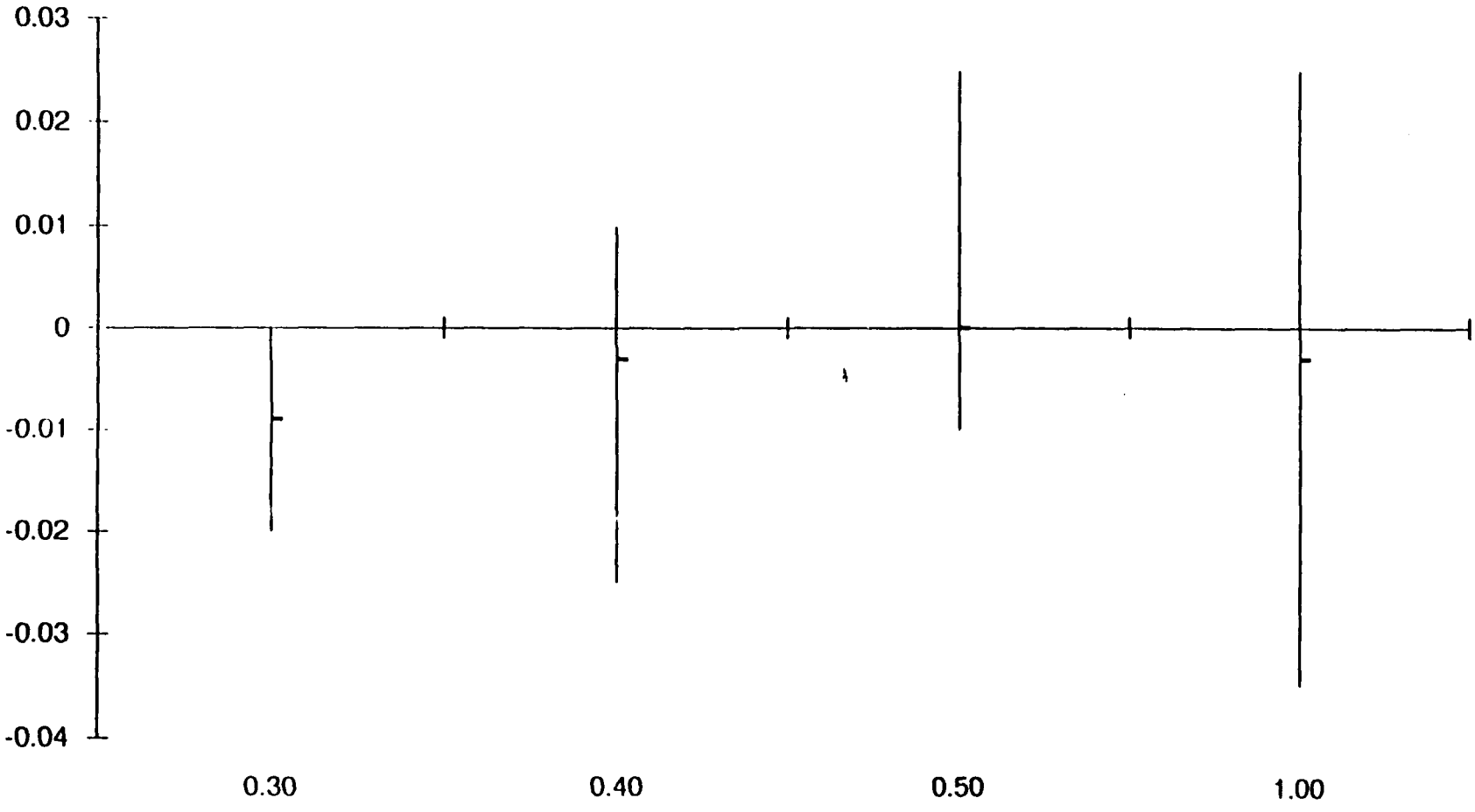

ETEC

Resist on X-Ray Stack 16

Opaque X

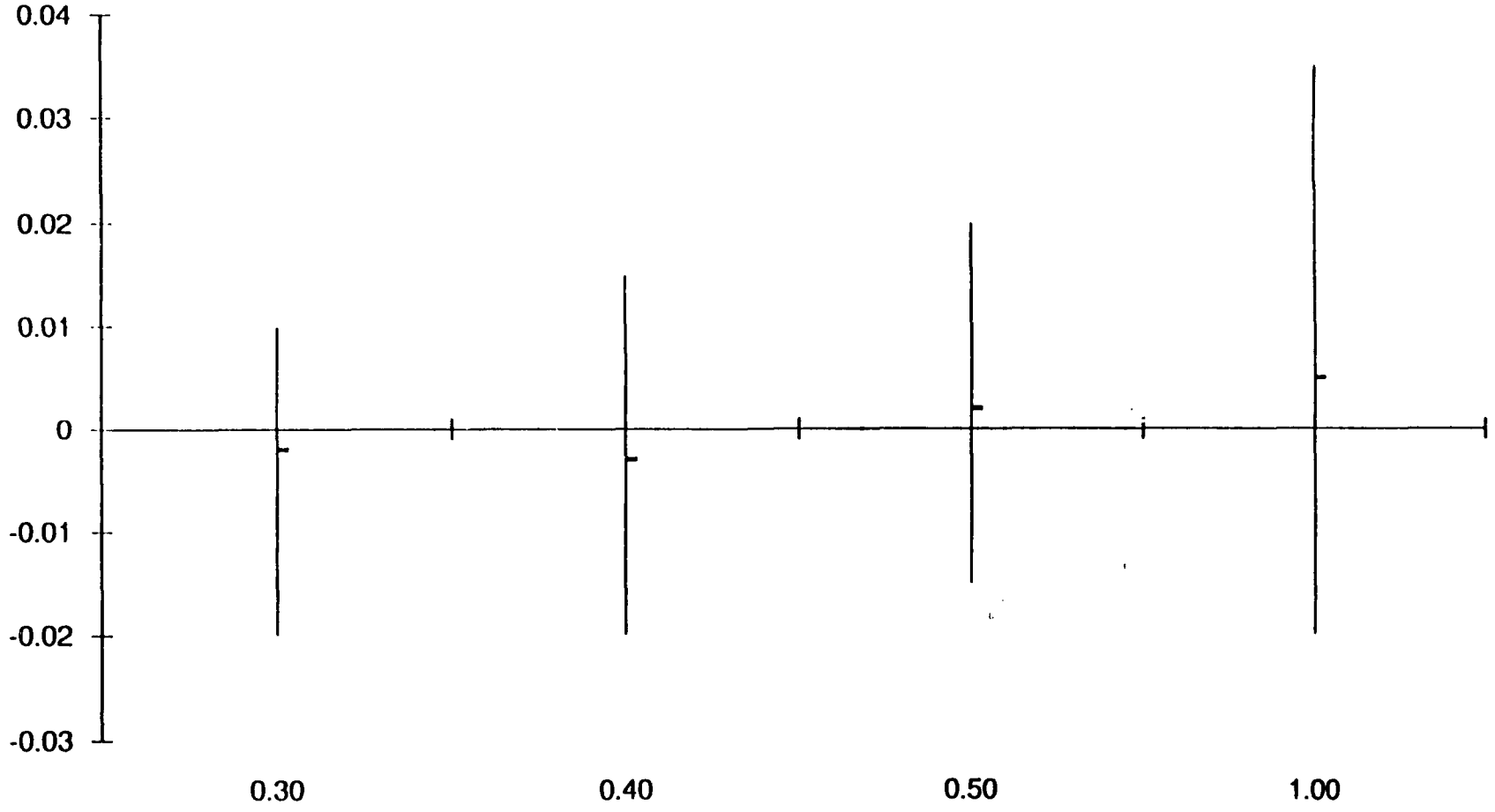

ETEC

Resist on X-Ray Stack

Clear Y

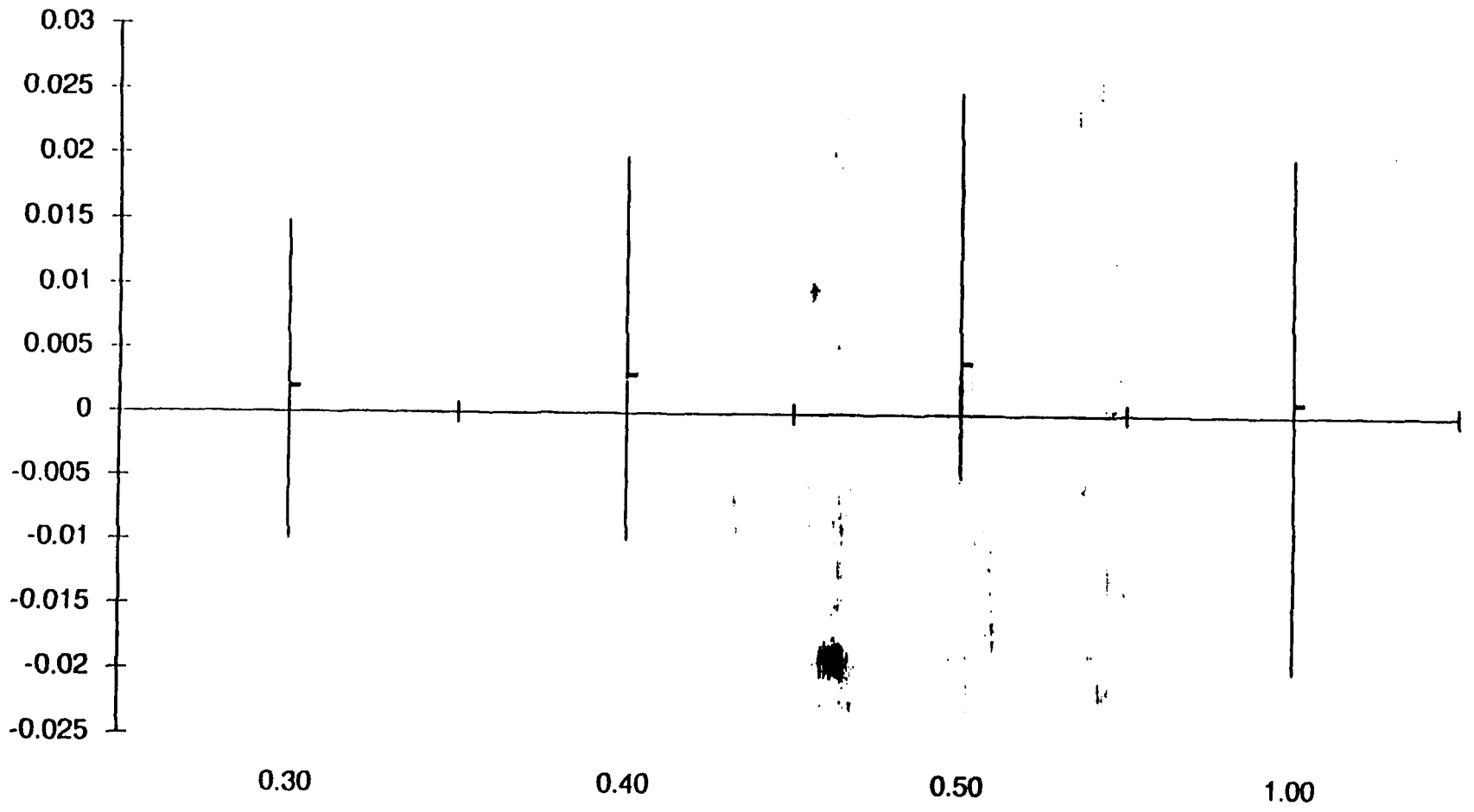

ETEC

Resist on X-Ray Stack 18

Clear X

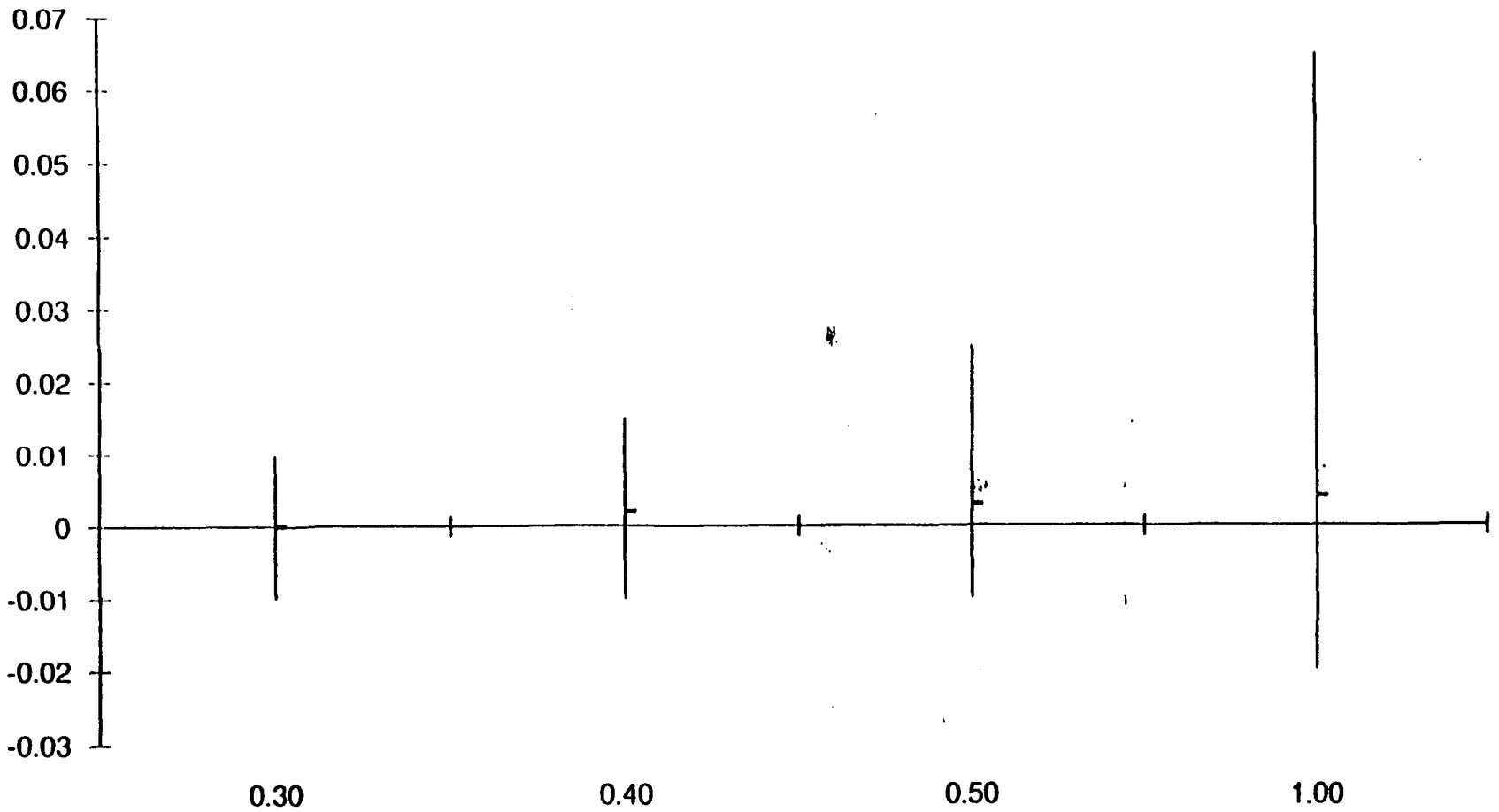

ETEC

Figure 19

Two-Dimensional Test Patterns: 0.2 Micron Design Rules

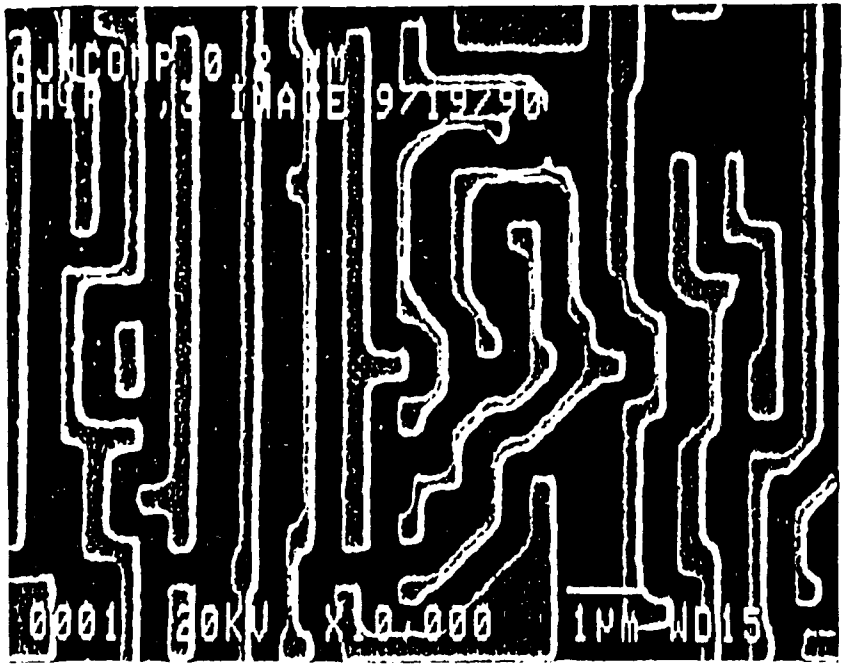

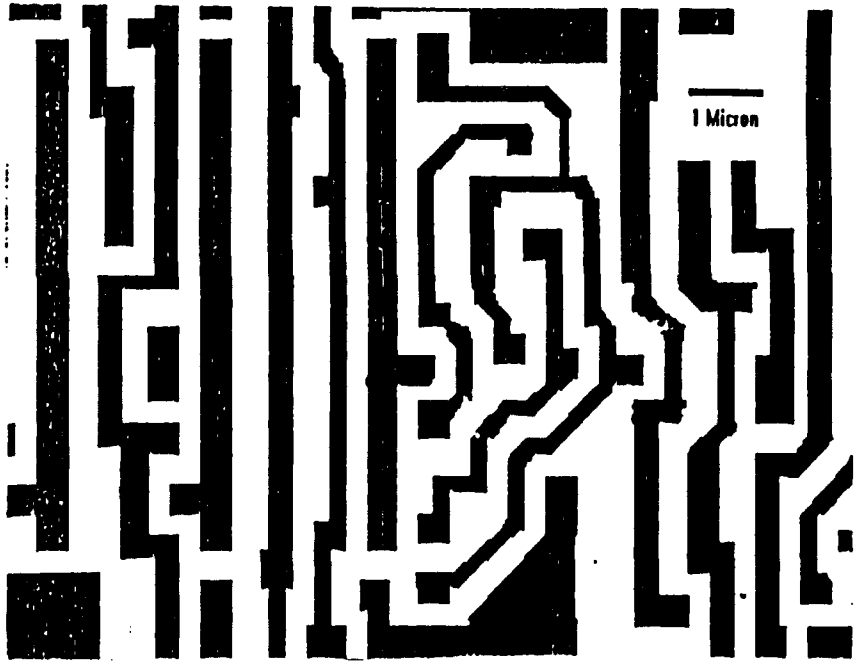

ETEC

Figure 20

Two-Dimensional Test Patterns: 0.2 Micron Design Rules

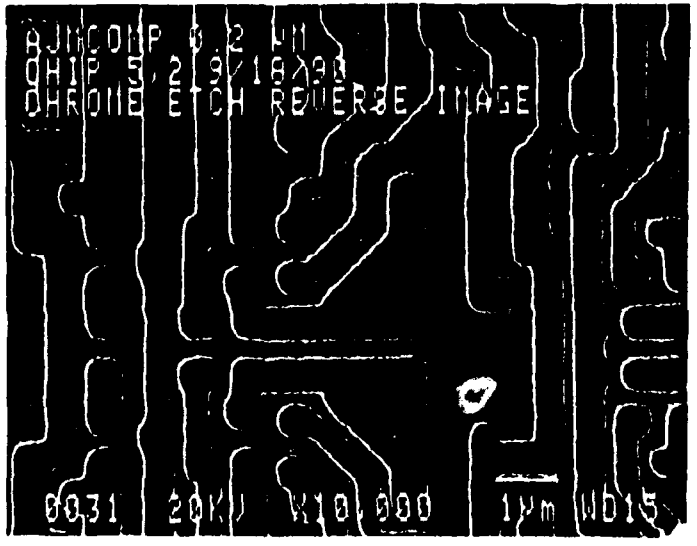

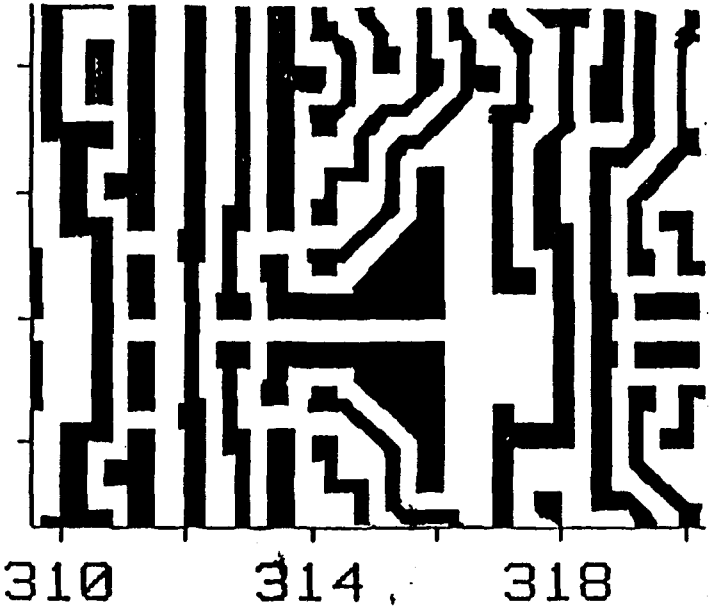

Figure 21 0.2 micron Dagger Patterns on Trilayer

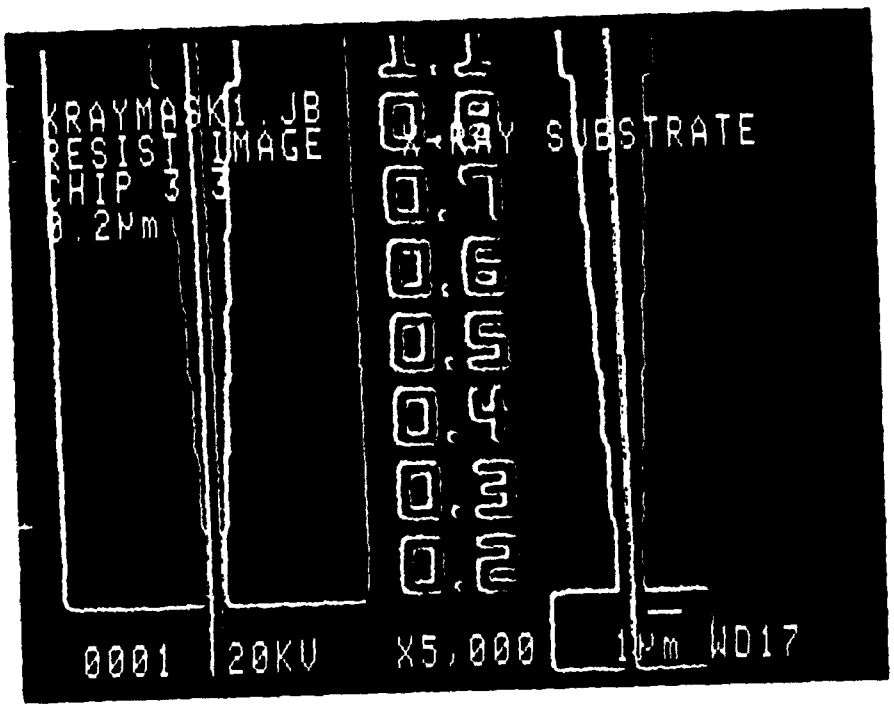

Figure 22.
Dagger Patterns written
on PBS Resist in Chrome.
Line Edge Roughness is very Good.

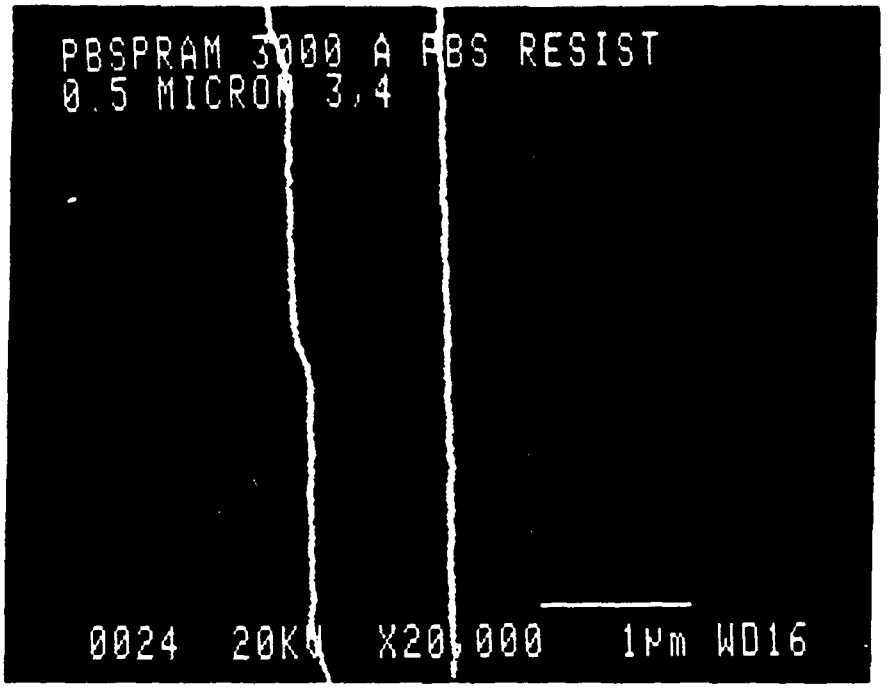

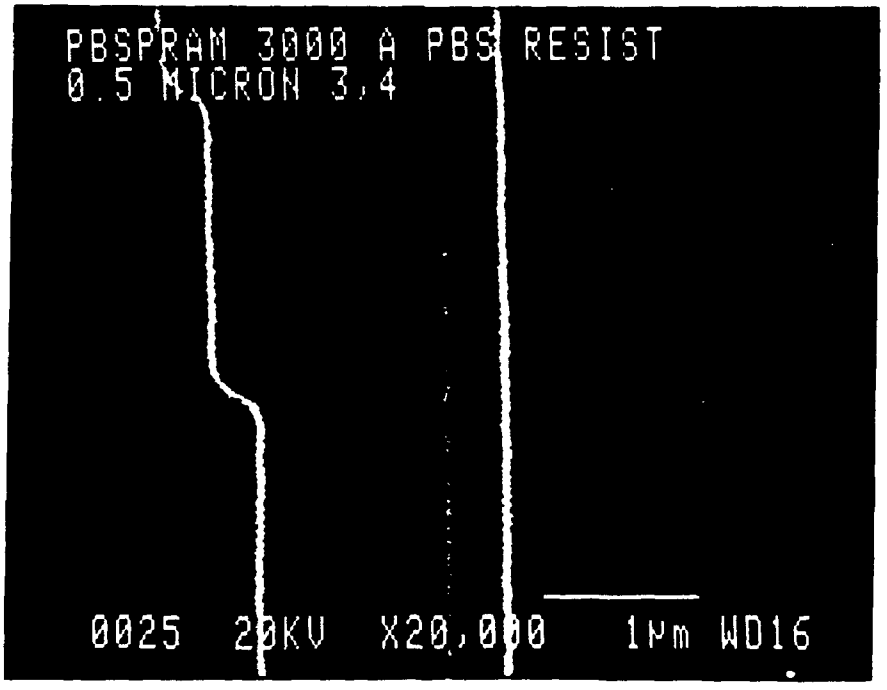

ETEC

Figure 23

Gold Plate

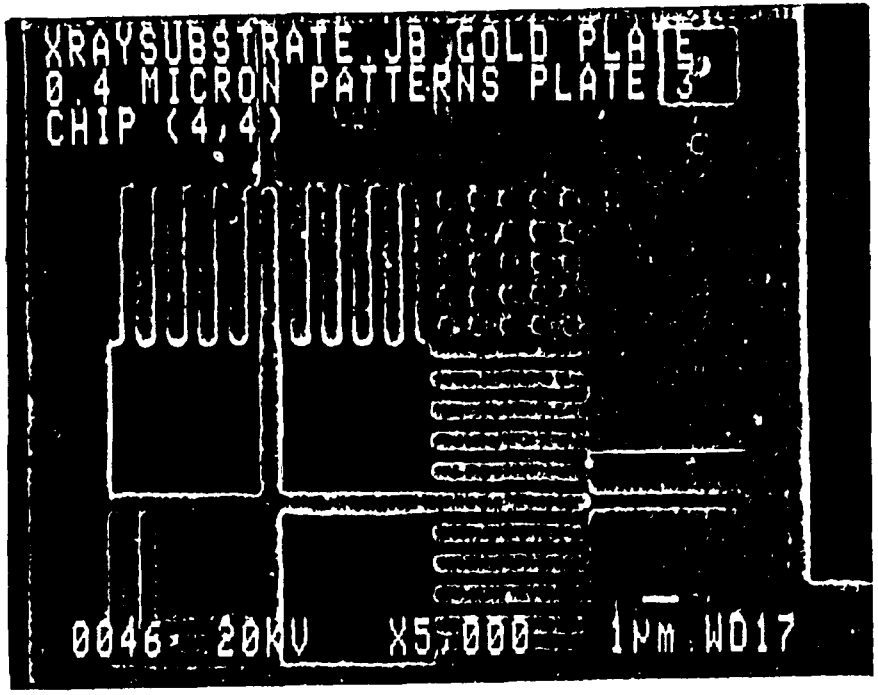

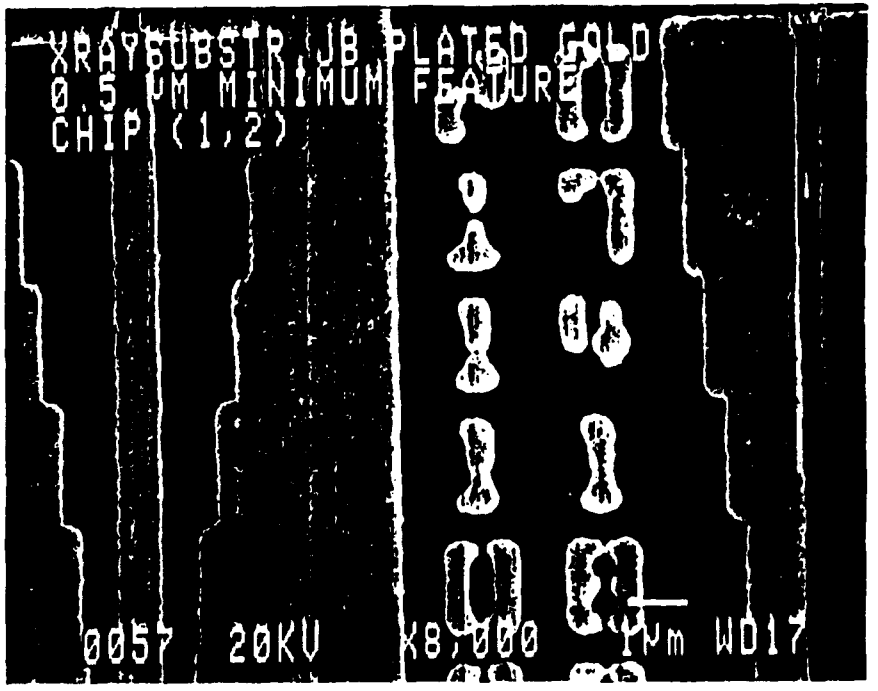

ETEC

Figure 24

0.3 μm Gold Plate
Logic Pattern

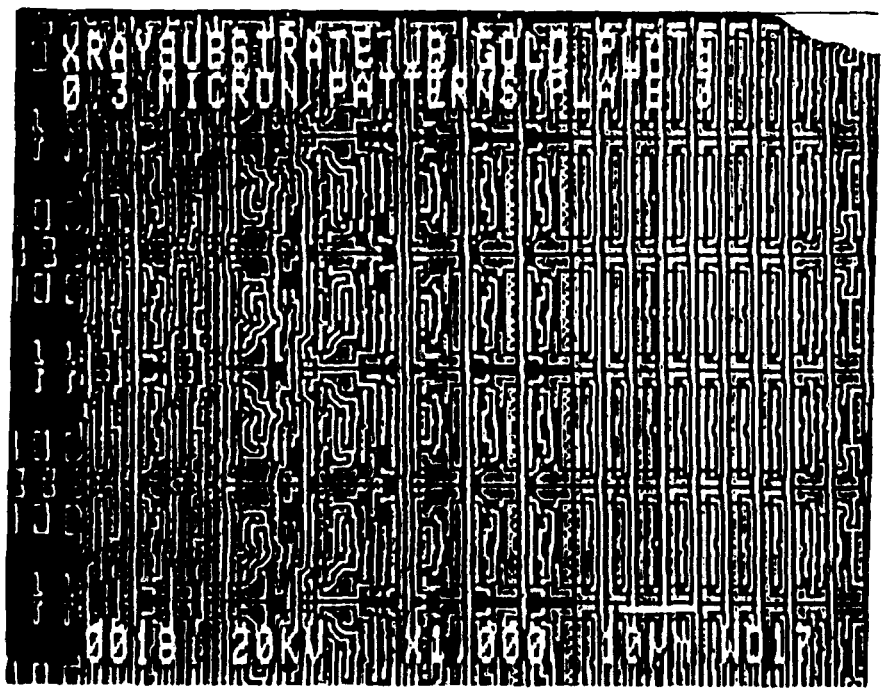

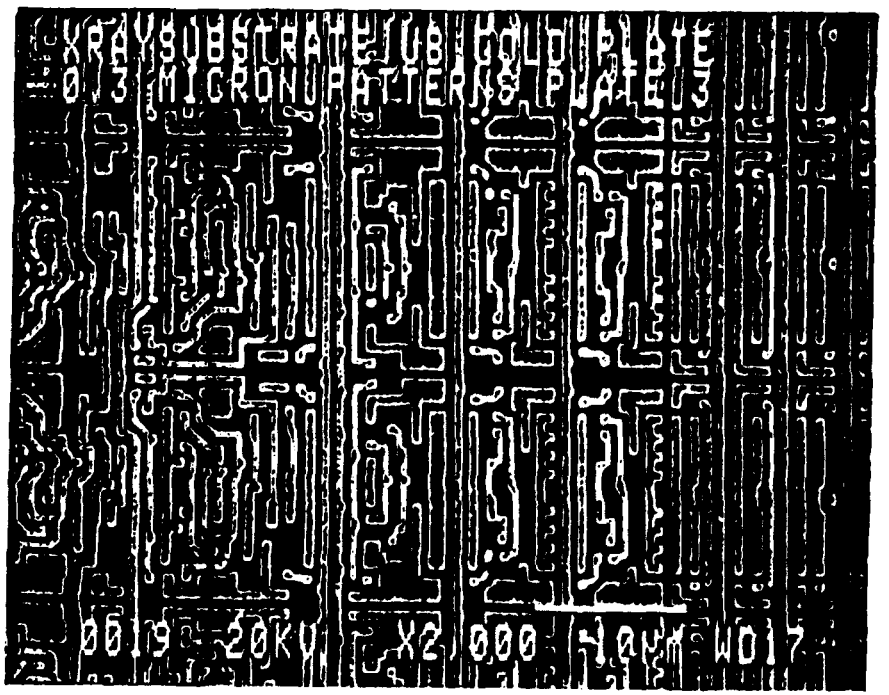

ETEC

Figure 25

0.3 μm Gold Plate
Logic Pattern

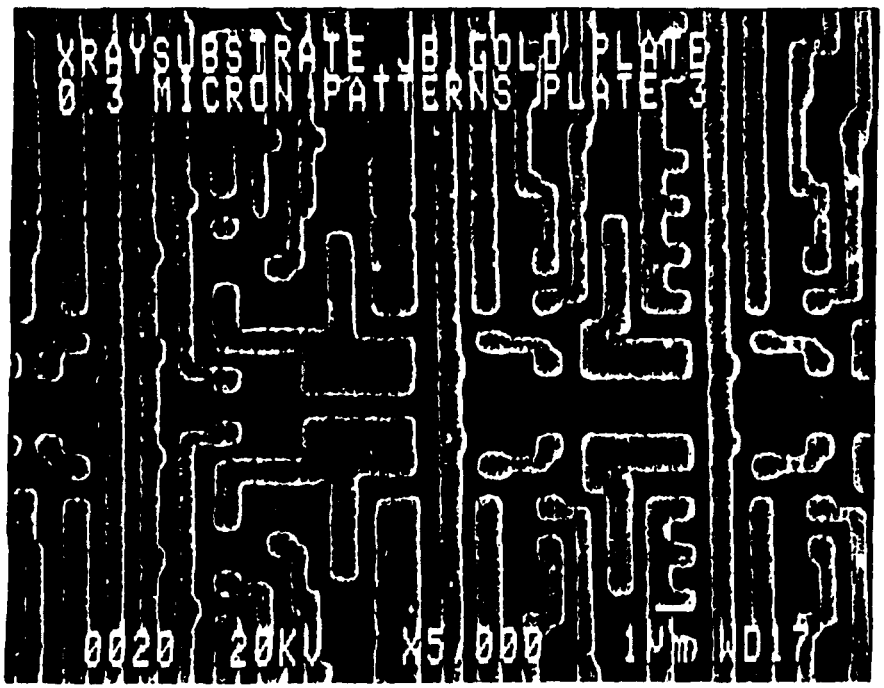

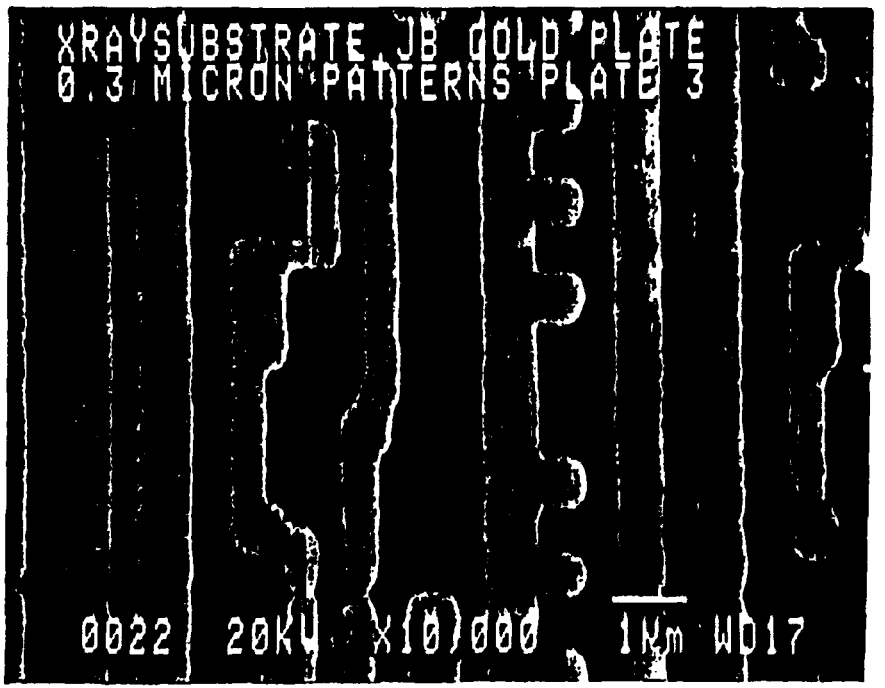

10. Appendix 2

The Low Voltage Alternative for Electron Beam Lithography
Y-H. Lee et al., Stanford University

An elastic cross section model for monte carlo simulations of low energy electornscatttering from high atomic number substrates
R. Browning et al., Stanford University.

Universal elastic scattering cross sections for electrons in the range 1-100keV
R. Browning, Stanford University

Silicon-on-quartz reflective masks for 0.25-μm microlithography
Y-H. Lee etal., STanford University

Low voltage alternative for electron beam lithography

Y.-H. Lee, R. Browning, N. Maluf, G. Owen, and R. F. W. Pease
Stanford Solid State Laboratory, Stanford University, Stanford, California 94305

(Received 24 June 1992; accepted 3 August 1992)

The current trend in electron beam lithography for patterning submicron features is towards the use of higher beam voltages (20–100 keV). Among the problems often perceived to be associated with the use of low voltages are the poorer resolution, the lower brightness, and the greater sensitivity to electric and magnetic interference. Both by simulation and by experiment at 2 kV it is shown: (1) features of less than 100 nm are clearly resolved in resist of about the same thickness; (2) such features are clearly resolved in both sparse and dense pattern; (3) such features in sparse and dense areas are clearly resolved over a twofold range of exposure doses; (4) such delineation is largely independent of substrate material; (5) there is no evidence of alternating-current magnetic interference; (6) the lower beam brightness at low voltages is compensated by the increased sensitivity of resists to lower energy electrons. The remaining concerns about low voltage lithography are the reliability of resist with an imaging layer less than 100 nm thick and the extent and effect of charging of such a resist.

I. INTRODUCTION

In 1960, Mollenstedt and Speidel[1] used electron beams for high-resolution patterning on membranes by modifying transmission electron microscopes. Practical electron beam lithography (EBL) started with a Westinghouse team (Wells, Everhart, and Matta)[2] in 1965, then with an IBM team (Broers, Lean, and Hatzakis).[3] Most tools were modified scanning electron microscopes (SEM) and primarily, for historical reasons, employed the same voltage (10–25 kV) as did SEM.[4–11] Proximity effects[12] caused by lateral scattering of electrons of energies above 10 keV in targets have been a subject of study for about 15 yr.

Two major schools of thought have emerged to deal with proximity effects: (1) applying complicated proximity effect correction schemes to current e-beam technology,[13–21] or (2) increasing the accelerating voltages to 50–100 kV,[22,23] so that the higher energy electrons forwardscatter less in the resist and the backscattered electrons emerging over a large area ($\sim 20\ \mu$m diam) are providing a relatively constant dose background. A third approach has been investigated, that is to use low voltage (<2 kV) such that the scattering is laterally confined to a small fraction of a minimum linewidth. In 1967, Pease[24] first reported that by using a retarding field, the chromatic and spherical aberration coefficients can be reduced at low landing energies and that there is no corresponding loss in current density. In 1986, McCord and Pease[25] used ultralow energy electrons (5–100 eV) in a scanning tunneling microscope (STM) to pattern thin electron beam resists. It is reported in this article that using a SEM operating at 2 kV (no retarding field) to pattern PMMA on both high and low atomic number substrates; the goal is to quantify the expected improvements in critical dimension control at low energy.

II. Prediction of electron scattering range by Monte Carlo simulation

A Monte Carlo simulation technique adopted to predict the electron scattering was based on a core program by Joy[26] modified to employ an elastic cross section for electron energy range from 1 to 100 keV.[27] The results clearly indicate the smaller interaction area (in targets) as the electron energy is lowered from 10 to 2 keV (Fig. 1). The program can also be used to show the distribution of energy dissipated per unit area throughout the thickness of thin resist film as a function of radius from the point of impact (Fig. 2). As might be expected this distribution is independent of substrate materials (Fig. 2).

III. EXPERIMENT

A. Exposure system

A Hitachi S800 SEM controlled with a PC-based pattern generator (Raith Elphy I) served as the exposure system. This SEM has a cold field emitter with two lenses, one condenser lens, and one objective lens. The exposure pattern (see Fig. 3) used for the study of proximity effects consists of areas of sparse and dense patterns. Because the SEM was operated in a conventional mode (no retarding

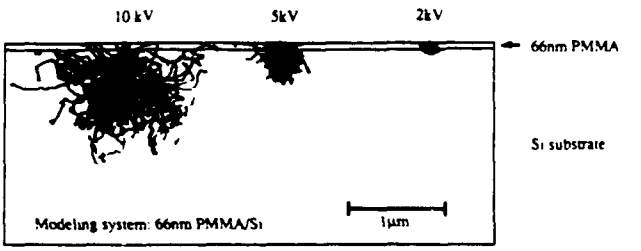

FIG. 1. Monte Carlo simulation illustrates that (1) the lower the electron energy the smaller the interaction area; (2) the smaller the lateral electron scattering range; (3) the thinner the surface imaging layer.

 0734-211X/92/063094-05$01.00

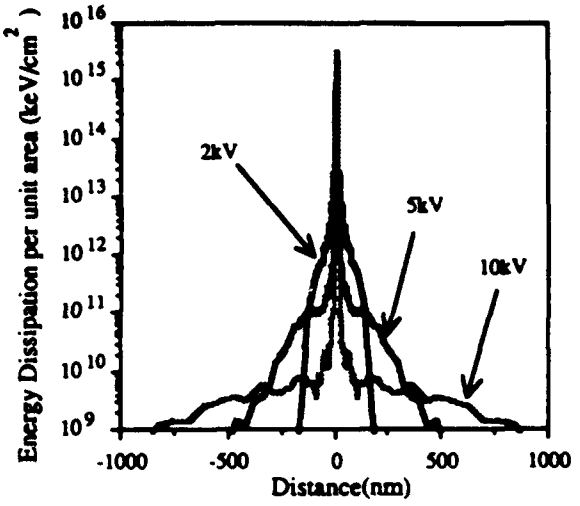

FIG. 2. Monte Carlo simulation of electron energy dissipated in 66 nm PMMA on Si at different accelerating voltages, 2, 5, and 10 kV. It suggests that the lower the energy of the electrons, the shorter the lateral electron scattering range. For 2 kV, the curve applies for both silicon and Au-coated silicon substrates.

field), small apertures ($\sim 100\ \mu$m in diameter) were used to reduce the aberration in the electron column. Alternating-current (ac) interference was reduced by using a short working distance (5 mm). The exposure doses were estimated from the beam currents, which were measured through correction of the *in situ* measured beam currents monitored via a picoammeter. The sample was grounded through the picoammeter. Because the *in situ* measured beam currents were lower than the total beam currents due to the backscattered electrons, a Faraday cup was mounted on the sample stage to measure the total electron beam current so that the backscattered electron coefficients can be estimated and the *in situ* beam currents corrected. The electron beam diameter (43 nm) was measured by the secondary electron signal from the Si knife edge (obtained by orientation dependent etching) and defined as the distance between the 10%–90% points. The address size was controlled to be 43 nm.

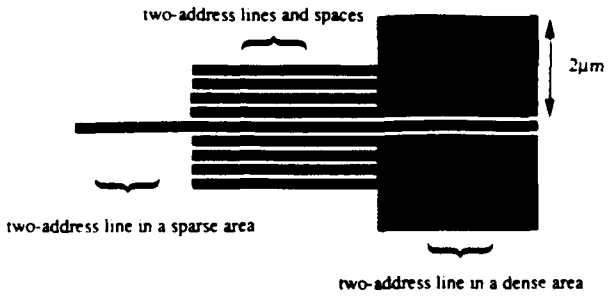

FIG. 3. Proximity effect pattern consists of two-address lines in dense and sparse areas. The dark areas are the exposed areas. The white areas are the unexposed areas.

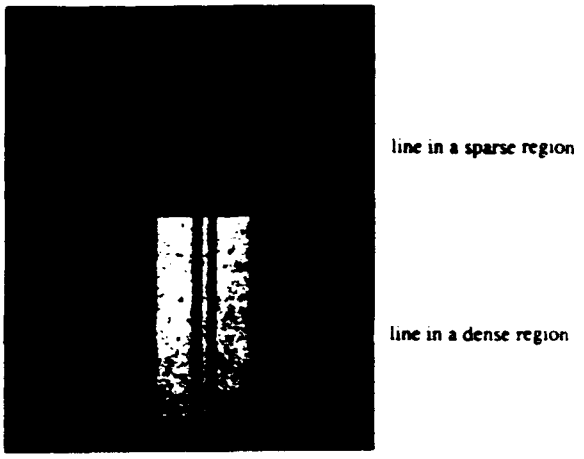

FIG. 4. SEM of developed resist image of 86 nm lines in dense and sparse areas on a silicon wafer. The negligible linewidth difference in dense and sparse areas demonstrated very low proximity effect for 2 keV electrons. The white area is the exposed area. The dark area is the unexposed area.

B. Resists, substrates, and processing

Two types of substrates were used, namely, bare silicon and silicon overcoated with 300 nm thermally evaporated gold. PMMA, 66 nm thick, was spin-casted on the substrates and prebaked at 120 °C for 6 h. The exposure dose range was 10–30 μC/cm^2. After exposure, samples were developed in 1:2 methyl isobutyl ketone (MIBK):isopropyl alcohol(IPA) for 35 s. Postbaking was performed at 120 °C for 20 min. The linewidths were estimated by viewing the SEM at 100 000× (at 25 kV), although the buildup of contamination in the SEM made accurate measurements difficult.

IV. RESULTS AND DISCUSSION

A. Low proximity effect

Representative SEM of developed resist images of line and space patterns on a silicon substrate are shown in Fig. 4. Note that the linewidth difference in the dense and sparse areas is less than 10 nm. This experimental result shows that proximity effect is very low for 2 keV electrons.

B. High dose tolerance and independence of substrate materials

Representative micrographs of the developed resist patterns on both types of substrates are shown in Figs. 5 and 6. Note that the difference of linewidth of two-address lines for both dense and sparse patterns on both types of substrate is negligible. This demonstrates the virtual elimination of proximity effect on both high and low atomic number substrates. The allowed dose ranges for resolution of 86 nm features in dense and sparse areas are 16–28 μC/cm^2 for bare silicon and 14–27 μC/cm^2 for gold-coated substrate, respectively. The granular structure of gold made precise linewidth measurements difficult.

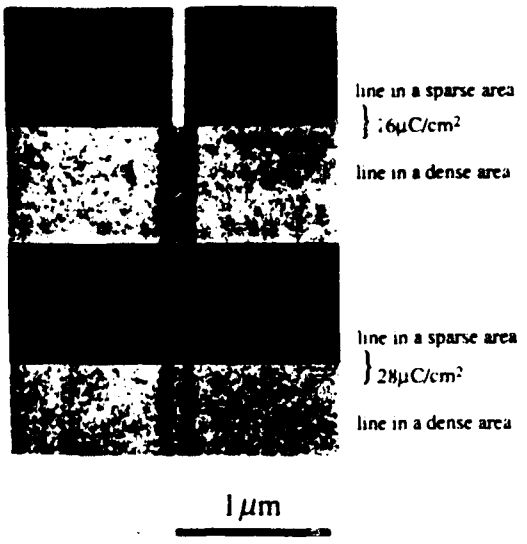

FIG. 5. SEM of developed resist image of nominal 86 lines in dense and sparse areas by a 2 keV electron beam on 66 nm PMMA/Si at the exposure doses of 16 and 28 $\mu C/cm^2$. Note the nominal 86 nm lines can be resolved in dense and sparse areas over 70% dose variation.

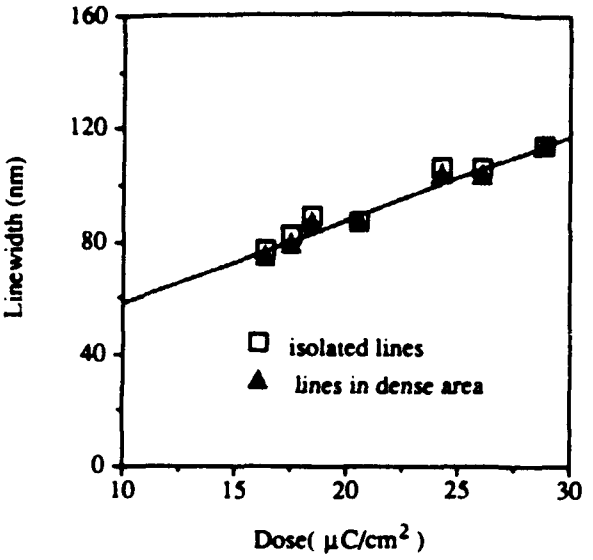

FIG. 7. Linewidth measurement as a function of exposure dose for the nominal 86 nm features on 66 nm PMMA/Si exposed by 2 keV electrons. Note the absence of any effect of the density on the pattern and the low sensitivity of linewidth to dose ($\Delta = 40$ nm for a twofold increase in dose).

C. Dose effect on linewidth

Measured linewidths have been plotted for both sparse and dense patterns as a function of exposure for both types of substrate in Figs. 7 and 8. The measured linewidth difference at a 10% exposure dose variation is 6 nm on bare silicon and 9 nm on gold-coated substrates.

For linewidth modeling, the following were basic assumptions.

(1) The incident current density distribution is

$$j = j_0 \exp(-r^2/\sigma_e^2) . \quad (1)$$

where r is the radial coordinate, measured from the center of the spot, and σ_e is the radius at which the current density falls to $1/e$ of its peak value. The beam diameter d is related to σ_e by the relation ($d = 1.66\sigma_e$), thus σ_e is 25.9 nm.

(2) For a point spot, the distribution of the energy deposited in the resist by the low-energy electrons was computed with the Monte Carlo program. Therefore, for a spot with radius σ_e, the energy density distribution in the resist

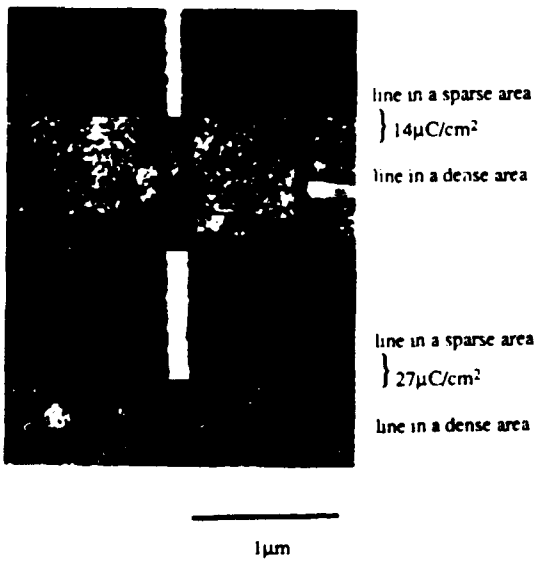

FIG. 6. SEM of developed resist image of nominal 86 nm lines in both dense and sparse areas by a 2 keV electron beam on 66 nm PMMA/300 nm Au/Si at the exposure doses of 14 and 27 $\mu C/cm^2$. Note that the high dose tolerance applied to Au-coated substrate as to bare silicon for 2 keV electrons (see Fig. 5). The rough surface is due to the granular structure of gold.

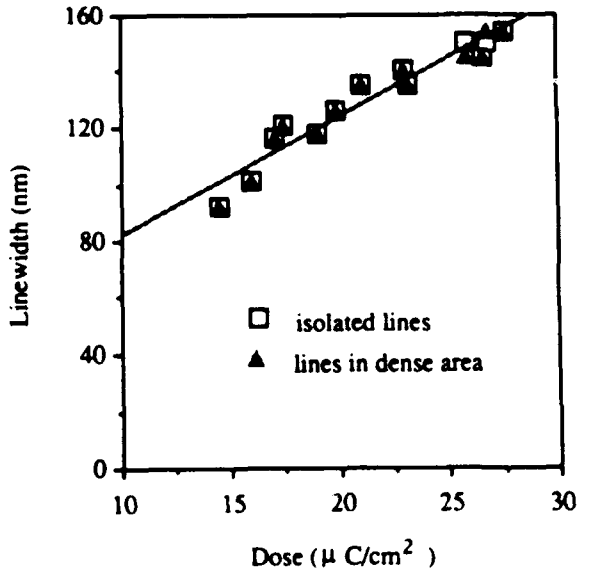

FIG. 8. Linewidth measurement as a function of exposure dose of nominal 86 nm features on 66 nm PMMA/300 nm Au/Si exposed by 2 keV electrons.

TABLE I. Comparison of measured and modeled linewidth difference at 10% dose variation for two-address lines in dense and sparse area on both Si and 300 nm thick gold coated Si substrates. $\Delta L10\%$: *linewidth difference for a 10% exposure variation.*

	Lines in sparse areas		Lines in dense areas	
	$\Delta L10\%$ measured (nm)	$\Delta L10\%$ calculated (nm)	$\Delta L10\%$ measured (nm)	$\Delta L10\%$ calculated (nm)
Si	6	8	6	8
Au	9	10	9	10

is a convolution of the incident current density distribution and the distribution of the energy deposited in the resist for a point spot.

Linewidth variation was modeled for a 10% change in exposure dose for two-address lines in dense and sparse areas for both types of substrate. As shown in Table I, the measured linewidth differences match with the modeled very well.

D. Application of low voltage EBL

It was a concern that low voltage electrons may not be able to expose resists which are sufficiently thick for useful pattern transfer. To investigate this potential problem, low-voltage (2 kV) EBL were employed for making both optical and x-ray masks. The patterned materials were 100 nm thick amorphous-Si (α-Si) [for deep ultraviolet (DUV) optical masks] and 200 nm tungsten (for x-ray masks). The resist was 66 nm thick PMMA for silicon and 90 nm for the tungsten. The developed PMMA resist layers served as a very effective plasma etch mask for α-Si and marginally effective for tungsten. The etching selectivities were measured by measuring the etching rates using ellipsometry and step profiling. For silicon etching, we used a combination of SF_6 and C_2ClF_5 gases in a Drytek plasma etcher (both gases at 200 sccm; 150 mTorr, 500 W). The etching condition gives an etching selectivity of 1:5 for PMMA on Si. For W etching, an etching selectivity of 1:2 of PMMA on W with a combination of SF_6 and CF_3Br in the same etcher as for silicon etching (both gases at 50 sccm; 65 mTorr, 500 W) was obtained. Figures 9(a) and 9(b) show the dry-etched silicon and tungsten delineated by the conditions described above. For etching chromium, Kuan[28] has reported the use of PMMA as thin as 8 nm.

V. SUMMARY

Low voltage (2 kV) EBL on both high and low atomic number substrates showed negligible proximity effects for features down to 86 nm as previously predicted by Monte Carlo simulation. High resist sensitivity and a remarkable high dose tolerance were also demonstrated. It was also demonstrated that thin surface imaging layers are adequate for pattern transfer for both optical and x-ray mask materials. Spurious beam wobble due to ac magnetic fields was negligible. These results suggest that low voltage (2 kV) is an attractive choice for EBL on 1× mask fabrication with tight control of critical dimensions.

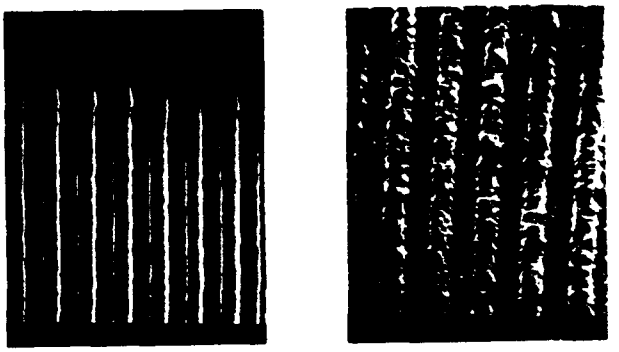

(a)

FIG. 9. SEM of 86 nm gratings of (a) dryetched Si delineated by a 2 keV electron beam along with dry-etching processing (SF_6 and C_2ClF_5 200 sccm; 150 mTorr, 500 W), and (b) dry-etched W delineated by a 2 keV electron beam along with dry-etching processing (SF_6 and $CBrF_3$ 50 sccm; 50 mTorr, 500 W).

ACKNOWLEDGMENTS

This work was supported by the Office of Naval Research under the Contract No. N00014-90-K-2000 and partly by IBM under Contract No. 192T628.

[1]G. Mollenstedt and R. Speidel, Phys. Bl. **16**, 192 (1960).
[2]O. C. Wells, T. E. Everhart, and R. K. Matta, IEEE Trans. Electron Devices **ED-12**, 556 (1965).
[3]A. N. Broers, E. G. Lean, and M. Hatzakis, Appl. Phys. Lett. **15**, 98 (1969).
[4]S. J. Wind, M. G. Rosenfield, G. Pepper, W. W. Molzen, and P. D. Gerber, J. Vac. Sci. Technol. B 7, 1507 (1989).
[5]F. J. Hohn, J. Vac. Sci. Technol. B 7, 1405 (1989).
[6]T. Abe, N. Ikeda, H. Kusakabe, R. Yoshikawa, and T. Takigawa, J. Vac. Sci. Technol. B 7, 1524 (1989).
[7]T. R. Groves, H. C. Pfeiffer, T. H. Newman, and F. J. Hohn, J. Vac. Sci. Technol. B **6**, 2028 (1988).
[8]M. A. Gesley, F. J. Hohn, R. G. Viswanathan, and A. D. Wilson, J. Vac. Sci. Technol. B **6**, 2014 (1988).
[9]T. Sakashita, N. Nomura, K. Hashimoto, T. Koizumi, K. Harafuji, A. Misaka, N. Sawada, and K. Kawakita, J. Vac. Sci. Technol. B 7, 1528 (1988).
[10]Z. W. Chen, G. A. C. Jones, and H. Ahmed, J. Vac. Sci. Technol. B **6**, 2009 (1988).
[11]K. Meissner, W. Haug, S. Silverman, and S. Sonchik, J. Vac. Sci. Technol. B 7, 1443 (1989).
[12]J. S. Greeneich and T. Van Duzer, J. Vac. Sci. Technol. **10**, 1056 (1973).
[13]G. Owen and P. Rissman, J. Appl. Phys. **54**, 3573 (1983).
[14]M. Isaacson, Scanning Electron Microsc. **1**, 763 (1978).
[15]J. S. Greeneich, J. Vac. Sci. Technol. **19**, 1269 (1981).
[16]H. Sewell, J. Vac. Sci. Technol. **15**, 927 (1978).
[17]N. D. Wittels and C. I. Youngman, *Proceedings of the Symposium on Electron and Ion Beam Science and Technology*, Eighth International Conference, edited by R. Bakish (Electrochemical Society, Princeton, NJ, 1978), p. 361.
[18]A. Kikuchi, A. Karamaru, N. Okazaki, Y. Nakane, and K. Tsuboi, J. Vac. Sci. Technol. **16**, 1764 (1979).
[19]M. Parikh and D. E. Schreiber, IBM J. Res. Dev. **24**, 530 (1980).
[20]R. E. Howard, E. L. Hu, L. D. Jackel, P. Gregge, and D. M. Tennant, Appl. Phys. Lett. **36**, 592 (1980).
[21]J. B. Kruger, P. Rissman, and M. S. Chang, J. Vac. Sci. Technol. **19**, 1320 (1981).
[22]H. C. Pfeiffer, T. R. Groves, and T. H. Newman, IBM J. Res. Dev. **32**, 494 (1988).

[23]J. B. McGinn, L. W. Swanson, N. A. Martin, M. A. Gesley, M. A. McCord, R. Viswanathan, F. J. Hohn, A. D. Wilson, R. Naumann, and M. Utlaut, J. Vac. Sci. Technol. B 9, 2925 (1991).
[24]R. F. W. Pease, *The IEEE 9th Annual Symposium on Electron, Ion, and Laser Beam Technology*, edited by R. F. W. Pease (San Francisco, San Francisco, CA, 1967), p. 176.
[25]M. A. McCord and R. F. W. Pease, J. Vac. Sci. Technol. B 4, 86 (1986).
[26]D. C. Joy, *Proceedings of the 9th European Congress of Electron Microscopy*, edited by P. J. Goodhew and H. G. Dickinson (Institute of Physics, Bristol, 1988), p. 22.
[27]R. Browning, T. Eimori, E. P. Traut, B. Chui, and R. F. W. Pease, J Vac. Sci. Technol. B 9, 3578 (1991).
[28]S. W. J. Kuan, C. W. Frank, C. C. Fu, D. R. Allee, P. Maccagno, and R. F. W. Pease, J. Vac. Sci. Technol. B 5, 2274 (1988).

EIPB · June '91

An elastic cross section model for use with Monte Carlo simulations of low energy electron scattering from high atomic number targets

R. Browning, T. Eimori,[a] E. P. Traut, B. Chui, and R. F. W. Pease
The Center for Integrated Systems, Stanford University, Stanford, California 94305

(Received 29 May 1991; accepted 26 July 1991)

The form of the screened Rutherford elastic scattering cross section has been modified to approximate the Mott scattering cross section for low energy electrons interacting with high atomic number targets, both for the total and the differential elastic cross section. A modified form of the total scattering cross section has been found that fits the Mott scattering cross section derived using a partial wave expansion. The fit is from atomic number 6–92 over the energy range 1–100 keV. The differential elastic cross section has been modeled using a screened Rutherford distribution plus an isotropic distribution. The ratio of forward to backscattering found from the Mott cross section was used as a fitting criteria. The screened Rutherford distribution is fitted to the forward scattering half-angle of the Mott distribution and the size of the isotopic distribution is then adjusted to give the correct forward to backscattering ratio. This differential form has been used in a Monte Carlo simulation of the backscattering from Au. Both the total and the differential cross sections are straightforward to implement in a Monte Carlo simulation of electron/target scattering.

I. INTRODUCTION

The simulation of electron scattering in a target using Monte Carlo methods is an important tool for the understanding of proximity effects in electron beam lithography, and in quantifying electron microscope data. For these simulations it is important to have simple but accurate models of the electron/atom scattering cross sections. A commonly used elastic scattering cross section is the screened Rutherford cross section which has a convenient analytical form and is straightforward to implement in a Monte Carlo calculation. However, the screened Rutherford cross section can only be validly used for high energy electrons and low atomic number target materials. Thus it is inaccurate for lithography and scanning electron microscopy which generally use 1–20 keV primary electron energies and a wide variety of target materials.

An alternative to the screened Rutherford cross section is the partial wave expansion of the Mott scattering cross section, which is normally used in the form of a look-up table and interpolation between data points. Here we discuss a further alternative which is to extract the trends from the Mott scattering data and apply corrections to the screened Rutherford formulation. This approach promises to give a computationally efficient implementation of the Mott scattering results.

The elastic cross section is used in two ways within a Monte Carlo simulation. The total elastic cross section is used to define a mean free path between scattering events, and the differential elastic cross section determines the angular probability of scattering. With the screened Rutherford cross section the differential cross section can both be analytically integrated over a sphere to give the total cross section, and it can be integrated over a partial solid angle to give a simple form for the scattering angle determined by a random number.[1] However, in this paper we have treated the total and the differential cross sections separately, as it is not necessary that the same cross section be used for both cases, or that a dimensionless angular distribution be integrable to an area for the total cross section. First we treat the total cross section and then the differential cross section and show simulation results for the backscattering of electrons from Au to illustrate the approach.

II. THE TOTAL ELASTIC SCATTERING CROSS SECTION

Without correction for relativistic effects, the total screened Rutherford cross section, σ_R for the scattering of an electron from a single atom can be written as

$$\sigma_R = 5.21\times10^{-21}\frac{Z^2}{E^2}\cdot\frac{\pi}{\alpha(1+\alpha)}\ \text{cm}^2, \tag{1}$$

where Z is the atomic number of the atom, E is the incident electron energy in keV, and α is a screening parameter defined as

$$\alpha = 3.4\times10^{-3}\frac{Z^{0.67}}{E}. \tag{2}$$

It can be seen that if the screening parameter α is much less than 1, which it is over much of our range of interest, then the screened Rutherford cross section scales as E^{-1} and as $Z^{1.33}$. Here we seek an equivalent expression for the Mott cross sections, σ_M, in terms of their dependence with E and Z. Reimer and Lodding[2] have tabulated results of a partial wave calculation of Mott cross sections, and here we have plotted their results as a function of the reduced electron energy $E = E\cdot Z^{1.33}$. Before reduction, this data was first multiplied by the inverse relativistic correction used by Reimer and Lodding.[2]

In Fig. 1, the total Mott elastic cross sections have been plotted for U, Au, Mo, Al, and C, using the symbols U, A, M, +, and C. The trend of the data falls into two distinct regions: one for reduced energies >0.1 for which σ_M is proportional to $E^{-1}Z^{1.33}$, in agreement with the trends seen for the screened Rutherford cross section. In the other, lower

 0734-211X/91/063578-04$01.00

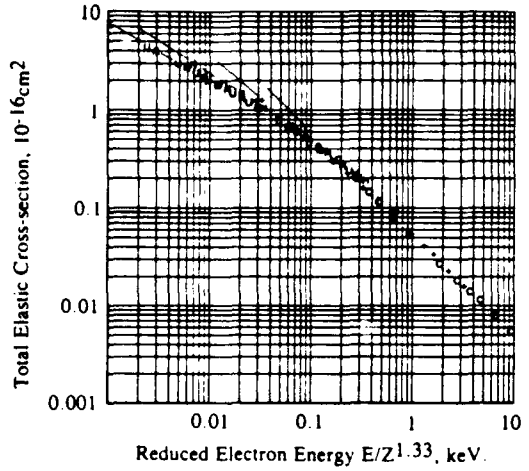

FIG. 1. Variation of the total elastic cross-section for electrons calculated using the partial wave expansion (Ref. 2) with the reduced electron energy, $E \cdot Z^{-1.33}$. The symbols are U—uranium, A—gold, M—Molybdenum, + —aluminum, C—carbon

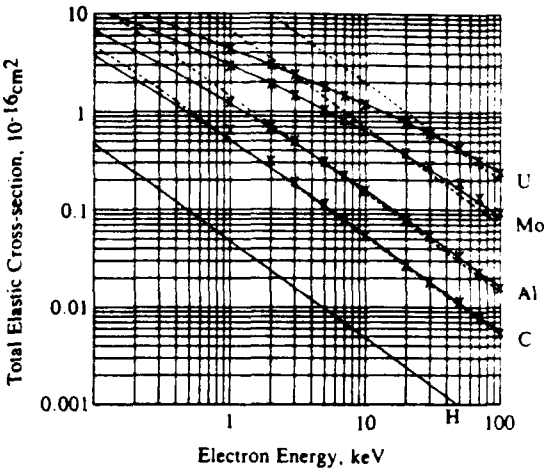

FIG. 2. Variation of total elastic scattering cross sections with electron energy. Solid line, Eq. (3) for U, Mo, Al, C, and H. Crosses are data points calculated using the partial wave expansion (Ref. 2). The dotted lines are the screened Rutherford cross sections (Ref. 1).

energy, region the results are more complex with the curves fanning out in different trajectories. For the higher atomic number materials such as Au and U the trend suggests an $E^{-0.5}$ dependence over an order of magnitude from 1–10 keV.

The observation that there is a systematic dependence of σ_M on E and Z has been made the basis for finding a universal expression. Reimer and Lodding[2] have published results or 13 elements, from atomic number 6–92, and these were used to give a fit across the Periodic Table. However, it should be pointed out that due to the variation with atomic number of the muffin tin potential used, Reimer and Lodding's[2] results are not monotonic with atomic number,[3,4] and the smooth fit discussed below ignores these variations. The largest deviations of Reimer and Lodding's[2] data from the smooth fit are in the region of the transition elements and will be larger for the rare gas atoms.[5]

The strategy for fitting the partial wave results of Reimer and Lodding[2] with a form similar to the screened Rutherford cross section has been described in detail elsewhere.[6] The initial fit across the Periodic Table used the Mott cross sections at 100 keV as the normalization point and a scaling law of $(Z^{1.33} + 0.032Z^2)$ was found. The region between the inverse linear and the inverse root regions was fitted using a Gaussian function rather than using a polynomial, and the final expression found was

$$\sigma = 4.7\times 10^{-18}\frac{(Z^{1.33}+0.032Z^2)}{(E+0.0155Z^{1.33}E^{0.5})} \times \frac{1}{(1-0.02Z^{0.5}e^{-u})}\ \text{cm}^2, \tag{3}$$

where $u = \log_{10} 8\cdot E\cdot Z^{-1.33}$.

Figure 2 shows a comparison of Eq. (3) with the results of Reimer and Lodding[2] and the screened Rutherford cross section. The continuous line is Eq. (3) and for U the fit is better than 0.5% over the range 1–100 keV. The largest deviations from Reimer and Lodding's data are in the region of the transition elements where the errors are up to 30%, largely due to departures from the initial smooth fit. The screened Rutherford cross section is plotted as a broken line in Fig. 2 and is clearly inaccurate for the larger atomic numbers.

III. DIFFERENTIAL ELASTIC CROSS-SECTION

As will be shown below, the form of the angular distribution of scattering makes a significant contribution to the accuracy of a Monte Carlo simulation. It has previously been pointed out by Kotera *et al.*[7] that the average scattering angle from the screened Rutherford cross section is much larger than that for the Mott cross section. The average scattered angle for the Rutherford cross section can be calculated analytically from

$$\theta_{\text{average}} = \frac{\int_0^\pi \theta\cdot\sin\theta\cdot(d\sigma/d\theta)d\theta}{\int_0^\pi \sin\theta\cdot(d\sigma/d\theta)d\theta}, \tag{4}$$

giving

$$\theta_{\text{average}} = \pi\sqrt{\alpha}\cdot\sqrt{1+\alpha} - \pi\alpha. \tag{5}$$

Equation (5) is plotted in Fig. 3 along with data taken from Reimer and Lodding[2] for Au. It can be seen that the average scattering angle using the screened Rutherford cross section is always larger than the corresponding average angle for the Mott cross section between the energies 1–100 eV. Equation (5), suggests the possibility of correcting the screened Rutherford formula to give a similar average angle as the Mott by decreasing the screening parameter. The formula

$$\alpha = (0.6 - 0.0035\cdot E)\cdot\alpha_R \tag{6}$$

gives the result shown as curve (c) in Fig. 3.

Although this approach seems reasonable this does not produce a scattering cross section that is similar to the Mott cross section. Figure 4 shows the form of the differential cross sections for 1 keV electron scattering from Au. In this figure the cross sections have been normalized at 0°. The screened Rutherford differential cross section, Fig. 4(a) is much broader than the Mott, Fig. 4(b), and it can be seen

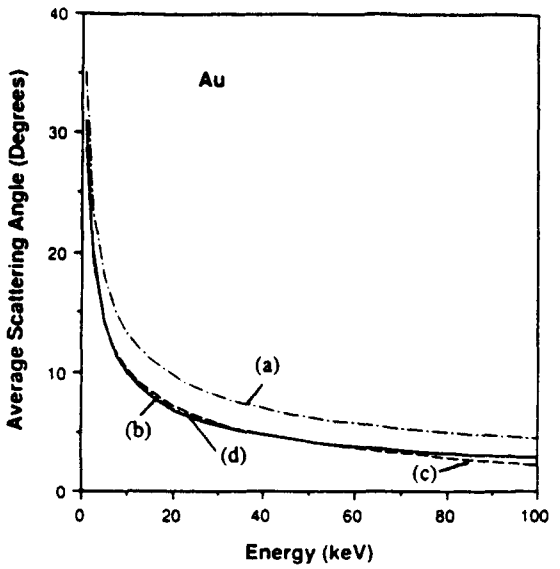

FIG. 3. Average scattering angle as a function of electron energy, for (a) screened Rutherford, (b) partial wave (Mott) (Ref. 2), (c) the screened Rutherford using the screening parameter Eq. (6), (d) the screened Rutherford plus isotropic distribution ratioed using Eq. (8)

that although the average angle is reduced by using Eq. (6), Fig. 4(c), because the high angle scattering is reduced, the small angle scattering is not like the corresponding Mott form, and the ratio of the forward to backscattered probabilities are overestimated by a factor 2.

As we wish to fit both the forward and backscattering distributions to give a realistic model an alternative is to split the Mott distribution into two parts, one part for the small angle forward scattering, and the other the backscattering contribution. The forms for these two parts of the distribution were chosen to be the screened Rutherford cross section

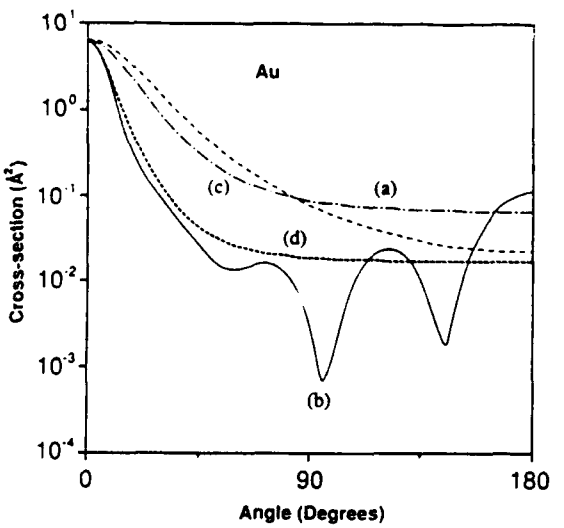

FIG. 4. Differential scattering cross section as a function of angle for 1 keV electrons scattering from Au. (a) Screened Rutherford. (b) Partial wave (Mott) (Ref. 2). (c) Screened Rutherford using the screening parameter Eq. (6). (d) The screened Rutherford plus isotropic distribution ratioed using Eq. (8).

and an isotropic distribution. The reason for this choice being that both forms give a simple formula for the scattering angle dependence on a random number.

The division of the scattering distribution into forward and backscattering parts can be justified by observing that in most simulations there is multiple elastic scattering before the electron comes to rest or exits the target. For example a 10 keV electron backscattered from Au, undergoes on average ten elastic collisions. Thus the differential scattering distribution is self-convolved several times, and while the narrow forward scattering half-angle and the ratio of the distributions are preserved, the broad features of the backscattering distribution are averaged out.

The screened Rutherford distribution was first modified by changing the screening parameter to fit the forward scattering of the Mott distribution at the half-heights. An isotropic distribution was then added to give the correct weighted scattering. Using the average scattering angle criteria produces the distribution shown as (d) in Fig. 4. This distribution is now more similar to the general trend of the Mott cross section, but underestimates the ratio of the forward to backscattering contribution. A similar curve (not shown) is produced using the alternative criteria that the ratio of the screened Rutherford distribution to the isotopic distribution is determined by the ratio of the forward ($<90°$) to backscattering ($>90°$) probability. The best fit of the half-angle of the screened Rutherford distribution to the Mott half-angle is obtained using

$$\alpha = 5.5\times 10^{-4} Z^{0.67}/E. \tag{7}$$

The two backscattering criteria give similar trends for the ratio of the screened Rutherford to isotopic distributions over the range 1–100 keV. For the average angle criteria

$$\frac{\sigma_R}{\sigma_{\text{Isotropic}}} = 3.9E^{0.72} \tag{8}$$

and the forward/backscattering ratio criteria

$$\frac{\sigma_R}{\sigma_{\text{Isotropic}}} = 4.2E^{1.1}. \tag{9}$$

For Eq. (9) the explicit expression for the differential cross section is then

$$\frac{d\sigma}{d\Omega} = 5.21\times 10^{-21}\frac{Z^2}{E^2} \times\left[\frac{1}{(1-\cos\theta-\alpha)} + \frac{\alpha(\alpha+1)}{4.2E^{1.1}}\right], \tag{10}$$

where α is defined in Eq. (7).

The effect of using the different criteria can be judged from the results of a Monte Carlo simulation of the backscattering factor for Au between 0.5 and 10 keV. The inelastic cross section used was the Bethe continuous slowing down approximation with the Rao-Sahib–Wittry[8] low energy extension. In Fig. 5 the upper curve (a) is the result of using the conventional uncorrected screened Rutherford cross section [Eqs. (1) and (2)]. Using the empirical total cross section [Eq. (3)], and the differential screened Rutherford cross section gives a result that is intermediate between the conventional screened Rutherford model and the experimental results. Using Eq. (6), the modified screening

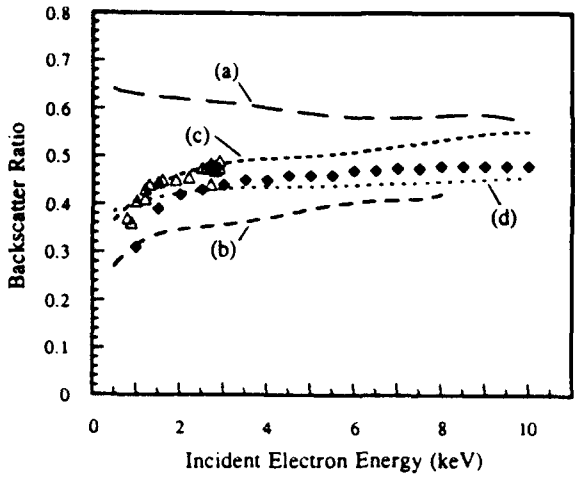

FIG. 6. Variation of backscattering coefficient at normal incidence with electron energy for Au. (a) Screened Rutherford. (b) Screened Rutherford using the screening parameter Eq. (6). (c) Screened Rutherford plus isotropic distribution ratioed using Eq. (8). (d) Screened Rutherford plus isotropic distribution ratioed using Eq. (9). Experimental data points △ (Ref. 9) and ▲ (Ref. 10).

parameter, gives too low a result, (b). The effects of the different criteria on the combined cross-section (screened Rutherford plus isotropic) can be seen in the difference between curves (c) and (d) of Fig. 5. The backscattering appears higher between 1–10 keV for the average scattering angle criteria than for the forward/backscattering criteria. The experimental results in this range are bracketed by these two curves in this energy range, but the forward/backscattering criteria gives results closer to experiment at higher energies up to 100 keV.

The differential cross-section comprising the modified screened Rutherford distribution plus an isotropic distribution can be implemented very simply in the standard Monte Carlo program. The choice of which part of the distribution to be used at any scattering event can be made by an additional random number weighting the relative areas of the distributions given by Eq. (9). The cosine of the scattering angle (a), is then given by the conventional formula[1] for the screened Rutherford part, and by $\cos\theta = 1 - 2R$, where R is a random number between 0–1, for the isotropic distribution.

IV. CONCLUSIONS

At energies above $0.1 \times Z^{1.33}$ keV the total elastic cross-sections derived from a partial wave expansion of Mott scattering of electrons from target atoms scales as $E^{-1}Z^{1.33}$. At lower energies the cross section scales approximately proportionally to $E^{-0.5}$. Using these trends a fit can be found that covers the range of atomic numbers from 6–92 and over the range 1–100 keV.

A form for the differential elastic cross section using a screened Rutherford distribution plus an isotropic distribution can be found that produces the correct magnitude for the forward to backscattering ratio over the energy range 1–100 keV. This form of the differential cross section is straightforward to implement in a Monte Carlo simulation of electron/target scattering, and gives results comparable to the experimental results for the backscattering factors from Au.

ACKNOWLEDGMENTS

This work was supported by the Office of Naval Research Contract No. N00014-90-K-2000. Our thanks to Professor Reimer and Dr. Lodding for their helpful correspondence.

[a] Visiting scholar from Mitsubishi Electric Corporation.

[1] D. C. Joy, *Proceedings of the 9th European Congress of Electron Microscopy*, edited by P. J. Goodhew and H. G. Dickinson (Institute of Physics, Bristol, 1988), p. 22.
[2] L. Reimer and B. Lodding, Scanning **6**, 128 (1984).
[3] L. Reimer and B. Lodding (private communication).
[4] H. Raith, Acta. Cryst. A **24**, 85 (1968).
[5] M. E. Riley, C. J. MacCallum, and F. Biggs, Atomic Data Nucl. Tables **15**, 443 (1975).
[6] R. Browning, Appl. Phys. Lett. **58**, 2845 (1991).
[7] M. Kotera, K. Murata, and K. Nagami, J. Appl. Phys. **52**, 997 (1981).
[8] T. S. Rao-Sahib and D. B. Wittry, J. Appl. Phys. **45**, 5060 (1974).
[9] J. Schou and H. Sorensen, J. Appl. Phys. **49**, 816 (1978).
[10] L. Reimer and H. Drescher, J. Appl. Phys. **10**, 805 (1977).

Universal elastic scattering cross sections for electrons in the range 1–100 keV

R. Browning
The Center for Integrated Systems, Stanford University, Stanford, California 94305

(Received 13 December 1990; accepted for publication 15 March 1991)

For high atomic numbers the total cross section for electron-atom elastic scattering calculated using the partial-wave method is found to fall into two regimes over the range 1–100 keV. The cross section in the higher energy regime scales as E^{-1}, and in the lower energy regime as $E^{-0.5}$. An empirical equation has been drawn up that describes these trends, and can give a universal expression for the cross sections over the Periodic Table to allow economical Monte Carlo simulation of electron scattering over a wide range of energies and materials.

In the x-ray and Auger microprobes it is becoming important to have a simple but accurate model of the electron scattering cross sections to perform quantitative analysis using Monte Carlo simulations. The most commonly used elastic cross section for this purpose is the screened Rutherford cross section. However, the screened Rutherford cross section is only valid over a limited range of electron energies and materials, and becomes inaccurate in the range of interest to scanning electron microscope (SEM) analyses which generally use 2–30 keV primary electron energies. The alternative, which is the use of the more accurate method of partial-wave expansion using the Mott scattering formula, is too computationally intensive to be presently useful in on-line simulations. Here we report a universal total elastic scattering cross section derived from partial-wave Mott scattering data, which like the Rutherford cross section is simple to implement, but is accurate over a wide range of materials (carbon to uranium) and electron energies (1–100 keV).

Without a correction for relativistic effects, the screened Rutherford cross section σ_R from a single atom can be written as[1]

$$\sigma_R = 5.21\times10^{-21}\frac{Z^2}{E^2}\cdot\frac{\pi}{\alpha(1+\alpha)}\ \text{cm}^2, \tag{1}$$

where Z is the atomic number of the atom, E is the incident electron energy in keV, and α is a screening parameter defined as

$$\alpha = 3.4\times10^{-3}(Z^{0.67}/E). \tag{2}$$

It can be seen that if the screening parameter α is much less than 1, then the screened Rutherford cross section scales as E^{-1} and as $Z^{1.33}$. Here we seek an equivalent expression for the Mott cross sections σ_M in terms of their dependence with E and Z. Reimer and Lodding[2] have tabulated results of a partial-wave calculation of Mott cross sections, and here we have plotted their results as a function of reduced electron energy $\bar{E}\equiv E.Z^{-1.33}$, Fig. 1. Before reduction the data were multiplied by the inverse of the relativistic correction used by Reimer and Lodding.[2]

There are two distinct regions: one for reduced energies >0.1, for which σ_M is proportional to $E^{-1}Z^{1.33}$, agreeing with the screened Rutherford cross section. In this region the reduced total cross sections for U(92), Au(79), Mo(42), Al(13), and C(6) are similar, and close to the figure for the Rutherford cross section. The other region, for reduced energies <0.1, is more complex with the curves for the different elements fanning out in different trajectories. However, the results suggest a $\bar{E}^{-0.5}$ dependence over an order of magnitude, from 1 to 10 keV in Au and U.

The observation that there is a systematic dependence of σ_M on E and Z is the basis for finding a universal expression. The results of Reimer and Lodding[2] are from 1 to 100 keV, and for 13 elements from C to U. There are some difficulties in the data set for fitting purposes. First, due to the muffin-tin potential used[3,4] the results are not monotonic with atomic number. The physical reason for this is the variation in atomic size, and is most marked in the rare-gas atoms.[5] Second, there are some unexpected trends and inconsistencies. For example, the cross section for C at 1 keV is larger than would be expected from the Rutherford cross section and the higher energy trends.

A normalization point for each atomic number was

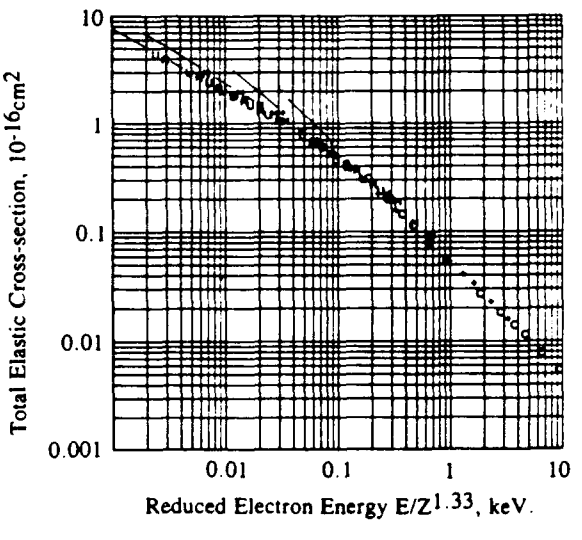

FIG. 1. Log-log plot of the total elastic scattering cross section for electrons calculated using the partial-wave expansion (Ref. 2) vs the reduced electron energy $E.Z^{-1.33}$. The symbols are U—uranium, A—gold, M—molybdenum, + —aluminum, and C—carbon.

 0003-6951/91/242845-03$02.00

first established by using the total elastic cross section at 100 keV as a base for the trends towards lower energy. The Rutherford cross section scales as the power 1.33 with atomic number but this produces a value that falls below the Mott cross section at high atomic numbers. A smooth fit to the Mott cross sections at 100 keV can be found using the expression $Z^{1.33} + 0.032Z^2$. This expression also compensates for the departure from a simple atomic number scaling law caused by the energy scaling terms discussed below.

For one atomic number it was straightforward to find the fitting constants in the inverse linear and the inverse root regions separately. However, finding a fit over the entire energy range using just E^{-1} and $E^{-0.5}$ terms was inaccurate, and a polynomial using several partial root terms was found necessary to give the correct transition between the regions. This polynomial was cumbersome, and as an alternative a Gaussian weighting function was used to correct the region between the inverse root and the inverse linear regions. The function used was

$$\frac{1}{(1-0.02Z^{0.5}e^{-u^2})},$$

where

$$u=\log_{10}8.E.Z^{-1.33}. \tag{3}$$

This function has two constants and two dependencies with atomic number. These dependencies were arrived at by observing in the first place that the deviation from inverse linearity occurs at approximately the same total cross section. As the total cross section scales in energy with $Z^{1.33}$, then the crossover point also scales this way. In fact, there is not quite enough range in the data to be definite about this trend. Second, the knee in the data is shallower with decreasing atomic number and the Gaussian correction term need not be as large for small Z. A square root scaling with atomic number was used, and although again the data does not extend quite far enough to fix this dependence, the maximum correction at atomic number 92 from the Gaussian term is only 20% and thus an exact scaling towards lower atomic numbers is not critical.

The final problem is to find the main dependence of the inverse root multiplier term over the entire periodic table. Scaling in the same way that the knee is scaled, with a $Z^{1.33}$ dependence, gives a maximum error of 3% over the range 1–10 keV for Al, Mo, and U. Fixing the constants using the best fit to the U data gives the complete empirical equation

$$\sigma=4.7\times10^{-18}\times\frac{(Z^{1.33}+0.032Z^2)}{(E+0.0155Z^{1.33}E^{0.5})}\cdot\frac{1}{(1-0.02Z^{0.5}e^{-u^2})},\ \text{cm}^2. \tag{4}$$

A comparison of the empirical equation (4) with the screened Rutherford and Mott results for U, Mo, Al, and C is shown in Fig. 2. Also shown is the comparison of Eq. (4) and the screened Rutherford cross section for H. The empirical equation is shown as a solid line, data from the Reimer and Lodding[2] tabulation without relativistic correction is shown as crosses, and the dashed line is the Rutherford cross section using the form given by Eq. (1).

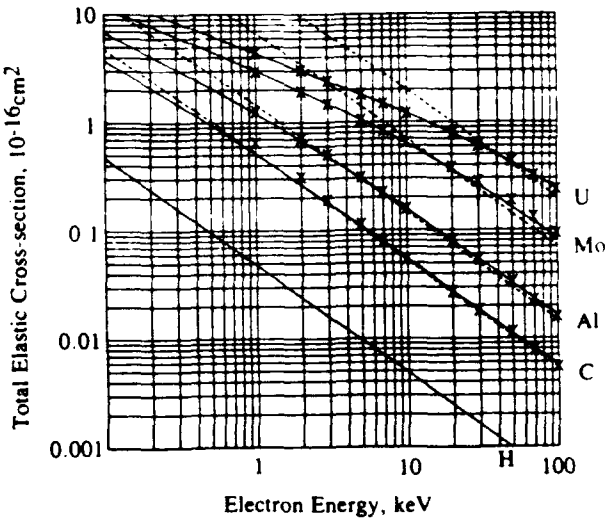

FIG 2. Log-log plot of total elastic scattering cross sections vs electron energy. Solid line, Eq. (4) for U, Mo, Al, C, and H. Crosses are data points calculated using the partial-wave expansion (Ref. 2). The dotted lines are the screened Rutherford cross sections (Ref. 1).

In comparison with the tabulated Mott data, the maximum error using Eq. (4) for U from 1 to 100 keV is 0.5%, while for Pb and Au the maximum error is < 5% over the range 10–100 keV and a maximum of 3% below 10 kev. It can be seen from Fig. 2 that the resultant fit for Mo in the inverse root region is good. The overall fit for Mo is similar to Sb and Ag with a maximum error of 10% at 100 keV and 3% at 1 keV. The result for the midrange to lower atomic numbers is not quite as good. The maximum errors in the range of atomic numbers from 20–40 is as high as 30% with a typical error in the 10% range. The source of the larger errors is the initial smooth fit over the nonmonotonic trend of the cross sections at 100 keV.

The fitting error for Al and Si is better than 4% over the whole energy range while the fit for C is better than 3% for 5 to 100 keV. The fit is poor for C below 3 keV, and 30% in error at 1 keV. However, the trend of the fit drops slowly below the Rutherford cross section towards lower energies, as would be expected. For the lower atomic numbers the validity of some of the scaling terms would only been seen in the low-energy region. Using the parameters that match the Mott cross section data that has only been presented graphically by Ichimura and Shimizu[6] (replacing 0.0155 with 0.02 in the inverse root term), the fit for Al is reasonable below 1 keV, and within the disparity found between using the alternative Thomas–Fermi–Dirac and the Hartree–Fock potentials.[6]

In summary, at energies above $0.1\times Z^{1.33}$ the total elastic scattering cross sections σ_M, derived using a partial-wave method scale as $E^{-1}Z^{1.33}$. At lower energies σ_M is approximately proportional to $E^{-0.5}$. An empirical equation has been drawn up that is a reasonable description of the total elastic scattering cross section over the entire periodic table with energies from 1 to 100 keV. The equa-

tion is simple enough for economic use within a Monte Carlo simulation. Further versions of this equation might well accommodate a much wider range of energies.

This work was supported by ONR contract No. N00014-90-K-2000 and IBM contract No. 192T467. My thanks to Professor R. F. Pease for his many helpful comments, and to Professor Reimer and Dr. Lodding for their helpful correspondence.

[1] D. C. Joy, *Proceedings of the 9th European Congress of Electron Microscopy*, edited by P. J. Goodhew and H. G. Dickinson (Institute of Physics, Bristol, UK, 1988), p. 22.
[2] L. Reimer and B. Lodding, Scanning **6**, 128 (1984).
[3] L. Reimer and B. Lodding (private communication).
[4] H. Raith, Acta. Crystallogr. Sect. A **24**, 85 (1968).
[5] M. E. Riley, C. J. MacCallum, and F. Biggs, At. Data Nucl. Tables **15**, 443 (1975).
[6] S. Ichimura and R. Shimizu, Surf. Sci. **112**, 386 (1981).

EIPBTS June '91

Silicon on quartz reflective masks for 0.25-μm microlithography

Y. H. Lee, R. L. Hsieh, A. Grenville, R. von Bünau, C. C. Tsai,[a] D. A. Markle,[b] G. Owen,[c] R. Browning, and R. F. W. Pease
Stanford University, Stanford, California 94305

(Received 30 May 1991; accepted 9 July 1991)

One approach to 0.25-μm lithography currently being explored is the unity-magnification Markle-Dyson projection system. This system, operating at $\lambda = 248$ nm, incorporates a reflective mask in its design. This utilizes the internal reflection at the quartz/film interface. To best meet the requirements of high reflectivity and quarter micron processing, amorphous silicon on quartz masks were chosen. Completed masks were used to print 0.19-μm lines and spaces on the prototype Markle–Dyson system, demonstrating the feasibility of silicon reflective masks for lithography.

I. INTRODUCTION

Integrated circuit lithography is typically done using 5× reduction optics; but as feature sizes decrease, corresponding diffraction-limited reduction lenses become increasingly complicated to design and to build. Projection optics design can be greatly simplified by going to a unity-magnification system. One such approach to 0.25-μm patterning uses a two element catadioptic Markle–Dyson projection lens, having an NA = 0.7 and operating at $\lambda = 248$ nm.[1] This system is a working prototype for a scaled up production stepper. A key feature of the Markle–Dyson configuration is the 1× reflective mask. In this article we describe the design, fabrication, and testing of reflective masks for this system.

The reflective mask design, illustrated in Fig. 1, consists of a flat quartz (fused silica) substrate with a patterned reflective film on the back surface. In operation, these masks utilize the internal reflection at the quartz/film interface. To improve object contrast and to diminish stray light transmission, the patterned reflective film is coated with an absorber film: this reduces the reflectivity of the spaces between the reflective pattern to about 1 %. In plan view, the object half-plane contains reflector and absorber structures, and the adjacent image half-plane is a clear quartz window. In the following discussions reflectivity of a film refers to the reflectivity in quartz at the quartz/film interface at $\lambda = 248$ nm. Normal incidence is assumed unless otherwise noted.

II. THICK FILM REFLECTION

The amplitude reflectivities of a plane wave at the boundary between two dielectric media of refractive indices n_1 and n_2 may be calculated using the Fresnel equations[2]:

$$r_\perp = \frac{n_1 \cos\theta_1 - n_2 \cos\theta_2}{n_1 \cos\theta_1 + n_2 \cos\theta_2}, \tag{1}$$

$$r_\parallel = \frac{n_2 \cos\theta_1 - n_1 \cos\theta_2}{n_2 \cos\theta_1 + n_1 \cos\theta_2}. \tag{2}$$

Here ⊥ and ∥ denote electric polarization perpendicular and parallel, respectively, to the plane of incidence; θ_1 and θ_2, the direction of wave propagation in media 1 and 2 respectively, are related by Snell's law:

$$\frac{\sin\theta_1}{\sin\theta_2} = \frac{n_2}{n_1}. \tag{3}$$

For the reflective mask design, medium 1 is a dielectric; but medium 2 is absorbing, having a complex refractive index denoted by $\mathbf{n}_2 = n_2 + j\kappa_2$. For this case, Eqs. (1), (2), and (3) still hold if n_2 is replaced by $\mathbf{n}_2$. By the Snell law relationship, the angle of reflection also becomes complex, and is denoted here by $\boldsymbol{\theta}_2$: θ_2 must be replaced by $\boldsymbol{\theta}_2$ in Eqs. (1) and (2). The resulting complex Fresnel equations are used to calculate results described in Sec. IV.

For amplitude reflectivity written in the form $r = \rho \exp(j\delta)$, the phase shift upon reflection is δ. At normal incidence $\delta_\perp = -\delta_\parallel = \delta$. The negative sign for the parallel polarization arises from rotation of the coordinate system about the transverse axis upon reflection.

The intensity reflectivity R is given by

$$R_\perp = |\mathbf{r}_\perp|^2, \tag{4}$$

$$R_\parallel = |\mathbf{r}_\parallel|^2. \tag{5}$$

This gives, at normal incidence,

$$R_\perp = R_\parallel = R = \frac{(n_1 - n_2)^2 + \kappa_2^2}{(n_1 + n_2)^2 + \kappa_2^2}. \tag{6}$$

The above equation holds for films sufficiently thick that

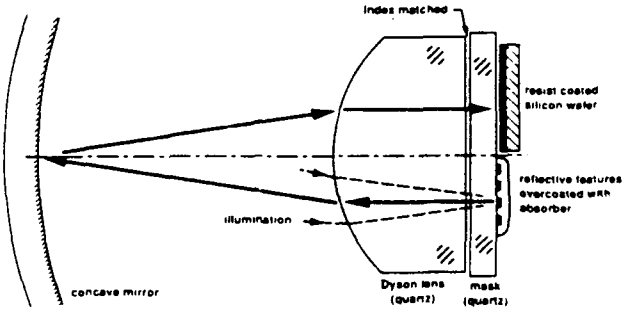

FIG. 1. Application of reflective mask in the Markle–Dyson optical projection system (Ref. 1).

 0734-211X/91/063138-05$01.00

negligible intensity is transmitted to the back side. For all following discussions, "reflectivity" refers to intensity reflectivity.

Within a medium, attenuation of transmitted intensity I_t, relative to its initial value I_0, can be written as

$$\frac{I_t}{I_0} = \exp\left\{\frac{-z}{d_{1/e}}\right\}, \tag{7}$$

where z is the depth into the medium and $d_{1/e}$ is the absorption depth, which can be written as

$$d_{1/e} = \frac{\lambda}{4\pi\kappa}. \tag{8}$$

Values of reported refractive index data for aluminum, amorphous silicon (a-Si), silicon, chromium, and novolak photoresist are listed in Table I, along with calculated reflectivity, phase shift upon reflection, and absorption depth. These refractive index values are used for all calculations reported here. Refractive index values listed for novolak photoresist are estimates based on observed behavior.

III. REFLECTIVITY VS THICKNESS

To find the reflectivity for films thin enough to transmit, a calculation for a stratified absorbing medium is required.[2] Results from this calculation are shown in Fig. 2, which shows calculated plots of reflectivity vs film thickness for quartz coated with aluminum, silicon, amorphous silicon, chromium, or photoresist. For the reflective mask geometry, incident light comes from within the quartz ($n = 1.5084$), and beyond the film is air ($n = 1.0$). The reflectivities of the four reflective materials approach the bulk value at the film thickness of 30 nm, corresponding to roughly five times $d_{1/e}$ (Sec. II). Being able to utilize thinner films allows one to reduce etch selectivity requirements, thereby increasing process latitude for film patterning.

IV. OBLIQUE REFLECTION

A calculation based on the complex Fresnel equations was used to study the reflectivity for a thick film at oblique incidence. Results from this calculation are presented in Fig. 3, which shows (a) reflectivity and (b) phase shift upon reflection,[9] both vs angle of incidence in the fused silica medium. A typical partial coherence factor σ of 0.5 in the Markle–Dyson projection system (NA = 0.7) corresponds to a maximum angle of 0.23 rad(= arcsin[σ*NA/1.5084]). At the small angles used for mask illumination, the splitting of perpendicular and parallel polarizations is minimal. Since highly reflective materials for this mask application will have large values of κ, their phase shifts tend to have similar values. Thus large phase differences, which would be desired for phase masks, cannot be obtained between highly reflective materials in the same plane.

TABLE I. Complex refractive index for various materials at $\lambda = 248$ nm, together with corresponding intensity reflection coefficients with respect to quartz, phase shift upon reflection, and absorption depth.

Material	n	κ	R	δ(rad)	$d_{1/e}$(nm)
Quartz[a]	1.5084	0.00	...	...	...
a-Si[b]	1.66	3.38	0.533	− 2.43	5.84
Si[c]	1.570	3.565	0.573	− 2.45	5.54
Al[d]	0.19	2.94	0.901	− 2.20	6.71
Cr[e]	1.36	1.91	0.309	− 2.08	10.33
Air	1.00	0.00	0.040	0.00	...
Photoresist	1.8	0.1	0.009	− 2.84	197.4

[a] Reference 3.
[b] References 4 and 5.
[c] References 4 and 6.
[d] References 4 and 7.
[e] Reference 8.

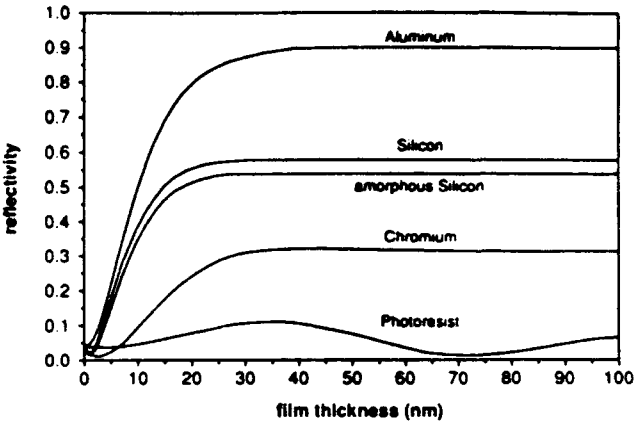

FIG. 2. Calculated normal incidence quartz/film reflectivity vs film thickness for aluminum, silicon, amorphous silicon, chromium, and novolak photoresist.

V. OBJECT CONTRAST

Object contrast M_0 for the reflective mask depends on the relative reflectivities of the reflector and absorber materials:

$$M_0 = \frac{R_r - R_a}{R_r + R_a},$$

where R_r and R_a are reflectivities of reflector and absorber, respectively. For typical optical imaging systems, image contrast is a decreasing function of image spatial frequency. Since reliable imaging requires having adequate contrast for the recording medium (photoresist), decreasing the starting object contrast will therefore decrease the resolution at the image. A reasonable goal is to have a starting object contrast of at least 95%.

VI. REFLECTOR MATERIAL SELECTION

Chromium, aluminum, and silicon were studied as possible reflector materials. Of these, chromium has low reflectance and would offer marginal contrast performance with most resist-type absorber materials. Aluminum has high reflectance but is difficult to pattern to 0.25-μm geometries. Silicon offers an appealing compromise in that it has approximately 55% reflectivity; it has well-behaved etching characteristics; and it has a 5:1 etch selectivity compared with PMMA resist (using the process described in Sec. VII). Using a silicon reflector and a novalak photoresist absorber

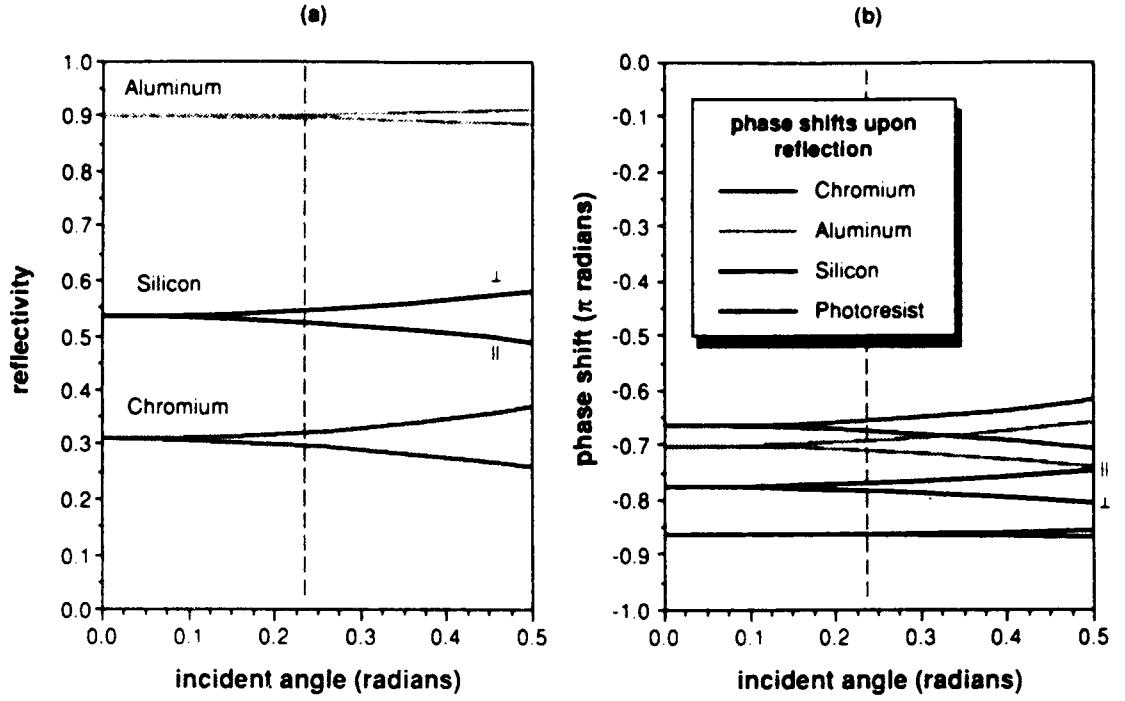

FIG. 3. (a) Quartz/film interface reflectivity vs incident angle, (b) phase shifts upon reflection vs incident angle. Perpendicular and parallel polarizations plotted for Al, Si, Cr, and photoresist.

with a reflectance of 1% gives an object contrast of 96%.

Amorphous silicon has better etching behavior for fine patterning compared to that of polysilicon. Figure 4 shows that polysilicon films have a rougher etched texture than identically etched amorphous silicon (using the process outlined in Sec. VII). Both films are deposited on silicon test wafers. The polycrystalline film shows grain delineation arising from etch rate differences between grain and grain boundary regions and between different grain orientations. The finer microstructure of the amorphous silicon film etches more uniformly than does a polycrystalline film.

The best quality amorphous silicon films used were grown using a PECVD process.[10] These films were either intrinsic, or doped with phosphorus. The effect of doping did not noticeably affect measured reflectivity, which was measured using a Nanometrics reflectometer, for which measurement uncertainty is estimated to be $\pm$ 5%. Reflectivity measurements of quartz wafers with various amorphous silicon film thicknesses are shown in Fig. 5. These show a 55% saturated reflectance at thicknesses greater than approximately 30 nm. Thus, films of 30 nm or greater yield the expected reflectance

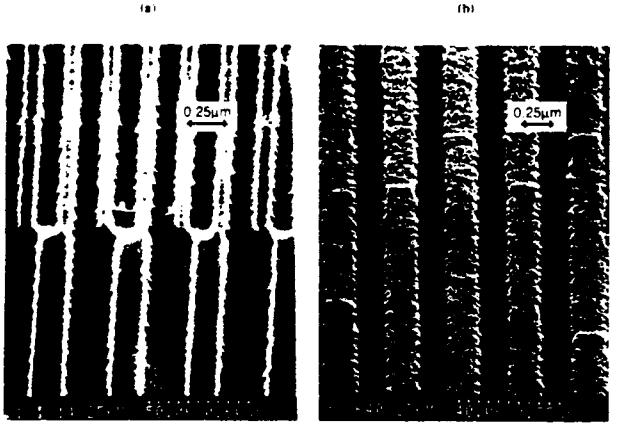

FIG. 4. Nominal 0.25-μm line and space pattern in (a) amorphous silicon film and (b) polysilicon film. Both are films on silicon wafers and are etched under identical plasma etching conditions. Finer microstructure for amorphous film gives smoother pattern delineation. Note nominal 0.13-μm line and space pattern produced in amorphous silicon [top half of 4(a)].

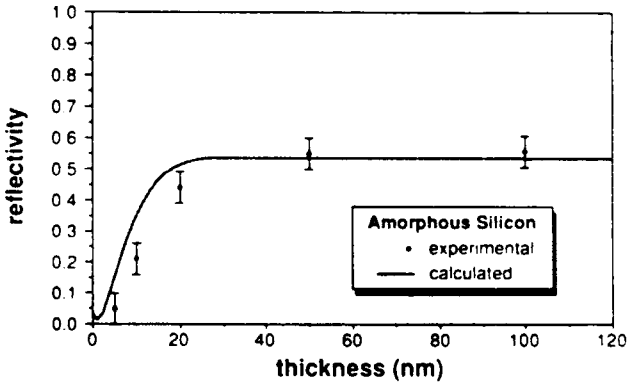

FIG. 5. Quartz/film reflectivity measurements of amorphous silicon vs film thickness.

calculated from tabulated refractive index data. This agreement indicates that interfacial smoothness and film quality are good. Patterned amorphous silicon on quartz reflective masks were made with film thicknesses of 30, 50, and 100 nm.

VII. REFLECTIVE MASK FABRICATION

A. Electron-beam lithography

A quartz mask substrate was coated with an amorphous silicon film which can be doped to obtain an electrical conductivity sufficient for charge dissipation during electron-beam writing. This was then spin coated with 30- to 50-nm thick PMMA electron-beam resist and prebaked at 120 °C for 6 h. Next, pattern exposure was done at 10 keV using a modified MEBES I electron-beam patterning system. After exposure, the PMMA was developed in a solution of 1:3 methyl-isobutyl-ketone (MIBK): isopropanol for 50 s and post-baked at 120 °C for 30 min. Since the mask pattern is written without proximity effect correction, the resist thickness is kept thin. Incorporating a proximity effect correction scheme would allow thicker resists to be used.

B. Plasma etching

With optimized etching conditions, the developed PMMA resist layer serves as an effective plasma etch mask for a thin silicon film. A favorable combination of high etch selectivity and low lateral etching was obtained using a combination of SF_6 and C_2F_5Cl gases in a Drytek plasma etcher (both gases at 200 sccm; 150 mTorr, 500 W). These conditions give an etch selectivity of 5:1 for PMMA on silicon, calibrated by etching PMMA masked silicon wafers. This is illustrated in Fig. 6, which shows 0.4-μm-deep trenches etched in silicon using a 75-nm-thick PMMA etch mask.

C. Patterning the absorber

The final step in the mask process is to pattern the absorber layer over the reflective pattern. The absorber material is a standard *g*-line photoresist (Shipley 1813) spin-deposited to 1–1.5-μm thick and patterned using conventional optical lithography. The absorber layer also serves as a protective coating for the patterned reflector features.

VIII. MASK INSPECTION

Figure 7 shows SEM micrographs of a reflective mask (with absorber removed) taken at 25 KeV. These show 0.25-, 0.38-, and 0.5-μm pitch line and space patterns. The patterned film is 100-nm-thick undoped amorphous silicon on quartz, with 20 nm of gold evaporated onto the surface to minimize SEM charging effects. After inspection the conductive gold layer can be wet etched in a solution of potassium iodide and iodine without harming the silicon features. High performance optical inspection methods such as confocal microscopy, solid immersion microscopy, and near-field microscopy are also being investigated

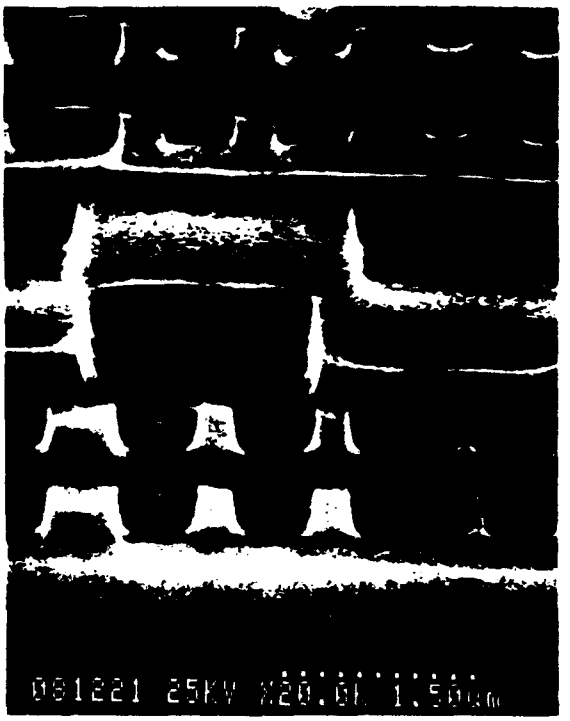

FIG. 6. 400-nm deep trenches plasma etched into silicon using a 75-nm-thick PMMA etch mask, illustrating a 5:1 etch selectivity. Sidewall fillets can be minimized by operating below the selectivity limit of PMMA as shown in Figs. 4 and 7.

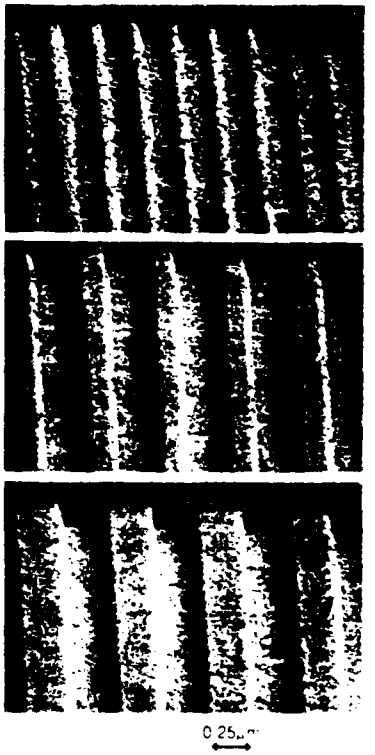

FIG. 7. SEM micrographs of 100-nm-thick amorphous silicon on a quartz mask taken at 25 keV, 85° tilt. Same magnification. Samples coated with 20-nm gold to minimize SEM charging effects.

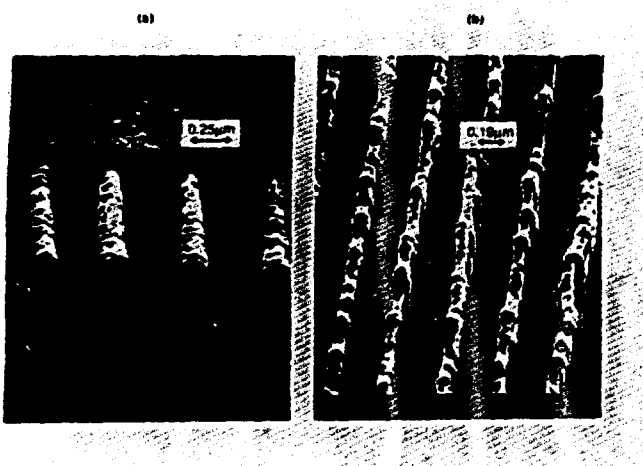

FIG. 8. (a) 0.25- and (b) 0.19-μm line and space patterns in 1.0-μm-thick bi-layer photoresist, made from the projected image of an amorphous silicon reflective mask.

IX. PROJECTION LITHOGRAPHY

A completed reflective mask, shown without absorber coating in Fig. 7, was imaged using the Markle–Dyson system to produce 0.25-μm nominal line and space features in a 0.5-μm-thick Shipley SNR248 negative resist, and 0.19-μm nominal line and space features in a 1.0-μm-thick IBM bi-layer positive photoresist.[10,11] Figure 8 shows projection images of (a) 0.25- and (b) 0.19-μm line and space patterns in a 1.0-μm-thick bi-layer photoresist.

X. CONCLUSIONS

Modeling and experimental measurements show that silicon films thicker than 30 nm are well suited for the reflective mask application. Of the various types of silicon films investigated, amorphous silicon films offer the best combination of reflectivity and processing advantages for fine patterning. Measured reflectance for films at least 30 nm thick are comparable to calculated values. This shows that high object contrast for a reflective mask is possible in practice. Working reflective masks with 0.25 μm and finer features were fabricated and successfully imaged in projection. This clearly demonstrates the feasibility of using reflective masks for high resolution optical projection patterning.

ACKNOWLEDGMENTS

The authors are grateful to Paul Jerabek for his help with the electron-beam exposure experiments. This work was supported in part by the Office of Naval Research (Contract No. N00014-90-K-2000), the Semiconductor Research Corporation (Contract No. 90MC500-1), and by IBM (Contract No. 63426QSXAB22G).

[a] Xerox, Palo Alto, CA 94303.
[b] Ultratech Stepper, Santa Clara, CA 95054.
[c] Hewlett Packard, Palo Alto, CA 94303.

[1] A. Grenville, R. L. Hsieh, R. von Bünau, Y-H. Lee, D. A. Markle, G. Owen, and R. F. W. Pease, J. Vac. Sci. Technol. B 9, 3108 (1991).
[2] M. Born and E. Wolf, *Principles of Optics*, 6th ed. (Pergamon, Oxford, 1980).
[3] I. H. Malitson, J. Opt. Soc. Am. 55, 1205 (1965).
[4] Reported refractive index data for Al, Si, and *a*-Si were analyzed and tabulated in E. D. Palek, *Handbook of Optical Constants of Solids* (Academic, Orlando, 1985).
[5] G. Weiser, D. Ewald, and M. Milleville, J. Non-Cryst. Solids 35, 36, 457 (1980).
[6] D. E. Aspnes and J. B. Theeten, J. Electrochem. Soc. 127, 1359 (1980).
[7] F. Shiles, T. Sasaki, M. Inokuti, and D. Y. Smith, Phys. Rev. B 22, 1612 (1980).
[8] P. B. Johnson and R. W. Christy, Phys. Rev. B 9, 5056 (1974).
[9] To compare the two polarizations, π is subtracted from the conventional phase of parallel polarization; reflection convention gives a π phase difference between the two polarizations at normal incidence. This is discussed further in R. S. Longhurst, *Geometrical and Physical Optics*, 3rd ed. (Longman, London, 1973), pp. 512–518.
[10] C. C. Tsai, J. C. Knights, G. Chang, and B. Wacker, J. Appl. Phys. 59, 2998 (1986).
[11] G. M. Wallraff, R. D. Miller, N. Clecak, and M. Baier, Proc. SPIE Symposium on Microlithography, 1991, 1466.